into simple basic mechanisms that will be described next. Two edge dislocations are shown in Figure 4.28(a). After the passage of one of them, one part of the lattice is displaced in relation to the other part by a distance equal to the Burgers vector. Both a positive and a negative dislocation can generate the same shear; however, they have to move in opposite directions in order to accomplish this. The reader is reminded (see Figure 4.20(a)) that the shear and motion directions are the same for edge dislocation.

Screw dislocations can produce the same lattice shear (Figure 4.28(b)). However, in this case the shear takes place perpendicular to the direction of motion of the dislocations; positive and negative screw dislocations have to move in opposite directions in order to produce the same shear strain.

The plane in which a dislocation moves is called a *slip plane*. The slip plane and the loop plane coincide in Figure 4.29. A loop will eventually be ejected from a crystal upon expanding if there is no barrier to its motion. The expansion of a loop will produce an amount of shear in the crystal equal to the Burgers vector of the dislocation. It is worth noting that the shears of the different dislocations are all compatible; there is no incompatibility of movement.

The prismatic loops, consisting totally of edge dislocations, cannot expand like the normal loops. Thus, because the plane of the dislocation does not coincide with the loop plane, the coupled movement of the edge dislocations will force the loop to move perpendicular to its plane, maintaining the same diameter. Upon being ejected from the crystal, a step will be formed at the surface. Figure 4.30 shows a succession of vacancy loops formed by punching of prismatic dislocations.

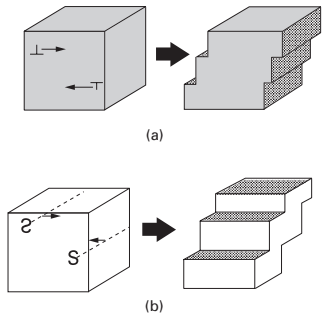

Fig. 4.28 Slip produced by the movement of dislocation. (a) Positive and negative edge dislocations. (b) Positive and negative screw dislocations.

4.4.3 Stress Field Around Dislocations

Dislocations are defects; hence, they introduce stresses and strains in the surrounding lattice of a material. The mathematical treatment of these stresses and strains can be substantially simplified if the medium is considered to be isotropic and continuous. Under conditions of isotropy, a dislocation is completely described by the line and Burgers vectors. With this in mind, and considering the simplest possible situation, dislocations are assumed to be straight, infinitely long lines. Figure 4.31 shows hollow cylinders sectioned

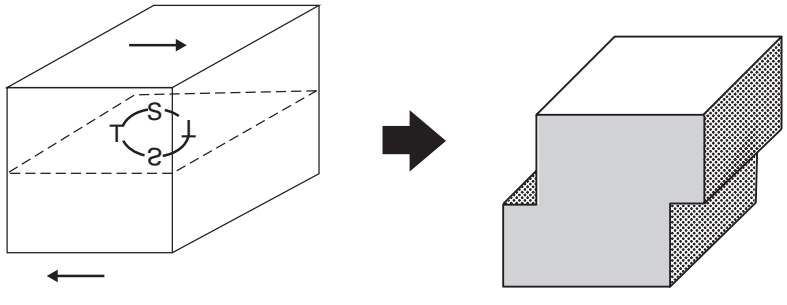

Fig. 4.29 Expansion of a dislocation loop.

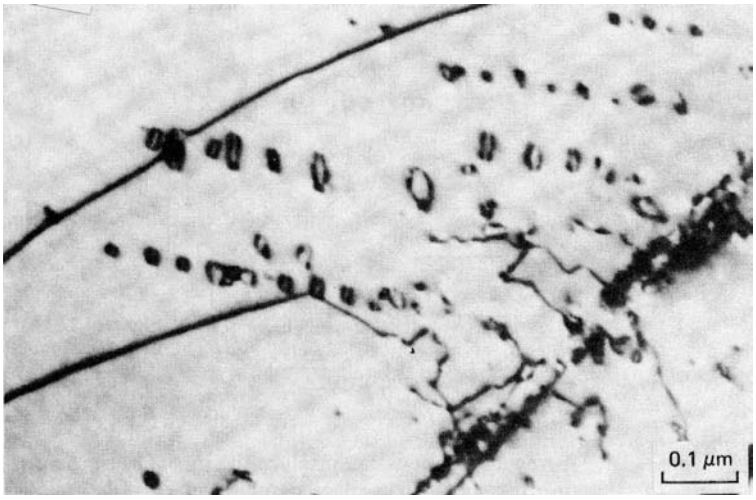

Fig. 4.30 Nickel heated at 600 °C for 10 min and quenched in liquid nitrogen. Strings of vacancy loops can be clearly seen. (Courtesy of L. E. Murr.)

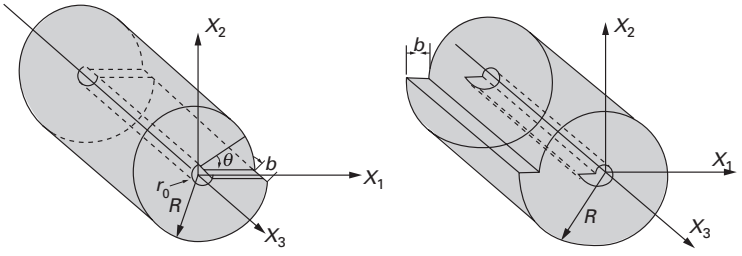

Fig. 4.31 Simple models for (a) screw and (b) edge dislocations; the deformation fields can be obtained by cutting a slit longitudinally along a thick-walled cylinder and displacing the surface by b parallel (screw) and perpendicular (edge) to the dislocation line.

along the longitudinal direction. Different deformations are applied in the two cases. The one in Figure 4.31(a) portrays the deformation around a screw dislocation, while Figure 4.31(b) is an idealization of the strains around an edge dislocation. The cylinders, with external radii R, were longitudinally and transversally displaced by the Burgers vector b, which is parallel (perpendicular) to the cylinder axis in the representation of a screw (an edge) dislocation. In either case, an internal hole with radius r_0 is made through the center. This is done to simplify the mathematical treatment. In a continuous medium, the stresses on the center would build up and become infinite in the absence of a hole; in real dislocations the crystalline lattice is periodic, and this does not occur. In mechanics terminology, this is called a *singularity*, A "singularity" is a spike, or a single event. For instance, the Kilimanjaro is a singularity in the African plains. Therefore, we "drill out" the central core, which is a way of reconciling the continuous-medium hypothesis with the periodic nature of the structure. To analyze the stresses around a dislocation, we use the formal theory of elasticity. For that, one has to use the relationships between stresses and strains (constitutive relationships), the equilibrium equations, the compatibility equations, and the boundary conditions. Hence, the problem is somewhat elaborate. We present the derivation of these relationships here only for the screw

dislocation; see Kuhlmann-Wilsdorf, and Weertman and Weertman (in the suggested reading) for details.

In Figure 4.31, we have the following displacements, for a screw dislocation, along the axes x_1, x_2, and x_3:

$$u_1 = 0, \quad u_2 = 0, \quad u_3 \neq 0.$$

The displacement in the direction x_3 can be assumed to be approximately equal to

$$u_3 = f(\theta) = \frac{b}{2\pi}\theta.$$

This is so because the displacement is b after a rotation of 2π. The angle θ is given by $\tan\theta = x_1/x_2$, thus

$$u_3 = \frac{b}{2\pi}\arctan\frac{x_2}{x_1}. \tag{4.10a}$$

The strain components in indicial notation are:

$$\varepsilon_{ij} = \frac{1}{2}\left(\frac{\partial u_i}{\partial x_j} + \frac{\partial u_j}{\partial x_i}\right) \qquad i, j = 1, 2, 3$$
$$\varepsilon_{11} = 0, \varepsilon_{22} = 0,$$
$$\varepsilon_{12} = 0, \varepsilon_{23} = \frac{1}{2}\frac{\partial u_3}{\partial x_2},$$
$$\varepsilon_{13} = \frac{1}{2}\frac{\partial u_3}{\partial x_1}, \varepsilon_{33} = \frac{\partial u_3}{\partial x_3} = 0.$$

Substituting Equation 4.10a into the equations above, we obtain

$$\varepsilon_{13} = \frac{-bx_2}{4\pi(x_1^2 + x_2^2)}, \tag{4.10b}$$

$$\varepsilon_{23} = \frac{bx_1}{4\pi(x_1^2 + x_2^2)}, \tag{4.10c}$$

$$\sigma_{33} = 0.$$

Now, using the generalized Hooke's law, we have

$$\sigma_{13} = 2G\varepsilon_{13},$$
$$\sigma_{23} = 2G\varepsilon_{23}.$$
$$\sigma_{13} = \sigma_{31} = -\frac{Gbx_2}{2\pi(x_1^2 + x_2^2)}, \tag{4.11a}$$

$$\sigma_{23} = \sigma_{32} = \frac{Gbx_1}{2\pi(x_1^2 + x_2^2)}. \tag{4.11b}$$

The stresses around an edge dislocation are (given without derivation):

$$\sigma_{11} = -\frac{Gbx_2(3x_1^2 + x_2^2)}{2\pi(1-\nu)(x_1^2 + x_2^2)^2}, \tag{4.12a}$$

$$\sigma_{12} = \frac{Gbx_1(x_1^2 - x_2^2)}{2\pi(1-\nu)(x_1^2 + x_2^2)^2}, \tag{4.12b}$$

$$\sigma_{22} = \frac{Gbx_2(x_1^2 - x_2^2)}{2\pi(1-\nu)(x_1^2 + x_2^2)^2}. \tag{4.12c}$$

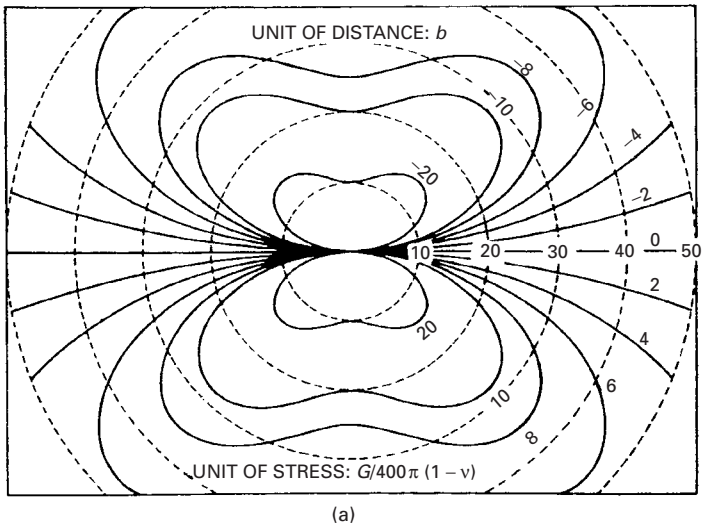

Fig. 4.32 Stress fields around an edge dislocation. (The dislocation line is Ox_3): (a) σ_{11}; (b) σ_{22}; (c) σ_{33}; (d) σ_{12}. (Adapted with permission from J. C. M. Li, in *Electron Microscopy and Strength of Crystals*, eds. G. Thomas and J. Washburn (New York: Interscience Publishers, 1963).)

It then follows that

$$\sigma_{33} = \nu(\sigma_{11} + \sigma_{22}) = -\frac{G\,b\nu\,x_2}{\pi(1-\nu)(x_1^2 + x_2^2)}. \tag{4.12d}$$

These stresses are shown in Figure 4.32 through isostress lines.

4.4.4 Energy of Dislocations

The elastic deformation energy of a dislocation can be found by integrating the elastic deformation energy over the whole volume of the

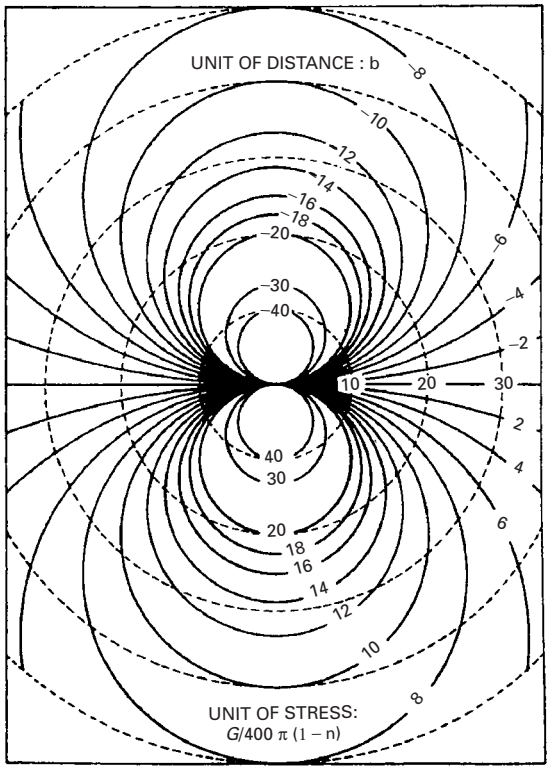

(c)

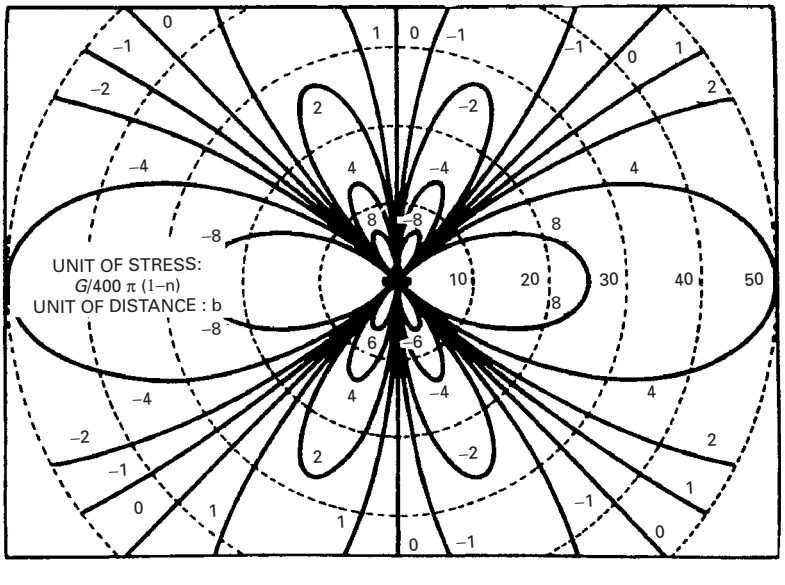

(d)

Fig. 4.32 (continued)

deformed crystal. The deformation energy is given by

$$U = \frac{1}{2}\sigma_{ij}\varepsilon_{ij}. \tag{4.13}$$

For an isotropic material, converting the strains to stresses, we have

$$U = \frac{1}{2G}\left[\frac{1}{2(1+\nu)}(\sigma_{11}^2+\sigma_{22}^2+\sigma_{33}^2)+(\sigma_{12}^2+\sigma_{13}^2+\sigma_{23}^2) - \frac{\nu}{(1+\nu)}(\sigma_{11}\sigma_{33}+\sigma_{11}\sigma_{22}+\sigma_{22}\sigma_{33})\right]. \tag{4.13a}$$

Using Equations 4.10a and 4.10b we have, for a screw dislocation,

$$U_s = \frac{1}{2G}\left[\frac{G^2b^2x_2^2}{4\pi^2(x_1^2+x_2^2)^2}+\frac{G^2b^2x_1^2}{4\pi^2(x_1^2+x_2^2)^2}\right] = \frac{Gb^2}{8\pi^2(x_1^2+x_2^2)}. \tag{4.14}$$

Substituting $(x_1^2 + x_2^2)$ by r^2 (see Figure 4.31), we find that

$$U_s = \frac{Gb^2}{8\pi^2 r^2}. \tag{4.15}$$

Integrating Equation 4.15 between r_0 and R, we get

$$U_s = \int_{r_0}^{R}\frac{Gb^2}{8\pi^2 r^2}2\pi r\,dr = \frac{Gb^2}{4\pi}\ln\frac{R}{r_0}. \tag{4.16}$$

In a similar way, the energy of a straight edge dislocation per unit length is equal to

$$U_\perp = \frac{Gb^2}{4\pi(1-\nu)}\ln\frac{R}{r_0}. \tag{4.17}$$

It should be observed that the factor $(1 - \nu)$ is approximately equal to 2/3. Hence, the energy of an edge dislocation is about 3/2 of that of a screw dislocation.

The schematic drawing of Figure 4.31 removes the core of the dislocation so as to avoid the infinite stresses along the dislocation line. Several methods have been used to estimate r_0. In this book, r_0 will be assumed to be equal to $5b$. Note that the energy given by the foregoing equations become infinite for infinite R; hence, one has to establish an approximate value for R. Dislocations in a metal never occur in a completely isolated manner; they form irregular arrays with mean density ρ. This density is given as the total length of dislocation line per unit volume. The spaghetti analogy can be used here. Imagine a pot with water and spaghetti. The density of the spaghetti would be obtained by measuring the total length of the spaghetti and dividing it by the volume of the pot. The stress fields of the various dislocations interact, as will be seen in subsequent sections; we generally assume a value of R equal to the average distance between the

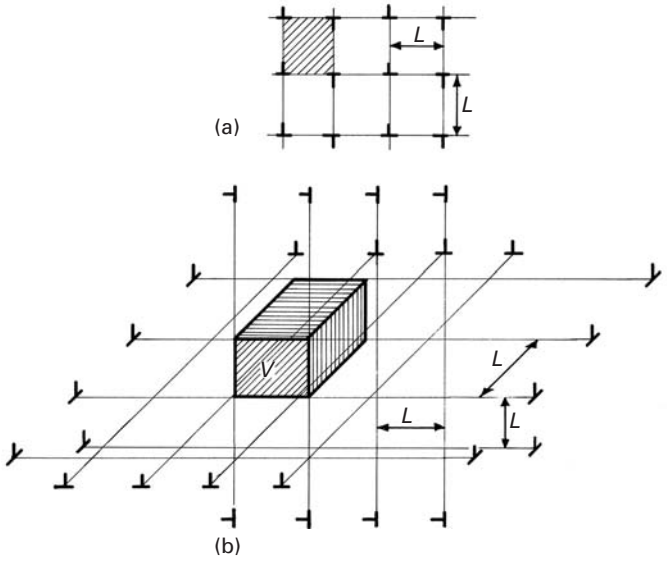

Fig. 4.33 Schematic representation of an idealized dislocation array (a) in two dimensions and (b) in three dimensions; note that dislocations on three perpendicular atomic planes define a volume *V*.

dislocations. It can be shown, by means of a simplified array, that the average distance or mean free path of dislocations is approximately equal to $\rho^{-1/2}$.

It is possible to calculate the radius of influence of each dislocation line, R, from the dislocation density ρ. This radius of influence is equal to $L/2$, in Figure 4.33. Figure 4.33(a) shows a two-dimensional array of dislocations; all dislocation lines "poke out" of the plane of the page. The mean spacing is L, and the hatched area is L^2. This area is bounded by four dislocations, and each dislocation is shared by four areas. Thus,

L^2 area $\rightarrow$ 1 dislocation,
unit area $\rightarrow$ ρ dislocations.

As a result,

$$\boxed{\rho = L^{-2}.} \tag{4.18}$$

The tridimensional calculation is slightly more complicated. Figure 4.33(b) shows a tridimensional array of dislocations. The hatched volume is $V = L^3$. This volume is composed of dislocations that lie along the edges. The total dislocation length can be taken to be 12 L. However, each dislocation is shared by four adjacent cubes. Hence,

$$\rho = \frac{12L/4}{L^3} = 3L^{-2}. \tag{4.19}$$

But

$$R = \frac{L}{2},$$

so that

$$\rho = 3(2\mathrm{R})^{-2}$$

and

$$R = \frac{1}{2}\left(\frac{\rho}{3}\right)^{-1/2} = 0.86\rho^{-1/2}.$$

The average dislocation radius is often taken to be

$$R \approx \rho^{-1/2}.$$

We now add the energy of the dislocation core. This energy is taken to be $Gb^2/10$ for metals. Hence, the total energy of a dislocation is

$$U_r = U_{nucleus} + U_{periphery}.$$

Equation 4.17 can then be generalized to:

$$\boxed{U_r = \frac{Gb^2}{10} + \frac{Gb^2}{4\pi(1-\nu)}(1-\nu\cos^2\alpha)\ln\frac{\rho^{-1/2}}{5b},} \tag{4.20}$$

where α is a parameter that describes the nature of the dislocation (edge $\alpha = \pi/2$, screw $\alpha = 0$), which can be mixed.

The energy of dislocations is often taken to be approximately

$$\boxed{U_r = \frac{Gb^2}{2}.} \tag{4.21}$$

For typical metals, U_r is equal to a few electron volts per atomic plane. The energy of the nucleus is 10% of this total. The energy of a dislocation per atomic plane is high in comparison with that of a vacancy: approximately 3 eV (4.8×10^{-19} J) versus about 1 eV (1.6×10^{-19} J).

Example 4.3

Annealed materials have a dislocation density of approximately 10^8 cm^{-2} or 10^{12} m^{-2}. Calculate the total strain energy for copper.

Solution: For copper, the Burgers vector is $b = 0.25$ nm. Inserting these values into Equation 4.14 and using $\alpha = 0$ (for a screw dislocation), we obtain

$$U = 0.1Gb^2 + \frac{Gb^2}{4\pi}\ln\frac{10^{-6}}{5\times 0.25\times 10^{-9}} = 0.63Gb^2 = \frac{Gb^2}{1.587} \cong \frac{Gb^2}{2}.$$

For this example, the energy per unit length is equal to 1.5×10^{-9} J/m ($G = 48.3$ GPa). The total strain energy is 1.5 kJ/m^3.

4.4.5 Force Required to Bow a Dislocation

Two additional equations will be derived next: the force required to curve a dislocation to a radius R and the Peach–Koehler equation. The analogy of a string helps to explain the energy of a dislocation. In the absence of an external stress field, a dislocation will tend to be straight, minimizing its length and overall energy. The same occurs for a string under tension. If the string is pushed by a force, it will exert a force back. Thus, a curved dislocation is said to possess a "line tension," which can be calculated. The energy of a curved dislocation

with radius R can be calculated (see Weertman and Weertman, p. 50, in the suggested reading) and is equal to

$$U = \frac{Gb^2}{4\pi} \ln \frac{R}{5b}. \tag{4.22a}$$

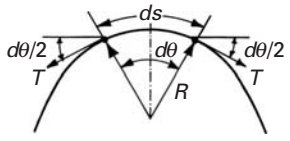

Fig. 4.34 Curved dislocation.

It is possible to calculate the force F required to bend a dislocation into a radius R. Figure 4.34 shows a curved dislocation with radius R. The line tension T is defined as the self-energy per unit length of dislocation. In the figure, the segment of the dislocation ds is "sectioned off," and the remaining dislocation is replaced by two tensions T acting tangentially to the line at the section points. The line tension is always tangential to the dislocation line. The (downward) vertical force exerted by the line tension on the segment ds is

$$F_1 = 2T \sin(d\theta/2).$$

This is balanced by the force F_2 (per unit length) exerted on the dislocation, multiplied by its length:

$$F_2 ds = 2T \sin(d\theta/2).$$

Since $d\theta/2$ is a small quantity,

$$F_2 ds = T\, d\theta.$$

But

$$R\, d\theta = ds,$$
$$F_2 R\, d\theta = T\, d\theta,$$
$$F_2 = T/R$$

Assuming, to a first approximation, that the line tension of a curved dislocation is equal to the energy of a straight dislocation (Eqn. 4.21), we have

$$\boxed{F = Gb^2/2R.} \tag{4.22b}$$

Peach–Koehler equation

The Peach–Koehler equation relates the force applied to a dislocation to a stress. F is the force per unit length of dislocation, and τ is the shear stress acting on the slip plane along the slip direction. This relation can be demonstrated by considering a parallelepiped with dimensions dx_1, dx_2, dx_3. If a dislocation, with length dx_1, on which a force per unit length is F, moves through the parallelepiped, the work done is

$$W = (F\, dx_1) dx_2.$$

The change in strain energy of the cube is equal to $1/2 > \gamma$ in elasticity and $= \zeta\gamma$ in plasticity.

For volume $dx_1 dx_2 dx_3$:

$$U = (\tau\gamma) dx_1 dx_2 dx_3,$$

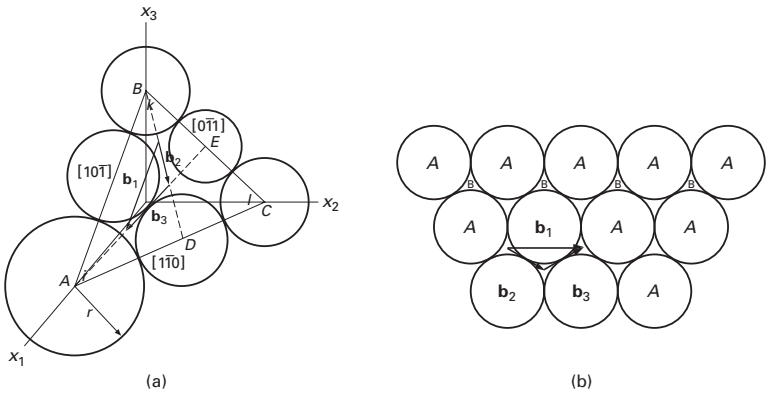

Fig. 4.35 Decomposition of dislocation in an FCC crystal.

where $dx_1\ dx_2\ dx_3$ is the volume of the parallelepiped. The shear strain produced by one dislocation is

$$\gamma = b/dx_3.$$

Since $W = U$,

$$(F\,dx_1)dx_2 = (\tau b/dx_3)dx_1 dx_2 dx_3$$

and

$$\boxed{F = \tau b.} \tag{4.22c}$$

By applying the Peach–Koehler equation to Equation 4.2b, we get the stress required to bow a dislocation to radius R:

$$\boxed{\tau = Gb/2R.} \tag{4.22d}$$

4.4.6 Dislocations in Various Structures

Dislocations in Face-Centered Cubic Crystals

In Section 1.3.2, we saw that, among the 80 or so metals, 55 are FCC. The FCC structure is the closest packed one, together with the HCP structure. Thus, it is natural that dislocations be more carefully studied for the FCC structure.

When we visualize a dislocation, we generally think of a defect that, upon passing, recomposes the original structure of the crystal. Hence, in a simple cubic structure, the Burgers vector would have the direction [100] and magnitude a (lattice parameter). However, there are cases in which the original structure is not recomposed. This type of dislocation is called *imperfect* or *partial*.

In FCC crystals, the closest packed planes are (111). These planes are usually termed A, B, and C, depending on their order in the stacking sequence. Figure 4.35 shows an atomic plane A. The glide movement of the atoms of the plane A that would recompose the same lattice would be indicated by the Burgers vector $\mathbf{b}_1$. This vector has the direction $[10\bar{1}]$. Its magnitude is (it can be also seen in Figure 4.35 that it is equal to the atomic size, and half the side AB):

$$\mathbf{b}_1 = \frac{\left|\overrightarrow{BA}\right|}{2} = 2r \tag{4.23}$$

Vector b_1 is expressed with respect to unit vectors i, j, and k of the coordinate system $Ox_1x_2x_3$ as

$$\overrightarrow{BA} = a(\mathbf{i} + 0\mathbf{j} - \mathbf{k}) \quad \mathbf{b}_1 = \frac{a}{2}\mathbf{i} + 0\mathbf{j} - \frac{a}{2}\mathbf{k} = \frac{a}{2}(\mathbf{i} - \mathbf{k}). \tag{4.24}$$

It can be seen that the magnitude is

$$|\mathbf{b}_1| = \frac{a}{\sqrt{2}}.$$

This vector is, logically, the same as that of Equation 4.23. The simplified notation used for Burgers vectors is

$$\mathbf{b}_1 = \frac{a}{2}[10\bar{1}] \quad \text{or} \quad \mathbf{b}_1 = \frac{1}{2}[10\bar{1}].$$

Hence, the term in brackets gives the direction of the vector, while the term that precedes it is the same fraction as that used in the definition of the unit vectors **i**, **j**, and **k** (see Equation 4.24). There is also a graphic method to determine this fraction. First, one draws the vector **b** connecting point (0, 0, 0) to point (1, 0, –1). Then one draws $\mathbf{b}_1$, which will be a fraction of b (in this case, half). The fraction is the term that precedes the bracketed term.

One possibility of decomposition for the dislocation is shown in Figure 4.35, where $\mathbf{b}_2$ and $\mathbf{b}_3$ add up to $\mathbf{b}_1$. $\mathbf{b}_2$ is obtained from *BD* and $\mathbf{b}_3$ from *EA*.

$$\overrightarrow{BD} = \frac{a}{2}\mathbf{i} + \frac{a}{2}\mathbf{j} - a\mathbf{k}$$

$$\overrightarrow{EA} = a\mathbf{i} - \frac{a}{2}\mathbf{j} - \frac{a}{2}\mathbf{k}.$$

It can be shown that $\mathbf{b}_2 = BD/3$ and that $\mathbf{b}_3 = EA/3$. Both $\mathbf{b}_2$ and $\mathbf{b}_3$ define partial dislocations, because they change the stacking sequence *ABC*. But, acting together (or sequentially), they would have the same effect as $\mathbf{b}_1$ and maintain the correct stacking sequence. $\mathbf{b}_2$ and $\mathbf{b}_3$ are:

$$\mathbf{b}_2 = \frac{a}{6}(\mathbf{i} + \mathbf{j} - 2\mathbf{k})$$

$$\mathbf{b}_3 = \frac{a}{6}(2\mathbf{i} - \mathbf{j} - \mathbf{k})$$

and

$$\mathbf{b}_1 = \mathbf{b}_2 + \mathbf{b}_3.$$

It is easy to establish whether $\mathbf{b}_1$, $\mathbf{b}_2$, and $\mathbf{b}_3$ belong to (111): the scalar product should be zero, because [111], which is perpendicular to (111), should also be perpendicular to $\mathbf{b}_1$, $\mathbf{b}_2$, and $\mathbf{b}_3$. The magnitude of $\mathbf{b}_2$ is given by:

$$|\mathbf{b}_2| = \left[\frac{a^2}{36}(1 + 1 + 4)\right]^{1/2}$$

$$= \frac{a}{\sqrt{6.}}$$

Hence, we have the following possible reaction:

$$\frac{a}{2}[10\bar{1}] \rightarrow \frac{a}{6}[11\bar{2}] + \frac{a}{6}[2\bar{1}\bar{1}].$$

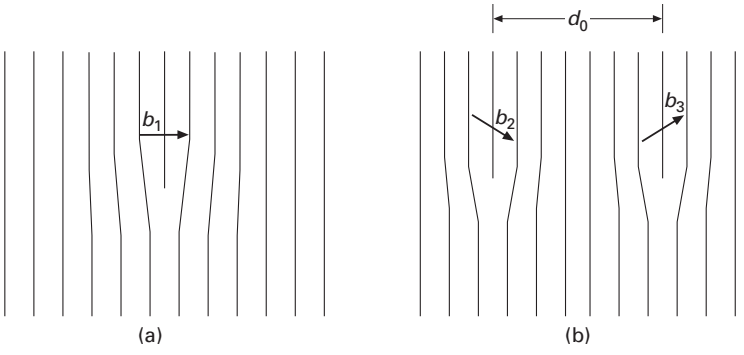

Fig. 4.36 Decomposition of a dislocation b_1 into two partial dislocations b_2 and b_3, separated by a distance d_0.

From Equation 4.21, the energy is $Gb^2/2$. Therefore, we need to check whether

$$\frac{G\,b_1^2}{2} \rightleftharpoons \frac{G\,b_2^2}{2} + \frac{G\,b_3^2}{2},$$

or $b_1^2 \rightleftharpoons b_2^2 + b_3^2$. Taking the square of the magnitude of the Burgers vectors yields

$$\frac{a^2}{2} > \frac{a^2}{6} + \frac{a^2}{6},$$

and we can see that the total energy decreases with decomposition.

When a perfect dislocation decomposes itself into partials, a region of faulty stacking is created between the partials. This decomposition is shown in Figure 4.36. The dislocations generate a region in which the stacking is *ABC AC ABC*. Hence, we have four planes in which the stacking is *CACA*. This is exactly the stacking sequence of the HCP structure. This structure has a higher Gibbs free energy than the equilibrium FCC structure, because it is not thermodynamically stable under the imposed conditions. This specific array of planes is called the *stacking fault*, and the energy associated with it determines the separation between the two partial dislocations: The repulsive force between the two partials is balanced by the attraction trying to minimize the region with the stacking fault. The following equations from [Murr[6] and Kelly and Groves, (see the suggested reading) respectively], allow the calculation of the equilibrium separation between the partial dislocations d:

$$\gamma_{SF} = \frac{G\,|b_p|^2}{8\pi d}\left[\frac{2-\nu}{1-\nu}\left(1 - \frac{2\nu\cos 2\theta}{2-\nu}\right)\right],$$

$$\gamma_{SF} = \frac{G\,b_1 b_2}{2\pi d}\left(\cos\theta_1\cos\theta_2 + \frac{\sin\theta_1\sin\theta_2}{2-\nu}\right),$$

or, in simplified form:

$$\boxed{\gamma_{SF} = \frac{G\,b^2}{2\pi d}.} \tag{4.25}$$

Here, γ is the stacking-fault free energy (SFE) per unit area (free energy of HCP minus free energy of FCC), $\mathbf{b_p}$ is the Burgers vector of

[6] L. E. Murr, *Interfacial Phenomena in Metals and Alloys* (Reading, MA: Addison-Wesley, 1975), p. 142.

Table 4.2 Stacking Fault Free Energies and Separation between Shockley Partials for Metals ($\theta = 30°$)[a]

Metal	γ (mJ/m^2)	a_0 (nm)	b (nm)	G (GPa)	d (nm)
Aluminum	166	0.41	0.286	26.1	1
Copper	78	0.367	0.255	48.3	3.2
Gold	45	0.408	0.288	27.0	
Nickel	128	0.352	0.249	76.0	2.9
Silver	22	0.409	0.289	30.3	9

[a] Adapted from L. E. Murr, *Interfacial Phenomena in Metals and Alloys* (Reading, MA: Addison-Wesley, 1975).

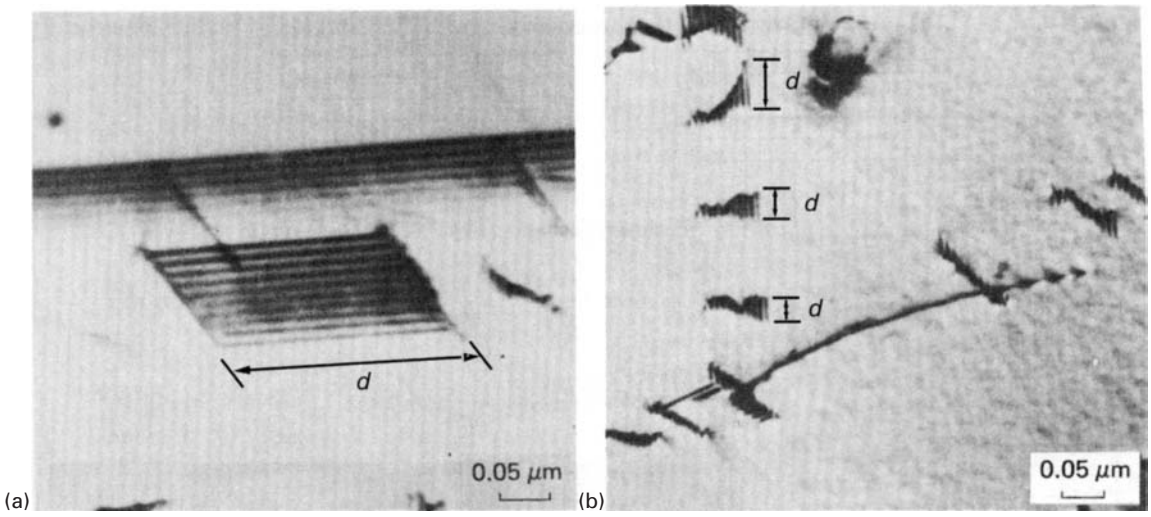

Fig. 4.37 (a) Short segment of stacking fault in AISI 304 stainless steel overlapping with coherent twin boundary. (a) Differences in the nature of these defects are illustrated by fringe contrast differences. (b) Dislocations in AISI 304 stainless steel splitting into partials bounded by short stacking-fault region. Partials spacing marked as *d*. (Courtesy of L. E. Murr.)

the partial dislocation, and θ is the angle of the Burgers vector with the dislocation line. Table 4.2 presents the SFEs for some materials. From the preceding equations, it can be seen that d is inversely proportional to γ. The effect of alloying elements is generally to decrease the SFE. The addition of aluminum to copper has a drastic effect on the latter's SFE, dropping it from 78 to 6 mJ/m^2. Aluminum, which has a high SFE (166 mJ/m^2), does exhibit a very small separation between partials: 1 nm. On the other hand, in certain alloy systems, the distance can go up to 10 nm or more.

The stacking-fault energy is very sensitive to composition. Usually, alloying has the effect of decreasing the SFE. Hence, brasses have an SFE lower than that of copper, and Al alloys have an SFE lower than that of Al.

Figure 4.37 shows some stacking faults in AISI 304 stainless steels viewed by transmission electron microscopy. The region corresponding to the stacking fault can be clearly seen by the characteristic fringe (////) pattern. The extremities of the fringes are bound by the partial dislocations. In Figure 4.37(a), the stacking fault lies parallel to a coherent twin boundary, which is much longer than the stacking fault. The fault can be distinguished from the coherent twin

boundary by the differences in fringe contrast. While all the fringes of the stacking fault are dark, the ones in the twin are dark at the top and become successively lighter. Figure 4.37(b) shows a number of dislocations (probably emitted from the same source) whose segments are trapped on the foil. These segments have decomposed into partials, and one can clearly distinguish the stacking-fault regions by the characteristic fringe contrast.

The effect of the stacking-fault energy on the deformation substructure can be seen in Figure 4.38. This figure shows (a) a copper and (b) Cu–Al alloy after deformation by shock loading under identical conditions (40 GPa peak pressure, 3 ns pulse duration). The Cu–Al alloy has a significantly lower stacking-fault energy ($\gamma_{SF} = 39\,mJ/m^2$) than does pure copper ($\gamma_{SF} = 78\,mJ/m^2$), and the resultant deformation substructures seem to be strongly affected by this difference. Low-SFE metals tend to exhibit a deformation substructure characterized by banded, linear arrays of dislocations, whereas high-SFE metals tend to exhibit dislocations arranged in tangles or cells. Cross-slip is more difficult in low-SFE alloys because the dislocations have to constrict in order to change slip planes. (See Chapter 6.) Therefore, the dislocations arrange themselves into parallel bands. The SFE also affects the work-hardening of alloys.

Another type of dislocation in FCC structures is called a *sessile* or *Frank dislocation*, which is immobile. Sessile or Frank dislocations appear under two specific conditions, shown in Figure 4.39. In Figure 4.39(a), a disk was removed in plane (111); in Figure 4.39(b), a disk was added. It can be seen that in both cases the stacking sequence was changed, to *ABCBCA* and *ABCBABC* for Figure 4.39(a) and (b), respectively. The Burgers vector is given by:

$$\mathbf{b} = \frac{a}{3}[111].$$

We have a sample of an *intrinsic* stacking fault in Figure 4.39(a) and an *extrinsic*, or double-stacking fault in Figure 4.39(b). Since the Burgers vector is not in the slip plane, the two faults are immobile. Another type of immobile dislocation that can occur in FCC metals is the Lomer–Cottrell lock. Let us consider two (111) and (11$\bar{1}$) planes. The three perfect dislocations on (111) are

$$\mathbf{b}_1 = \frac{a}{2}[1\bar{1}0],$$
$$\mathbf{b}_2 = \frac{a}{2}[\bar{1}01],$$
$$\mathbf{b}_3 = \frac{a}{2}[01\bar{1}],$$

For plane (11$\bar{1}$), we have

$$\mathbf{b}_4 = \frac{a}{2}[\bar{1}10],$$
$$\mathbf{b}_5 = \frac{a}{2}[101],$$
$$\mathbf{b}_6 = \frac{a}{2}[011].$$

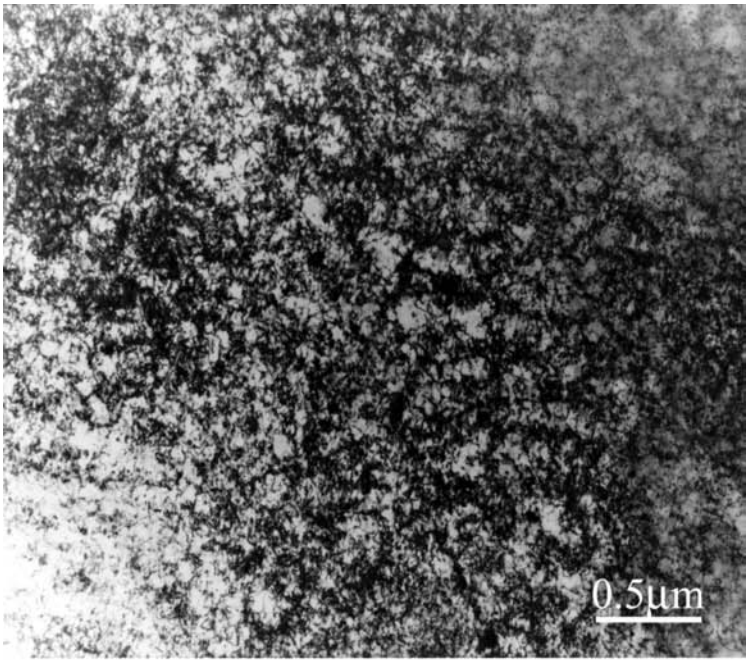

(a)

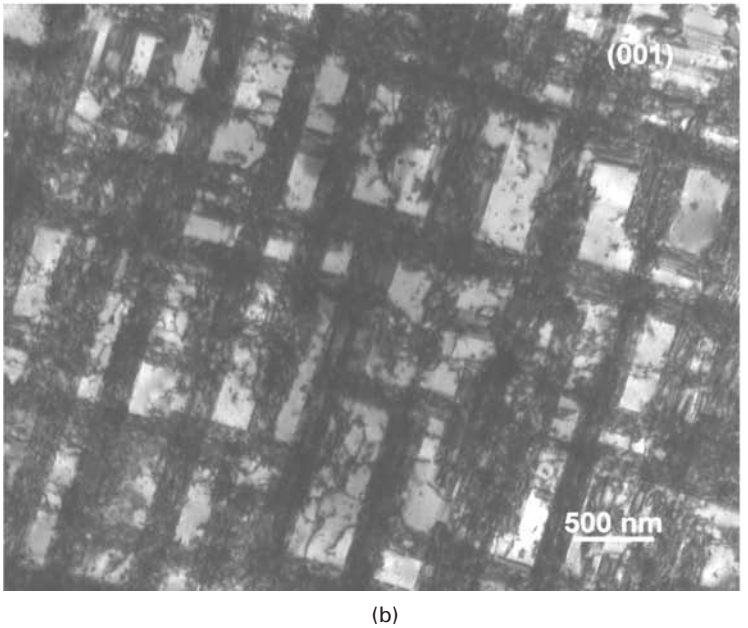

(b)

Fig. 4.38 Effect of stacking-fault energy on dislocation substructure. (a) High-stacking-fault-energy material (pure copper); (b) lower-stacking-fault-energy material (copper–2 wt% aluminium). Both materials were laser-shock compressed with an initial pressure of 40 GPa and pulse duration of 3 ns. (Courtesy of M. S. Schneider.)

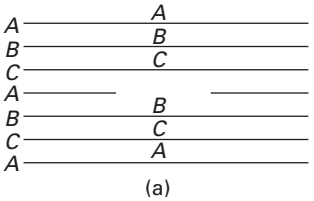

(a)

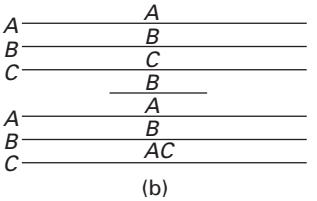

(b)

Fig. 4.39 Frank or Sessile dislocations. (a) Intrinsic. (b) Extrinsic.

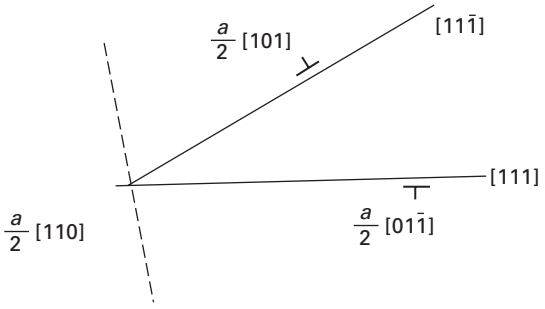

Fig. 4.40 Cottrell–Lomer lock.

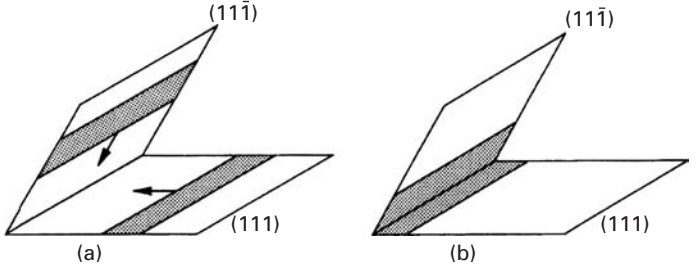

Fig. 4.41 Stairway dislocation.

One good rule to determine whether a direction belongs to a plane is that the scalar product between the direction **b** and the normal to the plane must be zero (in a cubic structure). This rule comes from vector calculus. Vectors $\mathbf{b}_1$ and $\mathbf{b}_4$ have the same direction and opposite senses; the common direction is also that of the intersection of the two planes. Hence, both dislocations will cancel when they encounter each other. The combination of $\mathbf{b}_2$ and $\mathbf{b}_5$ would result in

$$\mathbf{b}_2 + \mathbf{b}_5 = \frac{a}{2}[\bar{1}01] + \frac{a}{2}[101] = \frac{a}{2}[002] = a[001].$$

The energy of these dislocations is

$$\frac{a^2}{2} + \frac{a^2}{2} = a^2$$

Therefore, this reaction will not occur, because it will not result in a reduction of the energy. The only combinations that *would* result in a decrease in the overall energy would be of the type

$$\begin{aligned}\mathbf{b}_3 + \mathbf{b}_5 &= \frac{a}{2}[01\bar{1}] + \frac{a}{2}[101] \\ &= \frac{a}{2}[110].\end{aligned}$$

This reaction, which is energetically favorable, is shown in Figure 4.40. The dislocation is not mobile in either the (111) or (11$\bar{1}$) plane; hence, it acts as a barrier for any additional dislocation moving in these planes. Since it impedes slip, it is called a Lomer–Cottrell "lock."

The resultant configuration is shown in Figure 4.41; it resembles a stair and is therefore called a "stair-rod" or "stairway" dislocation. The

leading partials react and immobilize the partials coupled to them (the trailing partials). The bands of stacking faults form a configuration resembling steps on a stairway. These steps are barriers to further slip on the atomic planes involved, as well as in the adjacent planes.

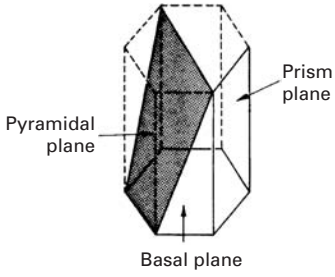

Fig. 4.42 Basal, pyramidal, and prism plane in HCP structure.

Dislocations in Hexagonal Close-Packed Crystals

In HCP crystals, the stacking sequence of the most densely packed planes is *ABAB*. These planes are known as basal planes. Figure 4.42 shows the main planes in the HCP structure. Perfect dislocations moving in the basal plane can decompose into Shockley partials, just as in the FCC structure. Stacking faults are also formed (only *intrinsic* stacking faults). This analogy can be easily understood if one realizes the similarity between the two structures. The (111) planes in the FCC structure are the equivalent of the basal planes in the HCP structures. A perfect dislocation in the basal plane has the Burgers vector

$$b = \frac{a}{3}[2\,\bar{1}\,\bar{1}\,0].$$

In an ideal hexagonal crystal, the c/a ratio is 1.633. However, in real hexagonal crystals this never happens. It has been experimentally observed that, for crystals with $c/a > 1.633$, slip occurs mainly on the basal plane, while the pyramidal and prism planes are "preferred" in crystals with $c/a < 1.633$. This is due to the dependence of the distance between the atoms upon c/a; it is well known that the dislocations tend to move in the highest packed planes. A detailed treatment of dislocations in HCP metals is given by Teutonico.[7]

Dislocations in Body-Centered Cubic Crystals

In BCC crystals, the atoms are closest to each other along the <111> direction. Any plane in the BCC crystal that contains this direction is a suitable slip plane. Slip has been experimentally observed in (110), (112), and (123) planes. The slip markings in BCC metals are usually wavy and ill-defined. The following reaction has been suggested for a perfect dislocation having its Burgers vector along <111>:

$$\frac{a}{2}[\bar{1}\bar{1}1] \rightarrow \frac{a}{8}[\bar{1}\bar{1}0] + \frac{a}{4}[\bar{1}\bar{1}2] + \frac{a}{8}[\bar{1}\bar{1}0].$$

This corresponds to the equivalent of Shockley partials. Apparently, the stacking-fault energy is very high, because the faults cannot be observed by transmission electron microscopy. The waviness of the slip markings is also indicative of the high stacking-fault energy. If the partials were well separated, slip would be limited to one plane. Cross-slip, which will be treated in Chapter 6, is much easier when the stacking-fault energy is high. If one adds up all the slip systems for BCC, one obtains a number of 48. This is much higher than the number for FCC.

[7] L. J. Teutonico, *Mater. Sci & Eng.*, 6 (1970) 27.

Example 4.4

Consider the following body-centered cubic dislocation reaction:

$$\frac{a}{2}[\bar{1}\bar{1}1] \rightarrow \frac{a}{8}[\bar{1}\bar{1}0] + \frac{a}{4}[\bar{1}\bar{1}2] + \frac{a}{8}[\bar{1}\bar{1}0].$$

a. Prove that this reaction will occur.
b. What kind of dislocations are the $(a/8)<110>$ and $(a/4)<112>$?
c. What kind of crystal imperfection results from this dislocation reaction?
d. What determines the distance of separation of the $(a/8)$ $[\bar{1}\bar{1}0]$ and the $(a/4)$ $[\bar{1}\bar{1}2]$ dislocations?

Solution: (a) $U \alpha b^2$:

$$\frac{a}{2}[\bar{1}\bar{1}1] \rightarrow \underset{b_1}{\frac{a}{8}[\bar{1}\bar{1}0]} + \underset{b_2}{\frac{a}{4}[\bar{1}\bar{1}2]} + \underset{b_3}{\frac{a}{8}[\bar{1}\bar{1}0]}.$$

On the left-hand side:

$$b^2 = \left(\frac{-a}{2}\right)^2 + \left(\frac{-a}{2}\right)^2 + \left(\frac{a}{2}\right)^2 = \frac{3}{4}a^2.$$

On the right-hand side:

$$b_1^2 + b_2^2 + b_3^2 = \left[\left(\frac{-a}{8}\right)^2 + \left(\frac{-a}{8}\right)^2 + 0^2\right] + \left[\left(\frac{-a}{4}\right)^2 + \left(\frac{-a}{4}\right)^2 + \left(\frac{2a}{4}\right)^2\right] + \left[\left(\frac{-a}{8}\right)^2 + \left(\frac{-a}{8}\right)^2 + 0^2\right]$$

$$= \frac{a^2}{32} + \frac{3a^2}{8} + \frac{a^2}{32} = \frac{7a^2}{16}.$$

Since

$$\frac{3}{4}a^2 > \frac{7a^2}{16},$$

the energy is lower after the reaction, and therefore, the reaction will occur.

(b) Partial dislocations.
(c) Stacking fault.
(d) Stacking-fault energy, γ_{SF}.

$$\gamma_{SF} \propto \frac{b_1 b_2}{d},$$

with b_1, b_2 known from (a),

$$\Rightarrow \gamma_{SF} \propto \frac{1}{d}$$

$$\Rightarrow d \propto \frac{1}{\gamma_{SF}}.$$

That is, if γ_{SF} increases, the distance between the dislocations decreases.

Example 4.5

Make a table with all the 48 slip systems for the BCC structure.

Solution: For each slip system, we have to satisfy the condition $\mathbf{u} \cdot \mathbf{v} = 0$. For (110) $[1\bar{1}1]$, $1 \times 1 + 1 \times (-1) + 0 \times 1 = 0$.

The table of 48 slip systems for the BCC structure is as follows.

Slip Plane {110}		Slip Plane {112}		Slip Plane {123}			
$(1\,1\,0)$	$[1\,\bar{1}\,1]$	$(1\,1\,2)$	$[\bar{1}\,\bar{1}\,1]$	$(1\,2\,3)$	$[1\,1\,\bar{1}]$	$(1\,2\,3)$	$[\bar{1}\,1\,1]$
$(1\,1\,0)$	$[1\,\bar{1}\,\bar{1}]$	$(1\,2\,1)$	$[\bar{1}\,\bar{1}\,1]$	$(1\,3\,2)$	$[1\,\bar{1}\,1]$	$(1\,3\,2)$	$[\bar{1}\,1\,1]$
$(1\,\bar{1}\,0)$	$[1\,1\,\bar{1}]$	$(2\,1\,1)$	$[\bar{1}\,1\,1]$	$(3\,1\,2)$	$[\bar{1}\,1\,1]$	$(3\,1\,2)$	$[1\,\bar{1}\,1]$
$(1\,1\,0)$	$[1\,1\,1]$	$(1\,1\,\bar{2})$	$[1\,1\,1]$	$(3\,2\,1)$	$[\bar{1}\,1\,1]$	$(3\,2\,1)$	$[1\,1\,\bar{1}]$
$(1\,0\,\bar{1})$	$[1\,1\,1]$	$(1\,\bar{2}\,1)$	$[1\,1\,1]$	$(2\,1\,3)$	$[1\,1\,\bar{1}]$	$(2\,1\,3)$	$[1\,\bar{1}\,1]$
$(1\,0\,\bar{1})$	$[1\,\bar{1}\,1]$	$(\bar{2}\,1\,1)$	$[1\,1\,1]$	$(2\,3\,1)$	$[1\,\bar{1}\,1]$	$(2\,3\,1)$	$[1\,1\,\bar{1}]$
$(1\,0\,1)$	$[1\,1\,\bar{1}]$	$(1\,\bar{1}\,2)$	$[1\,\bar{1}\,\bar{1}]$	$(1\,2\,3)$	$[1\,1\,1]$	$[\bar{1}\,2\,3]$	$[1\,\bar{1}\,1]$
$(1\,0\,1)$	$[1\,\bar{1}\,\bar{1}]$	$(1\,2\,\bar{1})$	$[1\,\bar{1}\,\bar{1}]$	$(1\,3\,2)$	$[1\,1\,1]$	$[\bar{1}\,3\,2]$	$[1\,1\,\bar{1}]$
$(0\,1\,1)$	$[1\,1\,\bar{1}]$	$(2\,1\,\bar{1})$	$[\bar{1}\,1\,\bar{1}]$	$(3\,1\,2)$	$[1\,1\,1]$	$[3\,\bar{1}\,2]$	$[1\,1\,\bar{1}]$
$(0\,1\,1)$	$[\bar{1}\,1\,1]$	$(\bar{1}\,1\,2)$	$[\bar{1}\,1\,\bar{1}]$	$(3\,1\,2)$	$[1\,1\,1]$	$[3\,2\,\bar{1}]$	$[1\,\bar{1}\,1]$
$(0\,\bar{1}\,1)$	$[1\,1\,1]$	$(\bar{1}\,2\,1)$	$[1\,1\,\bar{1}]$	$(2\,1\,3)$	$[1\,1\,1]$	$[2\,\bar{1}\,3]$	$[\bar{1}\,1\,1]$
$(0\,\bar{1}\,1)$	$[\bar{1}\,1\,1]$	$(2\,\bar{1}\,1)$	$[1\,1\,\bar{1}]$	$(2\,3\,1)$	$[1\,1\,1]$	$[2\,3\,\bar{1}]$	$[\bar{1}\,1\,1]$

4.4.7 Dislocations in Ceramics

Transmission electron microscopy has revealed dislocations in most nonmetals. Dislocations in semiconductors, minerals, oxide ceramics, and carbides, nitrides, and borides have been described and characterized. Many nonmetals tend to exhibit brittle behavior, in which dislocations play a minor role. However, if the temperature or lateral confinement of the material is sufficiently high, ductile behavior can be observed; in this case, dislocations play an important role. The role of confinement, or externally applied traction on planes parallel to the principal direction of external loading, is described in Chapter 7. The principal effect is to eliminate tensile stresses at the tips of internal flaws, thereby enabling the nonmetal to deform plastically. The temperature provides thermal activation that assists the overcoming of short-range obstacles by dislocations.

Table 4.3 lists the minimum temperatures at which ductile behavior is observed in ceramics. Most ceramics have high ductile-to-brittle transition temperature, and this has rendered the study of dislocations difficult. These high temperatures also affect the mechanisms of dislocation motion, since diffusion plays an important role at temperatures greater than or equal to $0.4T_m$, where T_m is the melting point in K. The climb of dislocations is an effective mechanism for overcoming obstacles.

Table 4.3 | Approximate Temperature for Macroscopic Plasticity in Some Ceramics

Ceramic	Melting point, T_m (K)	Softening point, $0.4T_m$ (K)
B_4C	2,725	1,090
TiC	3,400	1,360
HfC	4,425	1,770
WC	3,000	1,200
SiC	2,970	1,188
MgO	3,100	1,240
ZrO_2	3,100	1,240
Al_2O_3	2,325	930
TiO_2	2,100	844
SiO_2 (cristobalite)	1,990	796
S_3N_4	2,715	1,086
$MoSi_2$	2,300	920

Table 4.4 | Crystal Structures, Slip Systems, and Burgers Vectors for Ceramics (Courtesy of T. E. Mitchell)

Oxide	Slip system	Burgers vector	Other slip systems
MgO	$\{110\}\langle 1\bar{1}0\rangle$	$\frac{1}{2}\langle 1\bar{1}0\rangle = d_0$	$\{001\}\langle 1\bar{1}0\rangle$, $\{111\}\langle 1\bar{1}0\rangle$
$MgAl_2O_4$	$\{111\}\langle 1\bar{1}0\rangle$	$\frac{1}{2}\langle 1\bar{1}0\rangle = 2d$,	$\{110\}\langle 1\bar{1}0\rangle$
Al_2O_3	$(0001)\langle 11\bar{2}0\rangle$	$\frac{1}{3}\langle 11\bar{2}0\rangle = \sqrt{3d_0}\rangle$	$\{1120\}\langle 10\bar{1}0\rangle$, $\{\bar{1}102\}\langle \sim 11\bar{2}0\rangle$
TiO_2	$\{001\}\langle 0\bar{1}1\rangle$	$\langle 0\bar{1}1\rangle \simeq 2d_0$	$\{110\}$ [001]
Mg_2SiO_4	(100), $\{110\}$ [001]	$[011] = 2d_0$	(100) [010],$\{0kl\}$[100]
BeO	$(0001)\langle 11\bar{2}0\rangle$	$\frac{1}{3}\langle 11\bar{2}0\rangle = d_0$	$\{1100\}\langle 11\bar{2}0\rangle$, $[0001]\{10\bar{1}0\}$
UO_2	$\{001\}\langle 1\bar{1}0\rangle$	$\frac{1}{2}\langle 1\bar{1}0\rangle = \sqrt{2d_0}$,	$\{110\}$, $\{111\}\langle 1\bar{1}0\rangle$
SiO_2 (quartz)	$(0001)\langle 11\bar{2}0\rangle$	$\frac{1}{3}\langle 11\bar{2}0\rangle$	$\{1120\}$, $\{1010\}[\bar{0}001]$

The structures of a number of ceramics are given in Chapter 1. (See Figure 1.17.) In general, ceramics tend to slip along directions that are closest packed. Since ceramics possess ordered structures, and a perfect dislocation must recompose the original atomic arrangement, the Burgers vectors tend to be large.

Table 4.4 lists slip systems and Burgers vectors for a number of ceramics. For the oxide ceramics, the oxygen atoms (anions) tend to arrange themselves in close-packed structures (FCC or HCP), and this determines the slip systems. For instance, Al_2O_3 (HCP) has basal slip, where the slip lane is (0001) and the slip directions are $<11\bar{2}0>$. Prismatic or pyramidal slip are also possible. (See Table 4.4.) The Burgers vector is given by

$$b = \frac{1}{3}<11\bar{2}0> = \sqrt{3d_0},$$

where d_0 is the nearest distance between oxygen atoms. Recall that the oxygen atoms form an HCP structure. The arrangement of atoms in the basal plane is shown in Figure 4.43. The large circles are the

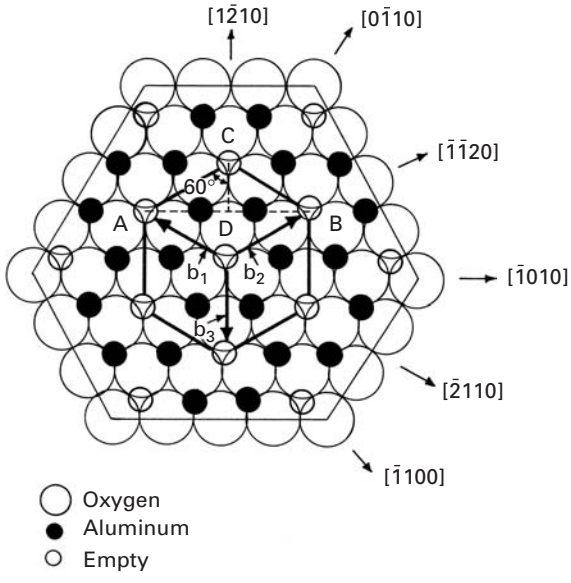

Fig. 4.43 Basal plane in Al_2O_3.

oxygen anions, forming a closed-packed hexagonal array. The full circles are the aluminum cations, which stack in the *ABC* sequence (similar to the FCC structure). The empty circles are normally empty octahedral interstices. The vectors $\mathbf{b}_1$, $\mathbf{b}_2$, and $\mathbf{b}_3$ are the Burgers vectors. They translate interstitial sites in such a manner that they become superposed. The magnitude of the Burgers vectors is equal to $\sqrt{3}$. This can be shown from the triangle *ABC*, where $BC = \sqrt{3}d_0$ and the angle *BCA* is equal to 120°.

For MgO, the anions form an FCC structure, and the Burgers vector has the direction $<1\bar{1}0>$ and a magnitude equal to d_0, the smallest oxygen spacing. Thus,

$$b = \frac{1}{2}<1\bar{1}0> = d_0.$$

The dislocations in ceramics generally have a high energy, due to the large shear modulus and Burgers vector ($U \sim Gb^2/2$). Table 4.5 gives Burgers vectors and self-energies for dislocations in a number of intermetallics and ceramics. For purposes of comparison, the dislocation energy of aluminum is shown. The differences can be dramatic. The Peierls–Nabarro stress (see Section 4.4.12) is very high, in general, because of the directionality of bonding in ionic and covalent structures. For instance, the bond angles of 109° for the carbon atom need very high forces to be distorted. The movement of a dislocation requires the breaking and remaking of bonds, and distortions are produced around the dislocations. Therefore, the movement of dislocations in ceramics is, in general, difficult. There are exceptions, however, such as MgO, which can exhibit significant plasticity at close to ambient temperature.

Dislocation interactions and reactions occur in a manner similar to that in metals and intermetallics. An example is given in Figure 4.44. Dislocation dipoles are often observed in the deformation

Table 4.5 | Elastic Energy for Dislocations in Ceramics and Intermetallics (Courtesy of Veyssiere)

	Oxygen Sublattice	**b**	b(nm)	G(GPa)	$Gb^2/2$
Al		$\frac{1}{2}$ <110>	0.286	27	1.2
Ni_3Al		<110>	0.356	100	6.4
MgO	FCC	$\frac{1}{2}$ <110>	0.298	125	5.1
CoO	FCC	$\frac{1}{2}$ <110>	0.301	70	3.2
NiO	FCC	$\frac{1}{2}$ <110>	0.296	135	5.9
$MgAl_2O_4$	FCC	$\frac{1}{2}$ <110>	0.57	120	19.5
BeO	HCP	$\frac{1}{3} < 11\bar{2}0 >$	0.27	160	5.9
$Al_2O_3 - \alpha$	HCP	$\frac{1}{3} < 11\bar{2}0 >$	0.476	200	22.6
TiO_2	distorted	<001>	0.296	100	4.4
	HCP	<101>	0.546		14.9
CuO_2	BCC	<001>	0.427	10	0.9
		<011>	0.604		1.8
UO_2	cubic	$\frac{1}{2}$ <110>	0.386	94	7.0
Y_2O_3	vacancy —	$\frac{1}{2}$ <111>	0.918	65	27.4
	containing cubic	<100>	1.06		31.5
$Y_3Fe_5O_{12}$	highly	$\frac{1}{2}$ <111>	1.072	78	44.8
	distorted	<100>	1.038		42.0

of sapphire and are shown in Figure 4.44(a). These dipoles are parallel edge dislocations of opposite sign that are attracted together into a position of approximately 45° (55° if there is anisotropy) in order to minimize the elastic fields. This is shown in Figure 4.44(b). In Figure 4.32(d), the elastic (shear stress) fields of edge distortions are shown. The shear stresses σ_{12} are minimized if they place themselves at 45°. These dipoles break down and form loops, as indicated in Figure 4.44(a). The stress fields of one dislocation are canceled by those of the other dislocation, at 45°, as shown in Figure 4.44(b). Dislocation dissociations and reactions are also observed and can be predicted from energetics. A hexagonal dislocation network is shown in Figure 4.45. The total Burgers vector at the nodes has to be equal to zero under equilibrium. This is called *Frank's rule*. For basal dislocations in a hexagonal structure, we have, at the nodes,

$$\frac{1}{3}[11\bar{2}0] + \frac{1}{3}[1\bar{2}10] + \frac{1}{3}[\bar{2}110] = 0.$$

And for the FCC structure,

$$\frac{1}{2}[1\bar{1}0] + \frac{1}{2}[01\bar{1}] + \frac{1}{2}[\bar{1}01] = 0.$$

These structures are often produced during recovery.

The dissociation of a perfect dislocation into partial dislocations is treated in a manner similar to that in metals. The criterion of energy

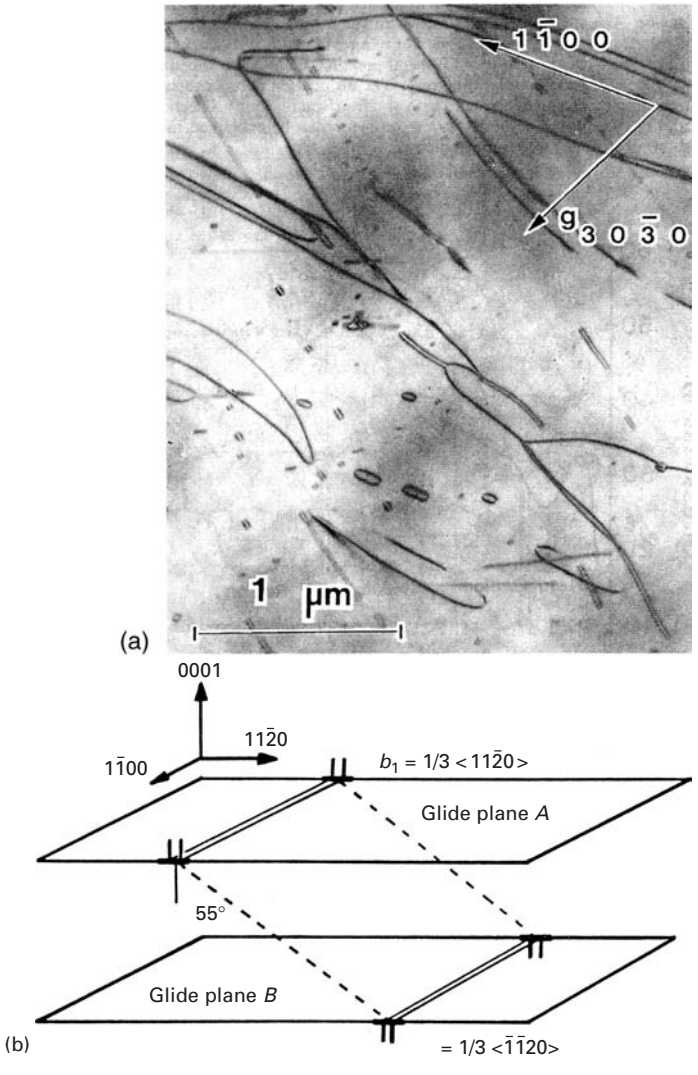

Fig. 4.44 (a) Dislocations, dipoles, and loops in sapphire. (b) Interaction between dislocations in sapphire. (From K. P. D. Lagerdorf, B. J. Pletka, T. E. Mitchell, and A. H. Heuer, *Radiation Effects*, 74 (1983) 87.)

decrease ($U \approx Gb^2/2$) is applied, and dissociation is stable if $b^2 > b_1^2 + b_2^2$.

A few dislocation dissociations have been observed in ceramics. In the spinel structure, the dissociation

$$\frac{1}{2}[1\bar{1}0] \rightarrow \frac{1}{4}[1\bar{1}0] + \frac{1}{4}[1\bar{1}0]$$

was observed, and the following dissociation was suggested to occur in Al_2O_3:

$$\frac{1}{3}[11\bar{2}0] \rightarrow \frac{1}{3}[10\bar{1}0] + \frac{1}{3}[01\bar{1}0].$$

This dissociation has been observed to occur only by climb.

As an illustration of the occurrence of stacking faults in ceramics, Figure 4.46 shows a TEM of gallium phosphide. The large concentration of these faults is evident. They are a common occurrence in thin

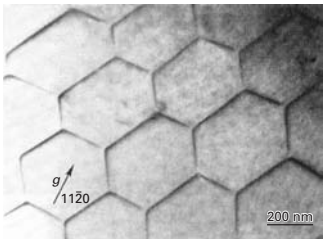

Fig. 4.45 Hexagonal array of dislocations in titanium diboride. (Courtesy of D. A. Hoke and G. T. Gray.)

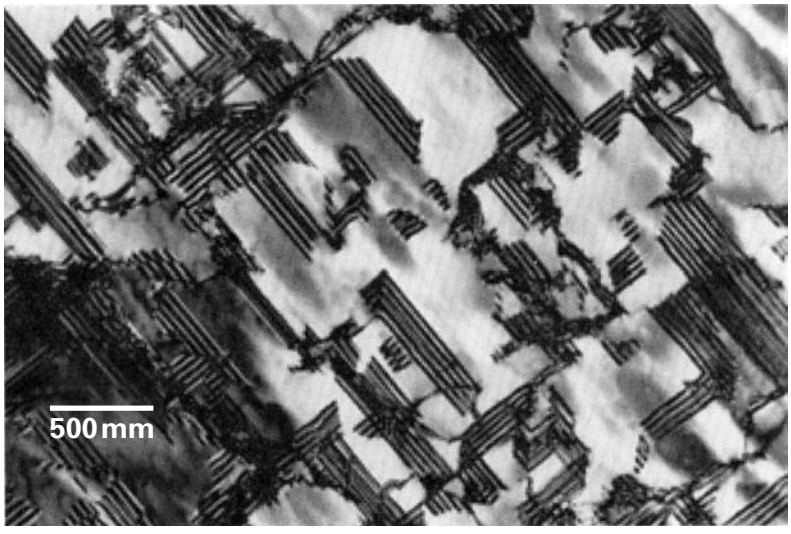

Fig. 4.46 Stacking faults in GaP. (Courtesy of P. Pirouz.)

films deposited on Si substrates by molecular beam epitaxy (MBE), chemical vapor deposition (CVD), or metal–organic CVD (MOCVD). Section 4.4.14 describes the stresses generated in epitaxial growth on a substrate. These mismatch stresses, as well as thermal stresses and growth faults, are responsible for the high concentration of stacking faults, which decreases with distance from the interface. Profuse stacking faults bounded by Shockley partial dislocations and stair-rod dislocations have been observed to occur in SiC grown on Si wafers. The configuration of stacking faults observed in SiC is analogous to that for GaP shown in Figure 4.46.

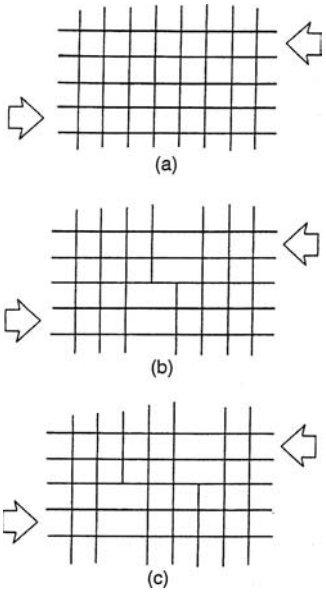

Fig. 4.47 Homogeneous nucleation of dislocation in conventional deformation.

4.4.8 Sources of Dislocations

It is experimentally observed that the dislocation density increases with plastic deformation; specifically, the relationship $\tau \propto \rho^{1/2}$ (see Chapter 6 Section 6.3) has been found to be closely obeyed. While the dislocation density of an annealed polycrystalline specimen is typically 10^7 cm^{-2}, a plastic strain of 10% raises this density to 10^{10} cm^{-2} or more, an increase of three orders of magnitude. This is an apparent paradox, because one would think that the existing dislocations would be ejected out of the crystalline structure by the applied stress. If one calculates the strain that the existing dislocations in an annealed metal would be able to produce by their motion until they would leave the crystal, one would arrive at very small numbers. Consequently, the density of dislocations has to increase with plastic deformation, and internal sources have to be activated. Some possible dislocation-generation mechanisms are discussed in the next few paragraphs.

The homogeneous nucleation of a dislocation occurs by in the rupture of the atomic bonds of a material along a certain line. Figure 4.47 shows schematically the sequence of steps leading to the formation of a pair of edge dislocations (one negative, one positive). In

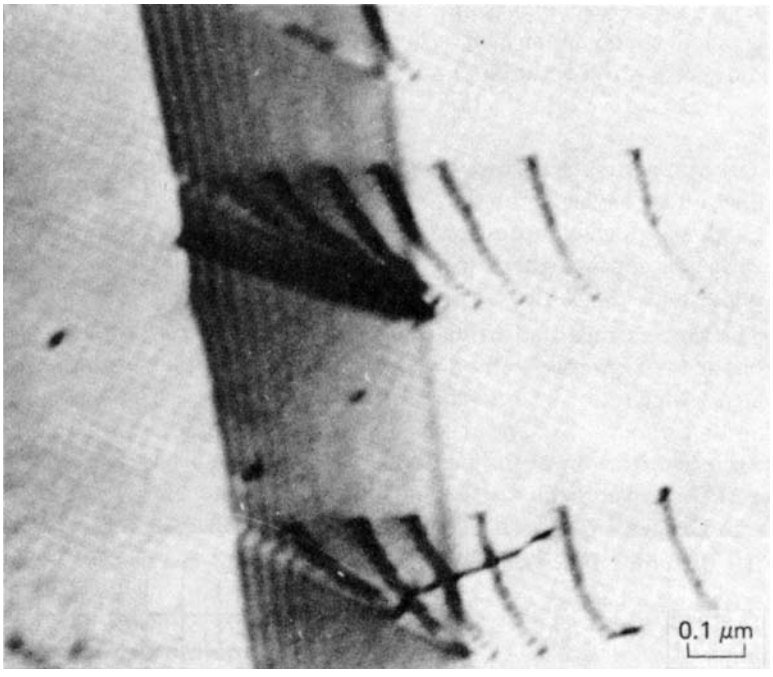

Fig. 4.48 Emission of dislocations from ledges in grain boundary, as observed in transmission electron microscopy during heating by electron beam. (Courtesy of L. E. Murr.)

Figure 4.47(a) the lattice is elastically stressed, until, in Figure 4.47(b), an atomic plane is sheared; this generates two dislocations that move in opposite senses. Such a mechanism allows the formation of dislocations from an initially perfect lattice. It can be seen intuitively that the stress required would be extremely high. Calculations were done by Hirth and Lothe (see the suggested reading), and for copper, this stress is on the order of

$$\frac{\tau_{\text{hom}}}{G} = 7.4 \times 10^{-2}.$$

Comparing this with the theoretical strength of crystals, one can see that the difference is not very large. Hence, such values would be obtained only if the applied stresses were very high or there were internal regions of high stress concentration. In conventional deformation, other dislocation-generation mechanisms should become operational at much lower stresses, rendering homogeneous nucleation highly unlikely.

Grain boundaries can serve as sources of dislocation. Irregularities at the boundaries (steps or ledges) could be responsible for the emission of dislocations into the grains. Figure 4.48 shows the emission of dislocations from a grain-boundary source; dislocations are seen as they are generated at the ledge. The stress due to heating produced by the electron beam produces the force on the dislocations. It is thought that dislocation emission from grain boundaries can be an important source of dislocations in the first stages of plastic deformation of a polycrystal.

In monocrystals, the surfaces can act as sources of dislocation. Small steps at the surfaces act as stress concentration sites; hence,

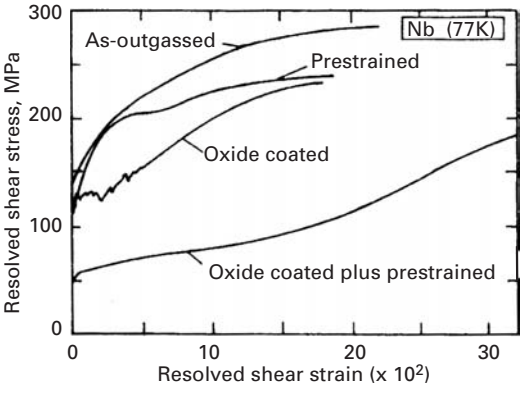

Fig. 4.49 Effect of oxide layer on the tensile properties of niobium. (Reprinted with permission from V. K. Sethi and R. Gibala, *Scripta Met.* 9 (1975) 527.)

the stress can be several times higher than the average stress. At these regions, dislocations can be generated and "pumped" into the monocrystals. The majority of dislocations in monocrystals deformed in tension are generated at the surface. Pangborn *et al.*[8] investigated the bulk and surface dislocation mechanism in monocrystals. The dislocation density close to the surface was up to six times greater than that in the bulk. The dislocation surface layer (with higher dislocation density) extended for approximately 200 μm into the material at the surface. The surface sources cannot have a significant effect on polycrystal deformation, because the majority of the grains would not be in contact with the free surface. Since dislocation activity is restricted to the grains, the surface sources would not be able to affect the internal grains. Incoherent interfaces between the matrix and precipitates, dispersed phases, or reinforcing fibers (in composites) are also sources of dislocations.

The importance of interfaces in the production of dislocations is seen in the results shown in Figure 4.49. The low-temperature tensile response of BCC metals was dramatically affected by the presence of an oxide layer. The figure exemplifies this response for niobium. The flow stress of monocrystalline niobium at 77 K is highly dependent on the state of the surface. The oxide softens the material. Two effects are responsible for the lowering of the flow stress by the introduction of an oxide layer:

1. The oxide puts the surface layers under tensile stresses, because the introduction of oxygen into the lattice expands it. On the other hand, the oxide is under compression. The resultant resolved shear stress at the surface is much higher (in the presence of the oxide layer) than that due exclusively to the externally applied load.
2. The predeformed and oxide-coated specimen (the lowest curve in the figure) has an even lower flow stress because the predeformation introduces surface steps, which act as stress-concentration sites.

[8] P. N. Pangborn, S. Weissman, and I. R. Kramer, *Met. Trans.* 12A (1981) 109.

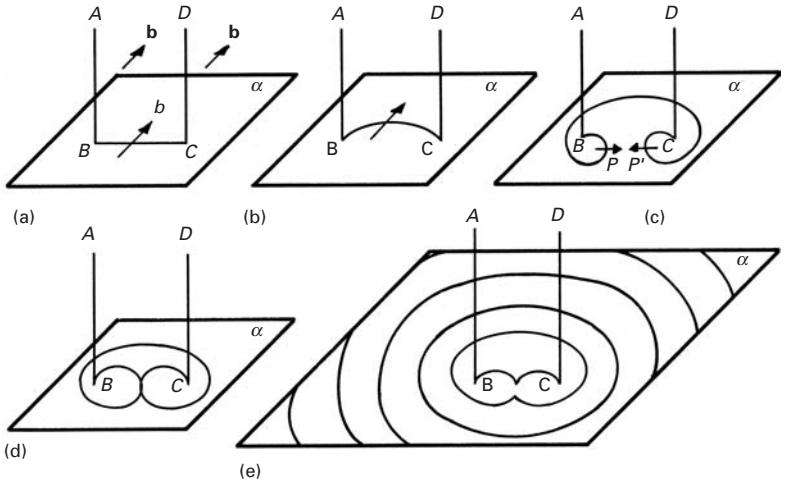

Fig. 4.50 Sequence of the formation of dislocation loop by the Frank–Read mechanism.

Hence, the joint action of the internal stresses generated by the oxide and the surface steps activates the dislocation sources at the surface.

The classic mechanism for dislocation multiplication is called the *Frank–Read source*. In Figure 4.50(a), there is a dislocation *ABCD* with Burgers vector *b*. Only the segment *BC* is mobile in the slip plane α. Segments *AB* and *CD* do not move under the imposed stress. The applied stress will generate a force per unit length on segment *BC* equal to (Section 4.45)

$$F = \frac{T\,ds}{R}.$$

The radius of curvature of the dislocation segment decreases until it reaches its minimum, equal to *BC*/2. At this point, the force is maximum (and so is the stress). Hence, the dislocation reaches a condition of instability beyond that point. The critical position is shown in Figure 4.45(c). When *P* approaches *P′*, the dislocation segments have opposite signs; accordingly, they attract each other, forming a complete loop when they touch, and are then pinched off. The stress required to activate a Frank–Read source is equal to that needed to curve the segment *BC* into a semicircle with radius *BC*/2; beyond this point, the stress decreases. Thus from Equation 4.22d:

$$\tau = \frac{Gb}{BC} = \frac{Gb}{2R}.$$

However, as loops are formed, they establish a back stress, so that the stress required to generate successive loops increases steadily. If the loops are expelled from the material, they cease to exert a back stress.

Only a few Frank–Read sources have been observed in metals. However, in a tridimensional array of dislocations, nodes define segments. These segments can bow and effectively act as Frank–Read sources. Another possibility is that the source forms when a screw dislocation cross-slips and returns to a plane parallel to the original slip

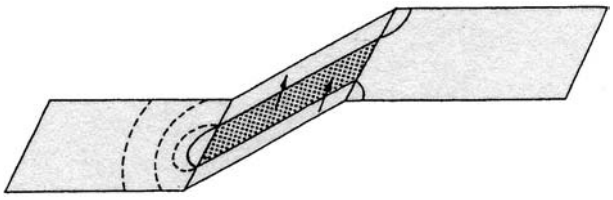

Fig. 4.51 Frank–Read source formed by cross-slip.

plane. (See Figure 4.51.) Incidentally, edge dislocations cannot cross-slip because their Burgers vector could not be contained in the cross-slip plane. The Burgers vector of a screw dislocation, on the other hand, is parallel to its line and will be in the cross-slip plane if the intersection of the two dislocations is parallel to it. After the segment in the cross-slip plane advances a certain extent, the stress system applied might force it into a plane parallel to the original slip plane. At this point, a Frank–Read source is formed. Although it is thought that the original formulation of the Frank–Read source is not common, its modifications just cited – the node and the cross-slip case – might be the important mechanism of dislocation generation, after the first few percent of plastic strain.

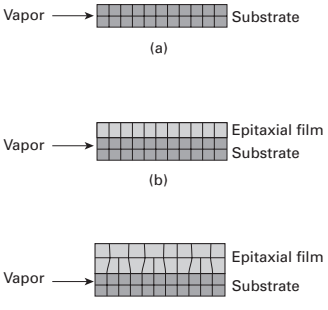

Fig. 4.52 Epitaxial growth of thin film. (a) Substrate. (b) Start of epitaxial growth. (c) Formation of dislocations.

Crystals formed by growth over a substrate (a technique commonly employed in the production of thin films) show dislocations whose formation can be easily explained. The substrate never has exactly the same lattice parameter as the crystal overgrowth. Figure 4.52 shows the sequence of formation of dislocations as the crystal grows over the substrate. If a_s and a_0 are the lattice parameters of the substrate and overgrowth, respectively, the separation between the dislocations is

$$d = \frac{a_s^2}{|a_s - a_0|}.$$

Often, the impurity content of a crystal varies cyclically due to solidification; this is called *segregation*. The periodic change in composition is associated with changes in the lattice parameter, which can be accommodated by dislocation arrays.

Vacancies can condense and form disks as well as prismatic loops if they are present in a "supersaturated" concentration. In FCC crystals, these disks and loops occur on {111} planes. As seen in Figure 4.39, the dislocations that form the edges of these features are called *Frank dislocations*. Kuhlmann–Wilsdorf (see suggested reading) proposed, that they can act as Frank–Read sources, and this was later confirmed experimentally.

4.4.9 Dislocation Pileups

All dislocations generated by a Frank–Read source are in the same slip plane if they do not cross-slip. In metals with low stacking-fault energy, the large separation between the partials renders cross-slip more difficult. In case one of the dislocations encounters an obstacle (a grain boundary, a precipitate, etc.), its motion will be hampered.

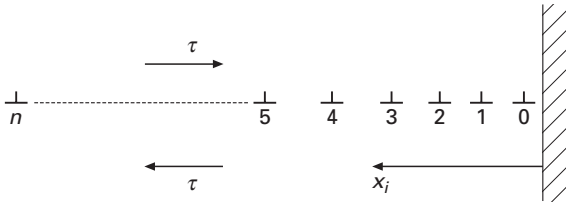

Fig. 4.53 Pileup of dislocations against a barrier.

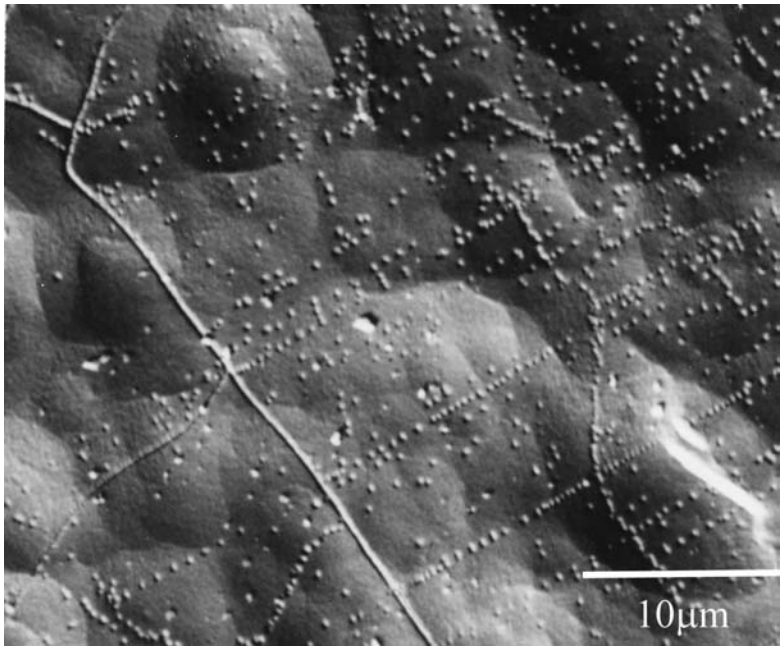

Fig. 4.54 Pileup of dislocations against grain boundaries (or dislocations being emitted from grain-boundary sources?) in copper observed by etch pitting.

The subsequent dislocations will "pileup" behind the leading dislocation, after being produced by the Frank–Read source. Figure 4.53 is a schematic diagram of a pileup. The distance between the dislocations increases as their distance from the obstacle increases. On the other hand, if the metal has a very high stacking-fault energy, cross-slip will easily occur, and the planar array will be destroyed; edge dislocations cannot, obviously, cross-slip because of their Burgers vector.

Figure 4.54 shows an example of a pileup, obtained by etch pitting in copper. Observe that the dislocation configurations for a pileup and a grain-boundary source are similar and that many grain-boundary sources have in the past been mistaken for pileups. Figure 4.48 shows a grain-boundary source.

Each dislocation in a pileup is in equilibrium under the effect of the applied stress and of the stresses due to the other dislocations (in the pileup). Assuming that the dislocations are of edge character and parallel, the resulting force acting on the ith dislocation is obtained

by applying the equation that gives the forces between dislocations:

$$\tau b - \sum_{\substack{j=0 \\ i \neq j}}^{n} \frac{G b^2}{2\pi(1-\nu)(x_i - x_j)} = 0. \tag{4.25}$$

n is the number of dislocations in the pileup.

Solving the n equations with n unknowns $(x_i - x_j)$ for the dislocations behind the lead dislocation, we obtain the positions of the dislocations. This derivation was introduced by Eshelby *et al*.[9] and we present the results without derivation.

The stress acting on the lead dislocation due to the presence of the other dislocations and due to the applied stress is found to be

$$\boxed{\tau^* = n\tau.} \tag{4.26}$$

So the effect of the n dislocations in the pileup is to create a stress at the lead dislocation n times greater than the applied stress. For this reason, the dislocation pileup is sometimes treated as a superdislocation with a Burgers vector nb. The foregoing calculations can also be applied to screw dislocations by removing the term $(1 - \nu)$. The length of the pileup under an applied shear stress τ is given by

$$L = \frac{nG b}{\pi \tau}. \tag{4.26a}$$

4.4.10 Intersection of Dislocations

A dislocation, when moving in its slip plane, encounters other dislocations, moving along other slip planes. If we imagine the first dislocation moving in a horizontal plane, it will "see" the other dislocations as "trees" in a "forest." The latter name designates dislocations in other slip planes. When the dislocation intersects another dislocation, since it shears the material equally (by a quantity b) on the two sides of the slip plane, it will form one or more steps. These steps are of two types: *jogs* if the "tree" dislocation was transferred to another slip plane, and *kink* if the "tree" dislocation remains in the same slip system. Various possible outcomes from dislocation intersections are shown in Figure 4.55. Figure 4.55(a) shows an edge dislocation traversing a "forest" composed of two edge and one screw dislocation. A good rule to determine the direction of jogs and kinks is the following: The direction of the segment is the same as the Burgers vector of the dislocation that is traversing the "forest;" on the other hand, the Burgers vector of the jog or kink is the Burgers vector of the dislocation in which it is located, because the Burgers vector is always the same along the length of a dislocation. Figure 4.55(b) shows a screw dislocation after traversing a "forest." The reader is asked to verify the directions of dislocation segments and Burgers vector; he or she should also verify whether they are jogs or kinks.

The ability of these segments to slip with a dislocation is of great importance in determining the work-hardening of metal. It should

[9] J. D. Eshelby, F. C. Frank, and F. R. N. Nabarro, *Phil. Mag*., 42 (1951) 351.

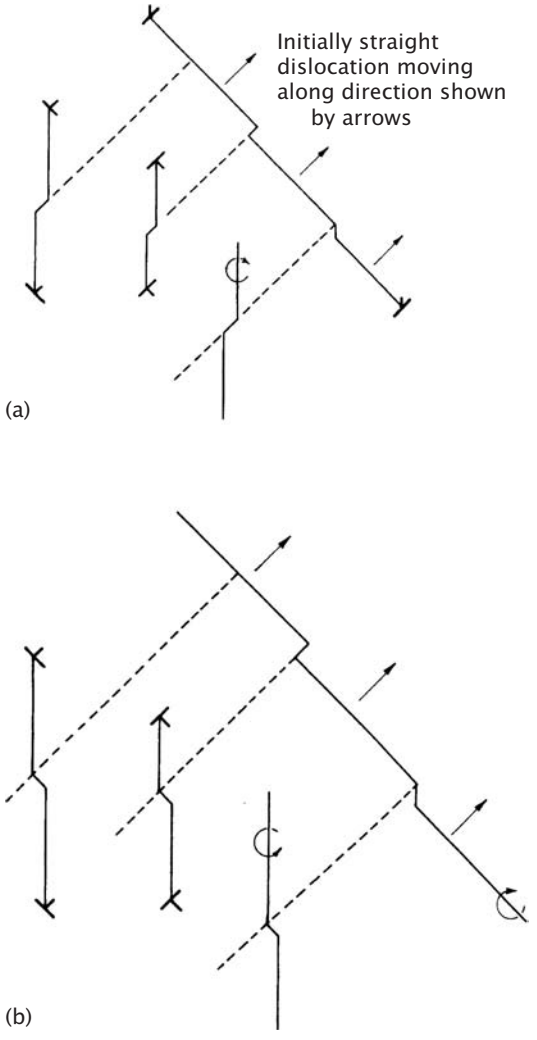

Fig. 4.55 (a) Edge dislocation traversing "forest" dislocations. (b) Screw dislocation traversing "forest" dislocations.

be noted that some authors use the name "jog" for both types of segments. Jogs and kinks can have either a screw or an edge character. From Figure 4.56(a), it can be seen that segments on an edge dislocation cannot impede the motion of jogs or kinks, because the segments can slip with the dislocation. On the other hand, in screw dislocations, there are segments that can slip with the dislocations and segments that cannot. When the segment can move with the dislocation, the motion is called *conservative*. When the segment cannot move by slip, the motion is called *nonconservative*. Figure 4.56(b) shows some interactions. At the left there is a conservative motion by slip, and at the right a nonconservative motion. The nonconservative motion of a jog is, in essence, a climb process and requires thermal activation. Vacancies or interstitials are produced as the segment moves. If the temperature is not high enough to provide sufficient thermal activation, the jog does not move, and loops are formed as the dislocation advances; this is shown in Figure 4.57. The

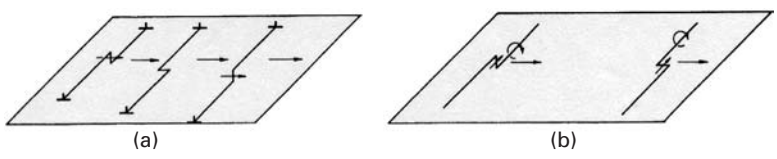

Fig. 4.56 (a) Kink and jog in edge dislocation. (b) Kink and jog in screw dislocation.

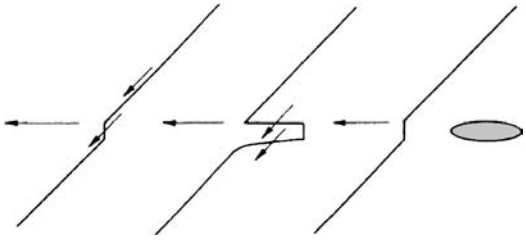

Fig. 4.57 Loop being pinched out when jog is left behind by dislocation motion.

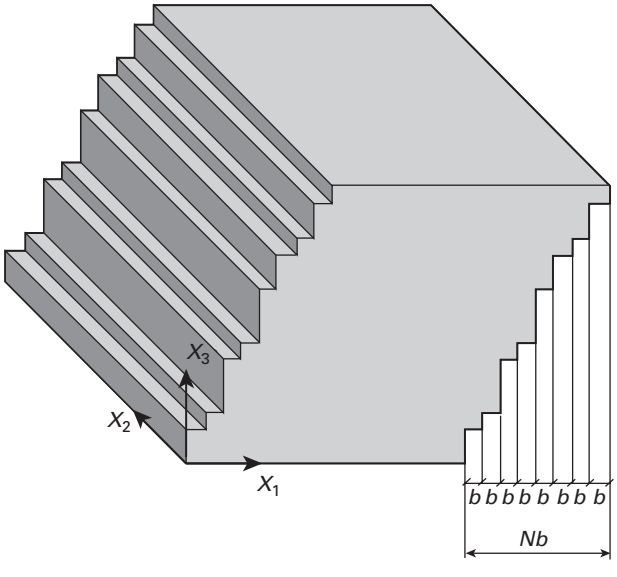

Fig. 4.58 Shear produced by the passage of parallel dislocations.

dislocation forms a dipole upon advancing, because the jog stays back. At a certain point, the dipole will be pinched out, producing a loop.

4.4.11 Deformation Produced by Motion of Dislocations (Orowan's Equation)

Upon moving, a dislocation produces a certain deformation in a material. This deformation is inhomogeneous. Figure 4.58 shows the steps generated by the passage of dislocations. If we consider a large number of dislocations acting on different systems, we can posit the association of a large number of small steps as creating a homogeneous state of deformation. The deformation is related to both the number of dislocations that move and the distance traveled by them. This equation is known as *Orowan's* or *Taylor–Orowan's equation* and is derived in this section. Figure 4.58 shows a cube dimensions dx_1, dx_2, and dx_3 that was sheared by the passage of N dislocations moving

along the plane Ox_1x_2. The plastic shear strain can be expressed as

$$d\gamma_{13} = \frac{N b}{dx_3}. \tag{4.27}$$

This is so because all dislocations are of edge character and have the same sign, with identical Burgers vector b. The density of dislocations, ρ, is the total length $N\,dx_2$ in the volume $dx_1\,dx_2\,dx_3$. Therefore,

$$\rho = \frac{N\,dx_2}{dx_1\,dx_2\,dx_3} \quad \text{and} \quad N = \rho\,dx_1\,dx_3. \tag{4.28}$$

Substituting Equation 4.28 into Equation 4.27 yields

$$d\gamma_{13} = \rho b\,dx_1.$$

A cube isolated in space, in which dislocations are generated on one face and pop out of the opposite face is an idealization. In real situations, dislocations remain within the material, and the deformation generated by each dislocation is related to the distance traveled by it. Assuming that dislocations travel an average distance, $\bar{l}$, we have

$$\boxed{\gamma_{13} = \rho b \bar{l}.}$$

But in a general case of deformation, five independent slip systems are activated. The deformation is not perfectly aligned with the movement of dislocations, and it is necessary to introduce a correction parameter k that takes this into account:

$$\gamma_p = k\rho b \bar{l}. \tag{4.29}$$

This is the Orowan equation. If one assumes that the density of mobile dislocations is not affected by the rate of deformation (strain rate), one would have, taking the time derivative of both sides of Equation 4.29,

$$\frac{d\gamma_p}{dt} = k\rho b \frac{d\bar{l}}{dt} + k\bar{l} b \frac{d\rho}{d\bar{l}}. \tag{4.30}$$

If we assume that ρ does not vary with time,

$$\boxed{\gamma_p = k\rho b \bar{v},}$$

where $\bar{v}$ is the mean velocity of the dislocations. We can also use the longitudinal strain ε_{11} if we are applying the situation to a tensile test. It can be shown that $\gamma = 2\varepsilon$ (see Section 6.2.3) for an ideal orientation for slip.

As an illustration, if iron ($b \approx 0.25$ nm) is being deformed at 10^{-3} s^{-1}, and the density of mobile dislocations is around 10^{10} cm^{-2}, their approximate velocity will be 4×10^{-6} cm/s.

Attention should be called to the fact that the density of mobile dislocations is lower than the total density of dislocations in the material. As the dislocation density increases in a deformed material, a greater and greater number of dislocations is locked by various types of barriers, such as grain boundaries, cell walls, or the action

of a great number of jogs. The actual density of mobile dislocations is only a fraction of the total dislocation density.

Example 4.6

Titanium is deformed by basal slip with edge dislocations. If a cube with one of its sides parallel to the *c*-axis is being deformed by shear through the passage of dislocations on every fifth (0001) plane, what shear strain γ is the cube undergoing? Take the radius of Ti atom

$$r_{Ti} = 0.147\,\text{nm}.$$

Solution: We first determine

$$a = 2r = 0.294\,\text{nm}.$$

We assume an ideal c/a ratio equal to 1.633. Thus, $c = 0.48$ nm. The Burgers vector for basal slip is equal to a.

Every fifth atomic plane corresponds to a distance $d = 5c = 2.4$ nm. The shear strain is thus equal to

$$\gamma = \frac{b}{d} = \frac{0.294}{2.4} = 0.1225.$$

Example 4.7

An FCC monocrystal of nickel is sheared by $\gamma_{12} = 0.1$. Assuming that the dislocation density is equal to 10^8 cm^{-2} and that it remains constant, what is the average distance each dislocation will have to move? If the shear strain rate is 10^{-4} s^{-1}, what is the mean velocity of the dislocation?

Solution:

$$r_{\text{Ni}} = 0.125\ \text{nm}$$

For FCC, $b = 2r_{Ni} = 0.250$ nm. Using Orowan's equation, taking k = 1, $\gamma = \rho b\bar{l}$, we obtain the following:

(i) $$\bar{l} = \frac{\gamma}{\rho b}$$
$$= \frac{0.1}{10^8\ \text{cm}^{-2} \times 0.25\ \text{nm}}$$
$$= \frac{0.1}{10^8 \times (10^4\,\text{m}^{-2}) \times 0.25\,(10^{-9}\ \text{m})} = 4 \times 10^{-4}\ \text{m}$$

(ii) $\dot{\gamma} = \rho b\bar{v}$,

so

$$\bar{v} = \frac{\dot{\gamma}}{\rho b}$$
$$= \frac{10^{-4} s^{-1}}{10^8\,\text{cm}^{-2} \times 0.25\ \text{nm}} = 4 \times 10^7\ \text{m/s}.$$

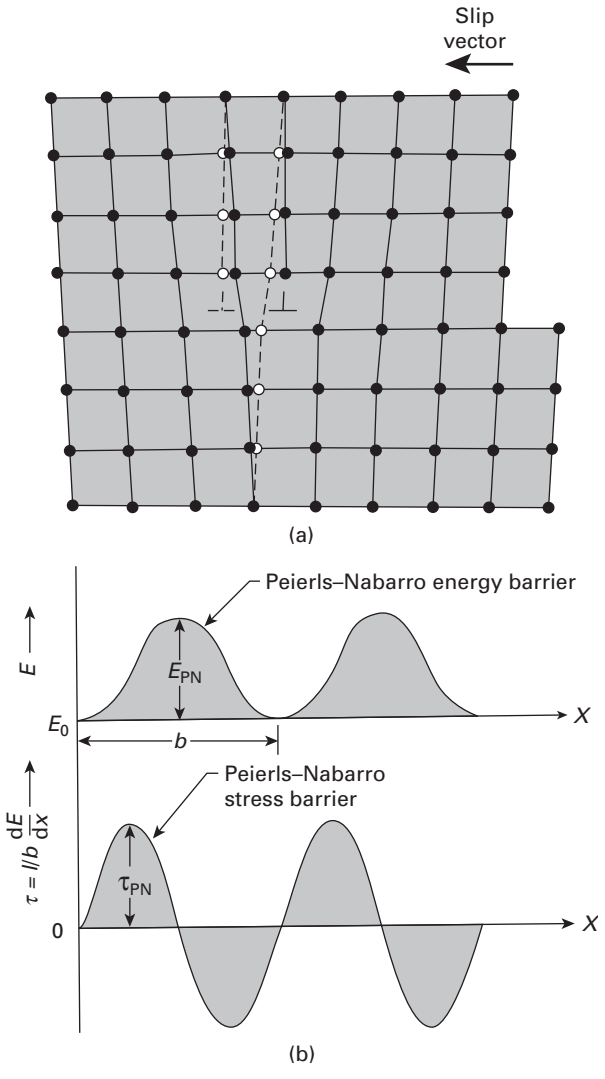

Fig. 4.59 (a) Movement of dislocation away from its equilibrium position. (b) Variation of Peierls–Nabarro stress with distance. (Reprinted with permission from H. Conrad, *J. Metals*, 16 (1964) 583.)

4.4.12 The Peierls–Nabarro Stress

The Peierls–Nabarro stress represents the resistance that the crystalline lattice offers to the movement of a dislocation. Figure 4.59 shows the stress that one has to apply to a dislocation to make it move a distance b. When the extra plane is moved away from its equilibrium position (either to the right or to the left), one has to overcome a barrier. The difference in energy between the equilibrium (saddle point) and the most unstable position is called the *Peierls–Nabarro energy*, and the stress required to overcome this energy barrier is the *Peierls–Nabarro (P–N)* stress. The dislocation does not advance simultaneously over its entire length. (See Figure 4.60(a).) Rather, a small hump, or kink pair is formed, as shown in Figure 4.60(b), via what is known as a Seeger mechanism. This kink pair then moves along the dislocation (the parts of the pair move in opposite directions), and when it has covered the entire front, the dislocation has advanced by

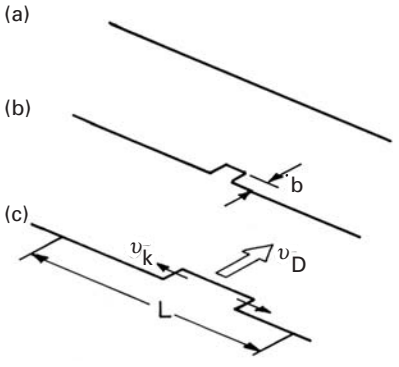

Fig. 4.60 Overcoming of Peierls barrier by Seeger kink pair mechanism. (a) Original straight dislocation. (b) Dislocation with two kinks. (c) Kinks moving apart at velocity v_k.

b, the Burgers vector. In Figure 4.60(c) the velocity of movement of a dislocation is v_D, related to the kink velocity v_k by

$$v_D = v_k \frac{b}{L}. \tag{4.31}$$

The stress required to overcome the obstacle is known as the Peierls–Nabarro stress. Calculations of this stress are fairly inaccurate because the continuum treatment breaks down for distances on the order of the atomic spacings. The energy of the dislocation is given by $U(x)$ as it moves through the barrier. The applied force required to bring this dislocation to the top of the energy barrier is

$$F = -\frac{dU}{dx}. \tag{4.32}$$

But from the Peach–Koehler equation ($F = \tau b$), we have

$$\tau = -\frac{1}{b}\frac{dU}{dx}. \tag{4.33}$$

A sinusoidal form for $U(x)$ was assumed by Peierls and Nabarro, leading to the expression

$$\tau_{PN} = \alpha \frac{G b}{2c} e^{-\pi a/c} \sin \frac{2\pi x}{c}, \tag{4.34}$$

where c is the spacing of atoms in the x direction, a is the lattice parameter, and α is a parameter that depends on the nature of the barrier; for $\alpha = 1$, the barrier is sinusoidal.

4.4.13 The Movement of Dislocations: Temperature and Strain Rate Effects

The resistance of crystals to plastic deformation is determined by the resolved shear stress that is required to make the dislocations glide in their slip planes. If no obstacles were present, the dislocations would move under infinitesimally small stresses. However, in real metals, the nature and distribution of obstacles determines their mechanical response. Becker[10] was the first to point out the importance of thermal energy in helping the applied stress overcome existing obstacles.

[10] R. Becker, *Z. Phys.* 26 (1925) 919.

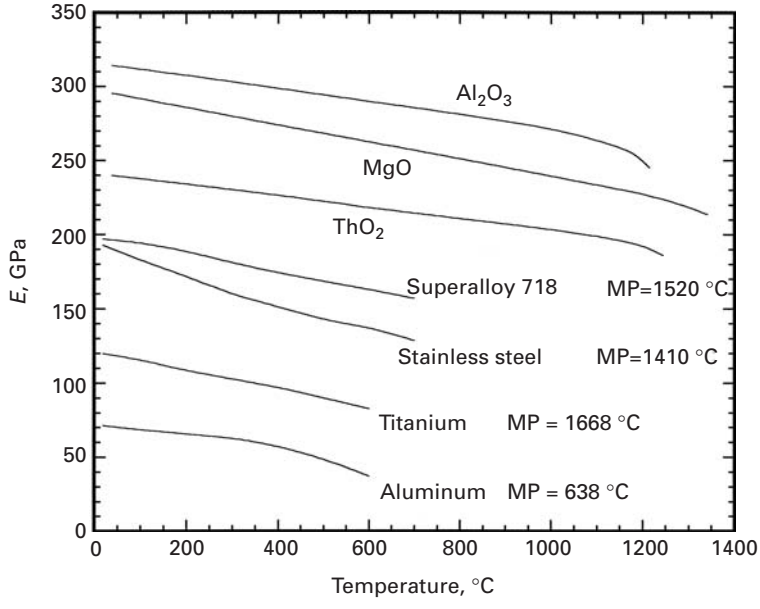

Fig. 4.61 Effect of temperature on Young's modulus. (Adapted from J. B. Wachtman Jr., W. E. Tefft, D. G. Lam, Jr., and C. S. Apstein, *J. Res. Natl. Bur. Stand.*, 64A (1960) 213; and J. Lemartre and J. L. Chaboche, *Mechanics of Solid Materials*, Cambridge: Cambridge University Press, 1990, p. 143.)

The stress required for deformation, τ, can be divided into two parts: τ^*, which is dependent on the strain rate and temperature of the material, and τ_G, in which the temperature dependence is equal to that of the shear modulus. Thus,

$$\tau = \tau^* + \tau_G\,, \tag{4.35}$$

or, in terms of the normal stresses,

$$\sigma = \sigma^* + \sigma_G\,. \tag{4.36}$$

The functional dependence can be expressed as

$$\sigma = \sigma^*(T\,, \dot{\varepsilon}) + \sigma_G(G\,). \tag{4.37}$$

We know that the elastic properties (E, G, ν) are only slightly dependent on temperature. Figure 4.61 shows the temperature dependence of Young's modulus for a number of materials. As the temperature increases, the amplitude of vibration of the atoms increases (but the frequency remains constant at approximately 10^{13} s^{-1}). This results in thermal dilation, which separates the atoms somewhat and changes their equilibrium positions and interatomic forces. The flow stress of metals, on the other hand, is much more sensitive to temperature and strain rate. Figure 4.62 shows the dependence of the yield stress on temperature for typical BCC and FCC structures. BCC metals (Fe, Cr, Ta, W, etc.) exhibit a greater temperature and strain rate sensitivity. It can be seen that the athermal component of stress is $\sigma_G \approx 50$ MPa, whereas the thermal component exceeds 1,000 MPa at 0 K. The increase in flow stress with decrease in temperature is much more gradual for FCC metals, as shown in Figure 4.62(c). The differences in temperature and strain rate sensitivity are due to different mechanisms controlling the rate of dislocation motion. In BCC metals,

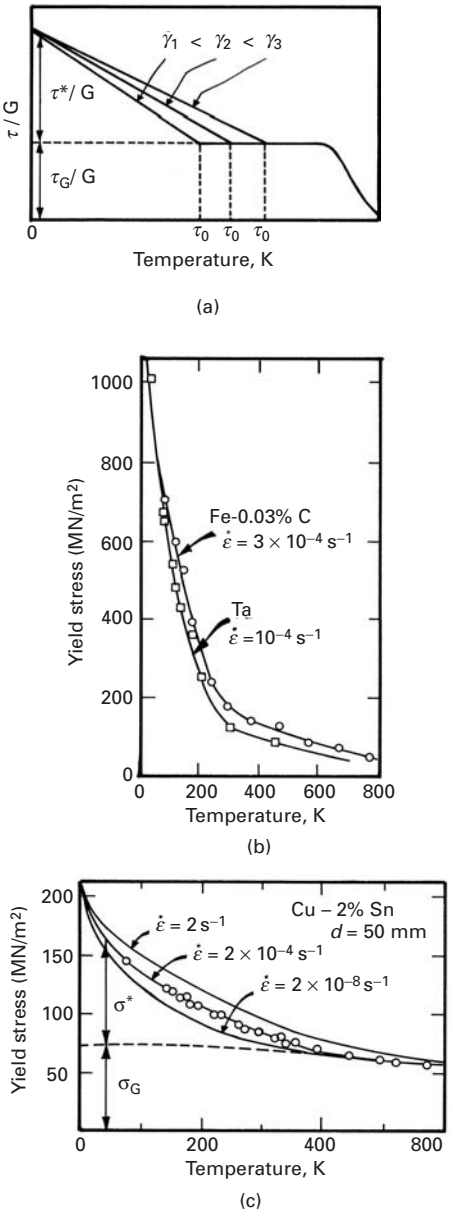

Fig. 4.62 Flow stress as a function of temperature for (a) an idealized material, (b) BCC metals, and (c) FCC metals. Notice the greater temperature dependence for Ta and Fe (BCC).

Peierls–Nabarro stresses are the major obstacles at low temperatures, and thermal energy can effectively aid the dislocations to overcome these stresses, which constitute a short-range barrier. For FCC metals, dislocations intersecting dislocations ("forest" dislocations) are the main barriers to the motion of dislocations. Thermal energy is less effective in helping dislocations to overcome these barriers.

At temperatures higher than 800 K, there is an additional drop in the flow stress, not shown in Figure 4.62. This drop occurs at $T \approx 0.5\ T_m$, where T_m is the melting point of the metal (or alloy). The drop is due to creep, which often involves dislocation climb. Creep is treated separately in Chapter 13.

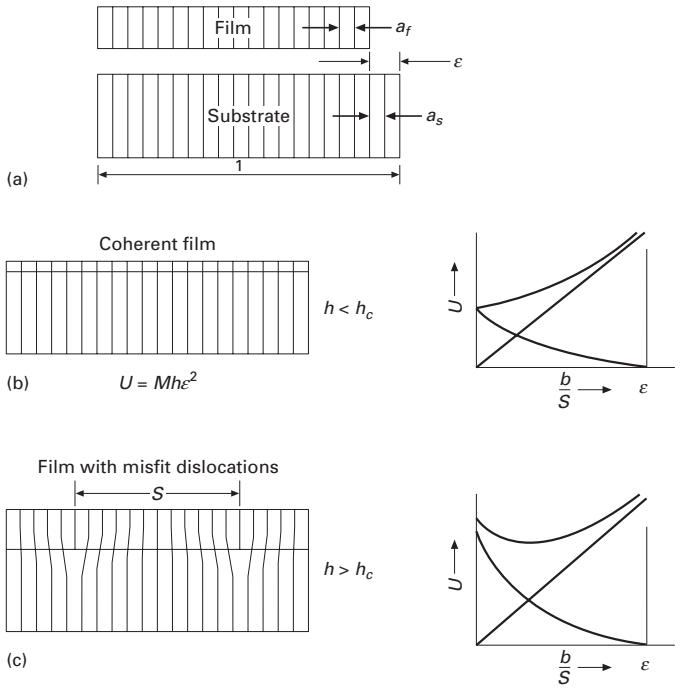

Fig. 4.63 Stresses and dislocations generated at film–substrate interface; (a) film and substrate with different lattice parameters; (b) elastic (coherent) accommodation of strains by film; (c) elastic + dislocation (semi-coherent) accommodation of strains at a film thickness greater than h_c. (Adapted from W. D. Nix, *Met. Trans.*, 20A (1989) 2217.)

Johnston and Gilman[11] were the first to measure the velocities of dislocations as a function of applied stress. They used LiF crystals for their measurements and observed, as expected, that the distance a dislocation moves increases with the magnitude and duration of the stress pulse. The distance also increases, at a constant stress, with increasing temperature. This relationship is known as the Johnston–Gilman equation and has the form

$$\boxed{v = A\tau^m e^{-Q/RT},} \tag{4.38}$$

where v is the dislocation velocity, exponent m is a stress dependency that is dependent on v, Q is an activation energy, and A is a pre-exponential term that depends on the material and the nature of the dislocation (edge or screw). Although this equation predicts an infinite dislocation velocity when the stress is high, it is generally accepted that the limiting dislocation velocity is the velocity of elastic shear waves. Thus, the equation breaks down at velocities close to the shear wave velocity (e.g., ~3,000 m/s for iron).

4.4.14 Dislocations in Electronic Materials

Producing dislocation-free substrates and epitaxial films is an important technological consideration. The presence of dislocations creates a barrier for electric fields and alters electronic properties of thin films. It is therefore undesirable. In order for epitaxial thin films to be stress free, they must have the same lattice parameter as the substrate. Figure 4.63(a) shows a film and substrate, with lattice parameters a_f and a_s, respectively. They are shown separately. If they

[11] W. G. Johnston and J. J. Gilman, *J. Appl. Phys.* 33 (1959) 129.

are connected, stresses will arise. The substrate is usually much thicker than the film. Thus, the elastic accommodation is assumed to occur entirely in the substrate. The epitaxial strain is:

$$\varepsilon = \frac{\Delta a}{a} \approx \frac{a_s - a_f}{a_s}.$$

We present below the van der Merwe[12]–Matthews[13] theory for the prediction of thin film configurations. The strain energy, in the case where the substrate is completely coherent with the film, is:

$$U_h = \frac{E}{1-\nu} h\varepsilon^2. \tag{4.39}$$

where h is the thickness of the thin film; the term $E/(1-\nu)$ is the biaxial modulus (see Section 2.16). It can be obtained from the generalized Hooke's law assuming a biaxial stress state. As the thickness of the film increases, the strain energy increases, due to the factor h in Equation 4.39. At first, the film is coherent with the substrate. This is shown in Fig. 4.63(b). When the strain energy reaches a critical level, misfit dislocations are created, decreasing the overall strain. Figure 4.63(c) shows a film with dislocations having a spacing S. The homogeneous strain is decreased from ε to $(\varepsilon - b/S)$ due to the insertion of dislocations, spacing S, with displacement (Burgers vector) b. However, the dislocations created have an energy U_d that has to be factored in. For misfit edge dislocations with a spacing S:

$$U_d = \frac{G b^2}{4\pi(1-\nu)} \frac{2}{S} \ln\left(\frac{h}{b}\right). \tag{4.40}$$

The misfit dislocations form a two-dimensional network. The term $2/S = 1/S + 1/S$ represents the length of misfit dislocations per unit area (square grid). The total strain energy Ut is obtained by adding Equations 4.39 (after subtracting the b/S term) and 4.40:

$$U_t = \frac{E}{1-\nu} h \left(\varepsilon - \frac{b}{S}\right)^2 + \frac{G b^2}{4\pi(1-\nu)} \frac{2}{S} \ln\left(\frac{h}{r_o}\right). \tag{4.41}$$

In Figure 4.63, the two plots on the right side represent the energy in the case of coherent and semicoherent interface. In the coherent case, the energy is minimum for an infinite spacing of dislocations ($b/S = 0$). However, as the thickness h of the film is increased, the second term (logarithmic in h) increases in importance. The energy reaches a minimum when critical thickness h_c is reached. This corresponds to the thickness at which dislocations are created at the interface. This is represented by the plot in Figure 4.63(c).

We can calculate the critical film thickness, h_c by taking the derivative of Equation 4.41 with respect to $1/S$:

$$\frac{\partial U_t}{\partial (1/S)} = -2\frac{E}{1-\nu}\left(\varepsilon - \frac{b}{S}\right) + \frac{G b^2}{2\pi(1-\nu)} \ln\left(\frac{h}{b}\right) = 0. \tag{4.42}$$

[12] J. H. van der Merwe and N. G. van der Berg, *Surface Science*, 32 (1972) 1.
[13] J. W. Matthews and A. E. Blakeslee, *Journal of Crystal Growth*, 27 (1974) 118; 29 (1975) 273.

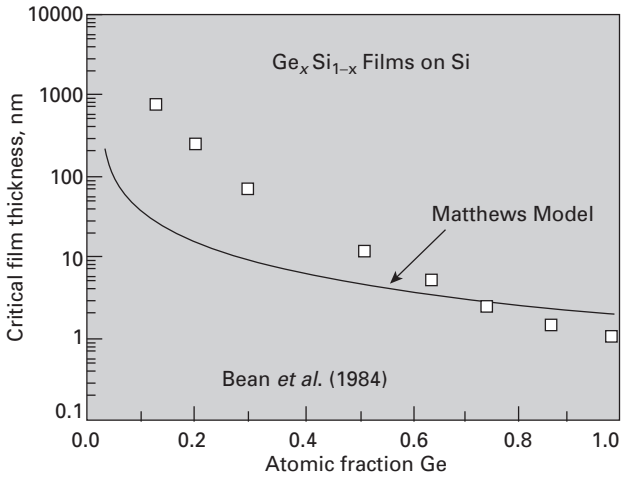

Fig. 4.64 Critical film thickness as a function of misfit strain for Ge_xSi_{1-x} film grown on Si substrate; the greater fraction Ge_x, the greater the misfit stain and the smaller h_c. Predictions from van der Merwe–Matthews theory; measurements from J. C. Bean, L. C. Feldman, A. T. Fiory, S. Nakahara, and I. K. Robinson, *J. Vac. Sci. Technol. A*, 2 (1984) 436. (Adapted from W. D. Nix., *Met. Trans*., 20A (1989) 2216.)

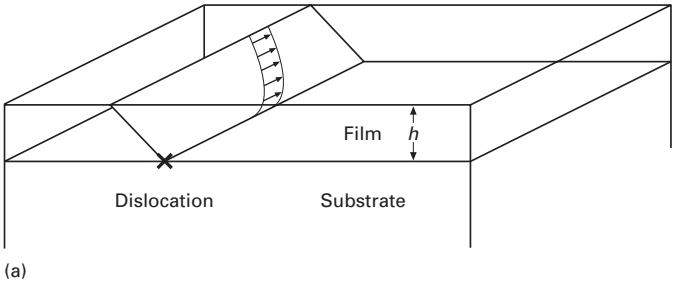

(a)

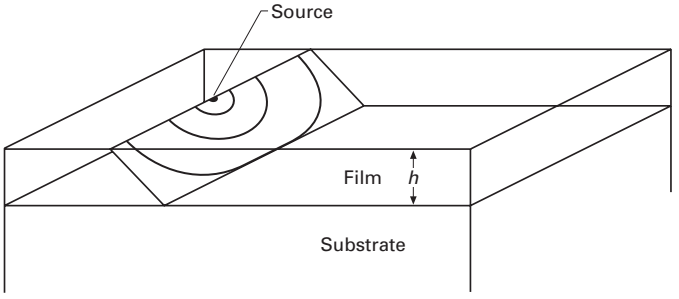

(b)

Fig. 4.65 Mechanisms of misfit dislocation generation; (a) Freund mechanism in which a "threading" dislocation preexisting in substrate lays over interface creating misfit dislocation; (b) Nix mechanism, by which surface source creates half-loops that move toward interface.

By setting $1/S = 0$, i.e., an infinite dislocation spacing, we obtain the Matthews–Blakeslee equation:

$$\boxed{\frac{h_c}{\ln\left(\frac{h_c}{\nu_0}\right)} = \frac{G\,b}{4\pi\,E\,\varepsilon} = \frac{b}{8\pi(1+\nu)E}} \tag{4.43}$$

Figure 4.64 shows the critical film thickness for Ge_xSi_{1-x} growth on a Si substrate. The higher the fraction x of Ge, the larger the strain in the film, ε. Consequently, the smaller will be h_c. The predictions of Equation 4.43 are compared with experimental results in Figure 4.64. The agreement is only qualitatively satisfactory. For small strains, the predicted thickness is orders of magnitude lower than the observed value.

One of the reasons for the difference is that dislocations cannot appear spontaneously at the interface, once a critical thickness is reached. They have to nucleate somewhere and move to the interface. This requires additional energy. Two possible mechanisms are shown in Figure 4.65. The Freund mechanism requires an existing dislocation that "threads" through substrate and film. This threading dislocation, moving along the interface as shown in Figure 4.65(a), creates the interface dislocation. The Nix mechanism requires a dislocation to be formed at the free surface and move to the interface. A source, operating at the surface, is shown in Figure 4.65(b). It produces half-loops, which expand and reach the interface.

Suggested Reading

Point Defects

C. S. Barrett and T. B. Massalski. *Structure of Metals*, 3rd ed. New York, NY: McGraw-Hill, 1966.

J. H. Crawford Jr. and L. M. Slifkin, eds. *Point Defects in Solids*. New York, NY: Plenum Press, 1972.

A. C. Damask and G. J. Dienes. *Point Defects in Metals*. New York, NY: Gordon and Breach, 1963.

C. P. Flynn. *Point Defects and Diffusion*. Oxford: Clarendon Press, 1972.

H. Kimura and R. Maddin. *Quench Hardening in Metals*, in the series "Defects in Crystalline Solids," S. Amelincx, R. Gevers, and J. Nihoul, eds. Amsterdam: North-Holland, 1971.

A. S. Nowick and B. S. Berry. *Anelastic Relaxation in Crystalline Solids*. New York, NY: Academic Press, 1972.

H. G. Van Bueren. *Imperfections in Crystals*. Amsterdam: North-Holland, 1961.

Line Defects

A. H. Cottrell. *Dislocations and Plastic Flow in Crystals*. Oxford: Clarendon Press, 1953.

J. C. Fisher, W. G. Johnston, R. Thomson, and T. Vreeland, Jr., eds. *Dislocations and Mechanical Properties of Crystals*. New York, NY: Wiley, 1957.

J. Friedel. *Dislocations*. Elmsford, NY: Pergamon Press, 1967.

J. P. Hirth and J. Lothe. *Theory of Dislocations*, 2nd ed. New York, NY: J. Wiley, 1981.

D. Hull and D. J. Bacon. *Introduction to Dislocations*. New York, NY: Oxford University Press, 1989.

A. Kelly and G. W. Groves. *Crystallography and Crystal Defects*. Reading, MA: Addison-Wesley, 1974.

I. Kovacs and L. Zsoldos. *Dislocations and Plastic Deformation*. Elmsford, NY: Pergamon Press, 1973.

D. Kuhlmann-Wilsdorf, in *Physical Metallurgy*, 3rd ed., R. W. Cahn and P. Haasen, eds. Amsterdam: North Holland, 1990, 1983.

J. P. Hirth and F. R. N. Nabarro, ed. *Dislocations in Solids*, (15 vols.). New York, NY: Elsevier/North-Holland, 1979–2008.

W. T. Read, Jr. *Dislocations in Crystals*. New York, NY: McGraw-Hill, 1953.

J. Weertman and J. R. Weertman. *Elementary Dislocation Theory*. New York, NY: Oxford University Press, 1992.

Exercises

4.1 Calculate the radii of the tetrahedral and octahedral holes in BCC and FCC iron; assume lattice parameters of 0.286 and 0.357 nm, respectively.

4.2 Calculate the concentration of monovacancies in gold at 1,000 K, knowing that $H_f = 1.4 \times 10^{-19}$ J. If the gold is suddenly quenched to ambient temperature, what will be the excess vacancy concentration?

4.3 How many vacancies per cubic centimeter are there in gold, at ambient temperature, assuming a lattice parameter of 0.408 nm?

4.4 What is the effect of vacancies on electrical conductivity?

4.5 What is the effect of vacancies on the amplitude of vibration of the neighboring atoms?

4.6 What stress is required to render operational a Frank–Read source in iron, knowing that the distance between points B and C is 20 (Figure 4.50) nm and that the Goldschmidt radius of the iron atoms is 0.14 nm?

4.7 Make all possible reactions between (perfect) dislocations in $(11\bar{1})$ and $(1\bar{1}\bar{1})$ in an FCC crystal. Among them, which ones are Lomer locks?

4.8 Consider all possible reactions between partial Shockley dislocations (only the front dislocation, from the pair) in (111) and $(11\bar{1})$ in an FCC crystal. Among them, which ones will form a stair-rod dislocation?

4.9

(a) Show that the reaction

$$\frac{a}{2}[10\bar{1}] \rightarrow \frac{a}{6}[21\bar{1}] + \frac{a}{6}[11\bar{2}]$$

is either vectorially correct or incorrect?

(b) Is the reaction energetically favorable?

4.10 10^7 and 10^{11} cm^{-2} are typical values for the dislocation density of annealed and deformed nickel, respectively. Calculate the average space among dislocation lines (assuming a random dislocation distribution), as well as the line energy for edge and screw dislocations, in both cases. In nickel, $E = 210$ GPa, $\nu = 0.3$, and the lowest distance between atom centers is 0.25 nm.

4.11 Calculate the dislocation density for Figure 4.22b; assume a foil thickness of 0.3 μm.

4.12 The concentration of vacancies in aluminum at 600 °C is 9.4×10^{-4}; by quenching, this concentration is maintained at ambient temperature. The vacancies tend to form disks, with Frank partials at the edges. Determine the loop concentration and dislocation density, assuming that:

(a) Disks with a 5-nm radius are formed.

(b) Disks with a 50-nm radius are formed.

For aluminum, assume that the radius of the atoms is 0.143 nm. (*Hint*: The length of the Frank dislocation corresponding to a disk is equal to the circumference of the circle.)

4.13 The flow stress of monocrystals is on the order of 10^{-4} G. Using the concept of Frank–Read sources, determine the length of segments required for this stress level. If the length of the segments is determined by dislocations on a second slip plane ("tree" dislocations), obtain an estimate for the dislocation density in annealed monocrystals. Assume that the dislocations are equally distributed on the slip planes of an FCC crystal.

4.14 On what planes of a BCC structure can the $a/2$ [111] move?

4.15 Upon encountering an obstacle, an edge dislocation stops. A second edge dislocation, with identical Burgers vector and moving in the same plane, approaches the first dislocation, driven by a stress equal to 140 MPa.

(**a**) What will be the equilibrium separation between the two dislocations? Assume that the metal is nickel ($E = 210$ GPa, $\nu = 0.3$, $r = 0.249$ nm).
(**b**) What would be the equilibrium separation if the dislocations were both screw dislocations?

4.16 LiF is an ionic crystal with a NaCl-type structure (cubic). The Li atoms occupy the vertices and the centers of the faces of the unit cell, while the F atoms occupy the edges, and one F atom is in the body-centered position. There are eight atoms per unit cell. Knowing that the slip plane for LiF is [110], determine the Burgers vector of a perfect dislocation. Remember that one has an ionic crystal and that there is a strong repulsion between ions of the same sign. Explain your results.

4.17 Draw a unit cell for an HCP crystal. Show the perfect dislocations in the base plane. Can they decompose into partials? If so, represent them by the special notation for dislocations.

4.18 Nickel sheet is being rolled at ambient temperature in a rolling mill (roll diameter 50 cm, velocity 200 rpm). See Figure 6.1 for sketch of rolling mill. The initial thickness is 20 mm and the final thickness is 10 mm (one pass).

(**a**) Calculate the average strain rate.
(**b**) Calculate the energy that will be stored in the material, assuming that the final dislocation density is 10^{11} cm^{-2}.
(**c**) Determine the total energy expenditure per unit volume, assuming a flow stress equal to 300 MPa.
(**d**) Assuming that all energy not stored as dislocations is converted into heat, calculate the temperature rise if the process is adiabatic ($C_p = 0.49$ J/g °C).
(**e**) Why does the energy stored represent only a fraction of the energy expended?

4.19 Calculate the largest atom that would fit interstitially into (a) nickel (FCC; atomic radius = 0.125 nm) and (b) molybdenum (BCC; atomic radius = 0.136 nm).

4.20 Calculate, for tungsten (BCC; atomic radius = 0.1369 nm), the radii of the largest atoms that can fit into (a) a tetrahedral interstitial site (at 0, 1/4, 1/2) and (b) an octahedral interstitial site (at 0, 1/2, 1/2).

4.21 If the enthalpy of formation for a vacancy is equal to 80 kJ/mol, what is the fraction of vacant sites at 1,500 K.

4.22 The lattice parameter of a BCC crystal was measured at ambient temperature and at 1,000 °C. The parameter showed an increase of 0.5% due to

thermal expansion. In the same interval of temperature, the density, measured by a separate method, showed a decrease of 2%.

(a) Assuming that, at room temperature, there is one vacancy per 1,000 atoms, what is the vacancy concentration at 1,000 °C?
(b) Calculate the activation energy necessary for the production of vacancies.

4.23 The Burgers vector of a dislocation is 0.25 nm in a crystal. The shear modulus $G = 40$ GPa. Estimate the dislocation energy per unit length in this crystal.

4.24 A dislocation is anchored between two points 10 μm distant. For a metal with $b = 0.35$ nm and $G = 30$ GPa, compute the shear stress necessary to bow the dislocation into a semicircle.

4.25 Consider an aluminum polycrystal with a grain size of 10 μm. If a dislocation source at the center of a grain emits dislocations under an applied shear stress of 50 MPa that pile up at the grain boundaries, what is the stress experienced by a grain boundary? Take $G = 26$ GPa and $b = 0.3$ nm.

4.26
(a) Iron ($r = 0.124$ nm, $G = 70$ GPa) is being deformed to a shear strain of 0.3. Assuming a constant dislocation density equal to 10^{10} cm^{-2}, what is the average distance each dislocation has to move?
(b) Assuming that the strain rate is 10^{-2} s^{-1}, what is the average dislocation velocity?

4.27 Aluminum ($r = 0.15$ nm, $G = 26$ GPa) is deformed to a shear strain of 0.5. A dislocation density equal to 10^{10} cm^{-2} results.

(a) What is the average distance each dislocation had to move?
(b) If the strain rate were 10^{-2} s^{-1}, what would be the average dislocation velocity?

4.28 Consider the following dislocation reaction in a face-centered cubic material:

$$\frac{a}{2}[1\bar{1}0] \rightarrow \frac{a}{6}[2\bar{1}1] + \frac{a}{6}[1\bar{2}\bar{1}].$$

Is it energetically favorable?

4.29 Consider dislocations blocked in gold. If the flow stress is controlled by the stress necessary to operate a Frank–Read source, compute the dislocation density ρ in the crystal when it is deformed to a point where the resolved shear stress on the slip plane is 45 MPa. Take $G = 27$ GPa.

4.30 Plot the stresses around a screw dislocation, in terms of isostress fields. Do a plot equivalent to the one in Figure 4.32 (edge dislocations).

4.31 Plot the energy of a single edge dislocation in copper as a function of dislocation density (in units of Gb^2). Start at a density of 10^6 cm^{-2}, characteristic of well-annealed material, and finish at 10^{11} cm^{-2}, characteristic of work-hardened material.

4.32 A dislocation segment is pinned by two obstacles at a distance of 10 μm. Calculate the stress required to bow this segment into a semicircle (this is equal to the stress required to activate a Frank–Read source). $b = 0.25$ nm; $G = 40$ GPa.

4.33 A tantalum polycrystal (grain size equal to 50 μm) is deformed to a total shear strain of 0.5 at a strain rate of 10 s^{-1}. Assume that dislocations cannot

cross grain boundaries. Given that $G = 10$ GPa, $b = 0.2$ nm, and assuming $k = 1$, calculate:

(a) The dislocation density required.
(b) The velocity at which each dislocation will move.

4.34 On eight cubes that have a common vertex, corresponding to the origin of axes, draw the family of {111} planes. Show that they form an octahedron and indicate all <110> directions.

4.35 How many vacancies per cubic centimeter are there in gold, at ambient temperature, assuming a lattice parameter of 0.408 nm? $G_v = 1.4 \times 10^{-19}$.

4.36 Burgers vector of a crystal generally lies in a close-packed direction. Why?

4.37 What is the ideal strength of a crystalline solid? What crystal imperfection allows the material to deform at much lower strength and why?

4.38 Do you think the addition of dislocations in a crystal changes its density? Explain your answer.

4.39 Describe in detail the effects of quenching in comparison to furnace cooling. Which process creates higher yield stresses and why?

4.40 In copper $G = 48.3$ GPa and b, the Burgers vector, is taken to be 0.25 nm. Find (a) the force required to bend a dislocation into a radius $R = 10$ μm; (b) the energy of this curved dislocation.

4.41 What is the effect of misfit dislocations on film–substrate interfaces? What happens as the thickness of the film increases?

Chapter 5

Imperfections: Interfacial and Volumetric Defects

5.1 Introduction

In Chapter 4, we dealt with point and line defects. There is another class of defects called *interfacial*, or *planar*, defects. These imperfections, as the name signifies, occupy an area or surface and so are two-dimensional, as well as being of great importance. Examples of such defects are free surfaces of a material, grain boundaries, twin boundaries, domain boundaries, and antiphase boundaries. Of all these, grain boundaries are the most important from the point of view of the mechanical properties of the material. In what follows, we consider in detail the structure of grain and twin boundaries and their importance in various deformation processes, and, very briefly, the structure of other interfacial defects. Details regarding the strengthening of a material by grain boundaries are given in Section 5.3. Volumetric defects, such as voids, also play a major role in the mechanical properties of materials, affecting the strength and elastic properties of the material significantly. Volumetric defects are briefly described in Section 5.7. In Section 5.8, we present the defects occurring in polymers.

5.2 Grain Boundaries

Crystalline solids generally consist of a large number of grains separated by boundaries. Most industrial metals and ceramics are polycrystalline aggregates, and the mechanical properties of these polycrystals can be radically different from those of the monocrystals that form the individual grains. Figure 5.1 illustrates a polycrystalline aggregate, in which each grain has a distinct crystallographic orientation. The sizes of these individual grains vary from submicrometer (for nanocrystalline and microcrystalline structures) to millimeters and even centimeters (for materials especially processed for high-temperature creep resistance). Figure 5.2 shows typical equiaxed grain configurations for polycrystalline tantalum and titanium

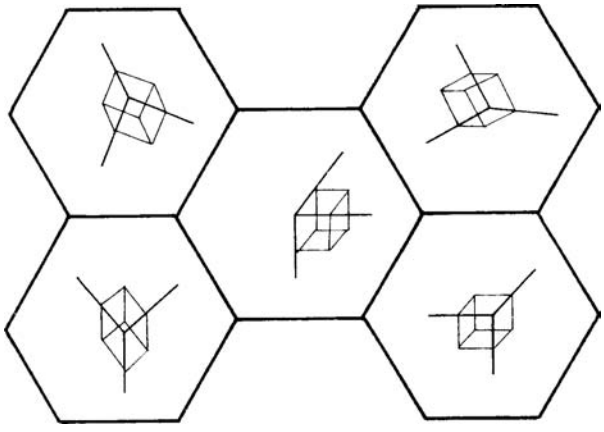

Fig. 5.1 Grains in a metal or ceramic; the cube depicted in each grain indicates the crystallographic orientation of the grain in a schematic fashion.

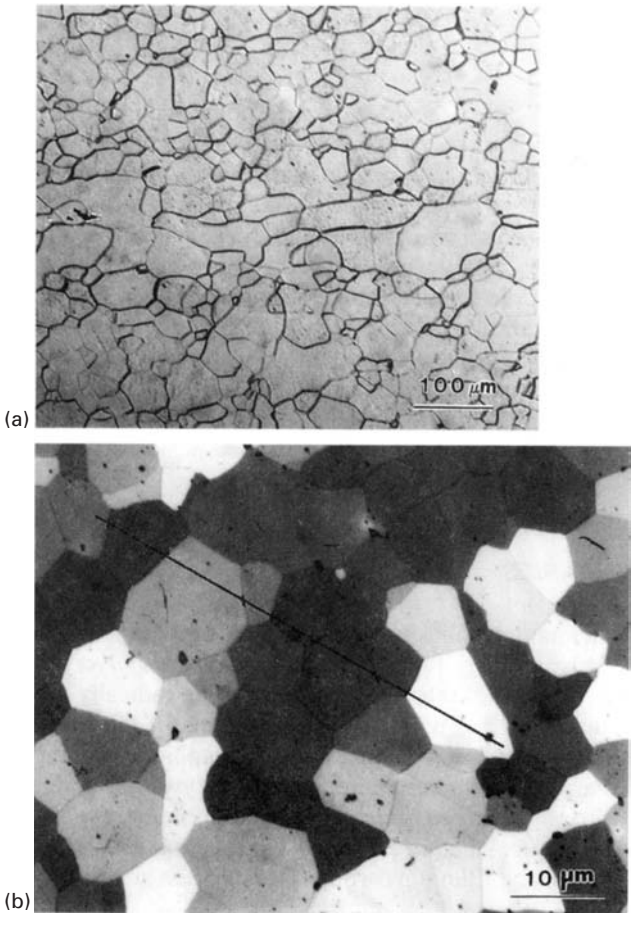

(a)

(b)

Fig. 5.2 Micrographs showing polycrystalline (a) tantalum and (b) TiC.

carbide. Grains often are elongated through plastic deformation. Each grain (or subgrain) is a single crystal, and the grain boundaries are thus transition regions between neighboring crystals. These regions may consist of various kinds of dislocations. When the misorientation between two grains is small, the grain boundary can be described

by a relatively simple configuration of dislocations (e.g., an edge dislocation wall) and is, fittingly, called a *low-angle boundary*. When the misorientation is large (called, again appropriately, a *high-angle boundary*), more complicated structures are involved (as in a configuration of soap bubbles simulating the atomic planes in crystal lattices). A general grain boundary has five degrees of freedom. Three degrees specify the orientation of one grain with respect to the other, and two degrees specify the orientation of the boundary with respect to one of the grains.

Grain structure is usually specified by giving the average diameter or using a procedure attributed to the American Society for Testing and Materials (ASTM) according to which the grain size is specified by the number n in the expression $N = 2^{n-1}$, where N is the number of grains per square inch when the sample is examined at 100 power.

The ASTM procedure is common in engineering applications. In research, it is often preferred to measure the grain size by the lineal intercept technique. In this technique, lines are drawn in the photomicrograph, and the number of grain-boundary intercepts, N_ℓ, along a line is counted. The mean lineal intercept is then

$$\boxed{\bar{\ell} = \frac{L}{N_\ell M},} \tag{5.1}$$

where L is the length of line and M is the magnification in the photomicrograph of the material. In Figure 5.2(b), a line is drawn for purposes of illustration. The length of the line is 6.5 cm. The number of intersections, N_ℓ, is equal to 7, and the magnification (obtained by using the marker of 10 μm) $M = 1{,}300$. Thus,

$$\bar{\ell} = \frac{65 \times 10^{-3}}{7 \times 1300} = 7.1\,\mu\text{m}.$$

Several lines should be drawn to obtain a statistically significant result. The mean lineal intercept $\bar{\ell}$ does not really provide the grain size, but is related to a fundamental size parameter, the grain-boundary area per unit volume, S_v, by the equation

$$\bar{\ell} = \frac{2}{S_v}. \tag{5.2}$$

The proof of this formula is beyond the scope of this book, but is given by deHoff and Rhines.[1] If we assume, to a first approximation, that the grains are spherical, we have the following relationship between the grain-boundary area and volume:

$$\begin{aligned} S_v &= \frac{1}{2}\frac{4\pi r^2}{\frac{4}{3}\pi r^3} \\ &= \frac{3}{2r} = \frac{3}{D}. \end{aligned} \tag{5.3}$$

[1] R. T. deHoff and F. N. Rhines (eds.), *Quantitative Microscopy* (New York: McGraw-Hill, 1968).

Here, D is the average grain diameter, and the factor 1/2 was introduced because each surface is shared between two grains. From Equations 5.2 and 5.3, we get

$$D = \frac{3}{2}\bar{\ell},$$

which is the most correct way to express the grain size from lineal intercept measurements.

Example 5.1

The American Society for Testing and Materials (ASTM) has a simple index, called the ASTM grain size number, n, defined as

$$\boxed{N = 2^{n-1}}$$

where N is the number of grains in an area of 1 in^2 ($=64.5$ mm^2) in a 100-power micrograph. In one such grain size measurement of an aluminum sample, it was found that there were 56 full grains in the area, and 48 grains were cut by the circumference of the circle of area 1 in^2. (a) Calculate ASTM grain size number n for this sample. (b) Calculate the mean lineal intercept.

Solution: The grains cut by the circumference of the circle are taken as one-half the number. Thus,

$$\begin{aligned} N &= 56 + 48/2 \\ &= 56 + 24 = 80 = 2^{n-1} \\ n &= \ln N / \ln 2 + 1 \\ &= \ln 80 / \ln 2 + 1 \\ &= 4.38/0.69 + 1 = 7.35. \end{aligned}$$

(b) For the mean lineal intercept, we use the circle:

$$\begin{aligned} \pi r^2 &= 1in^2, \\ r &= 0.56\,\text{in}, \\ \bar{\ell} &= \frac{2\pi r}{N_\ell M} = \frac{2\pi \times 0.56 \times 25.4}{48 \times 100} \\ &= 0.0186\,\text{mm} = 18.6\,\mu\text{m}. \end{aligned}$$

Example 5.2

Determine the grain size for the microstructure shown in Figure E5.2, using both the lineal intercept method and the ASTM method. The straight marks traversing the grains are annealing twins and should be

counted in the computation. From the mean lineal intercept, obtain the grain diameter.

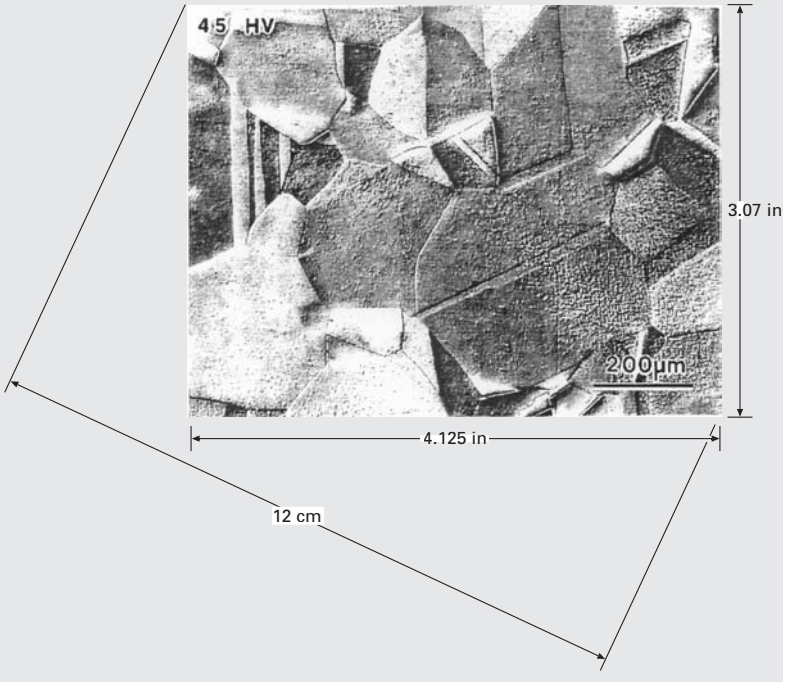

Fig. E5.2

Solution: From the ASTM method, $N = 2^{n-1}$, where N is the number of grains per unit area (in^2) and n is the grain size number.

The number of grains counted is approximately 60, and the area of the picture is $3.07 \times 4.20 = 12.90$ in^2. So we have

$$N = \frac{60}{12.9} = 4.65.$$

We rewrite N as 2^{n-1}, and taking logarithms, we get

$$\ln N = \ln 2^{n-1}$$
$$= (n-1)\ln 2.$$

So we have

$$1.53 = (n-1)\ln 2,$$
$$n - 1 = 2.24,$$
$$n \approx 3.$$

By the lineal intercept method, $\overline{\ell} = L/(MN)$, where $M = 2$ cm/200 μm $= 100$ is the magnification, $L = 12$ cm is the straight line drawn, and

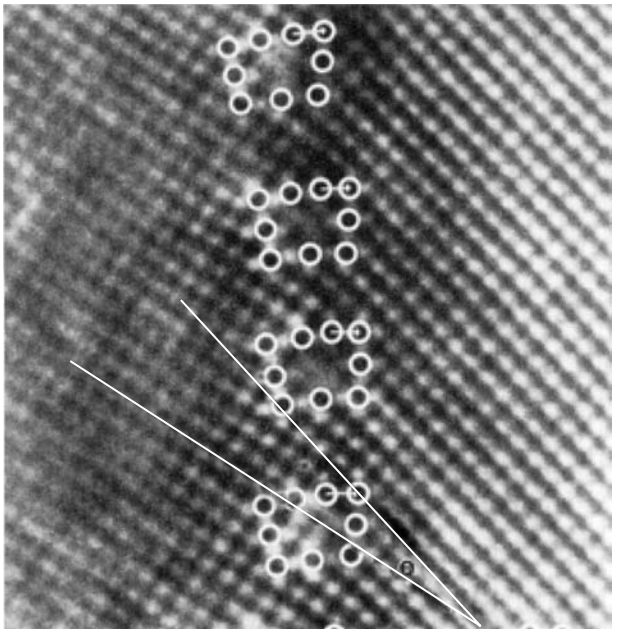

Fig. 5.3 Low-angle grain-boundary observed by high-resolution transmission electron microscopy. Positions of individual dislocations are marked by Burgers circuits. (Courtesy of R. Gronsky.)

$N \approx 9$ is the number of intercepts (with grains). Thus, we have

$$\bar{\ell} = \frac{12}{100 \times 9} = 0.013\text{cm}$$
$$= 130\,\mu\text{m}.$$

5.2.1 Tilt and Twist Boundaries

The simplest grain boundary consists of a configuration of edge dislocations between two grains. The misfit in the orientation of the two grains (one on each side of the boundary) is accommodated by a perturbation of the regular arrangement of atoms in the boundary region. This is very clearly seen in the high-resolution transmission electron micrograph of Figure 5.3. A low-angle grain-boundary with a misorientation $\theta = 10^\circ$ between equivalent (100) planes is shown, and the dislocations are highlighted by circles marking their Burgers vector.

Figure 5.4 shows some vertical atomic planes terminating in a boundary, and each termination is represented by an edge dislocation. The misorientation at the boundary is related to the spacing between dislocations, D, by the relation (see triangle with dimensions)

$$D = \frac{b/2}{\sin(\theta/2)} \cong \frac{B}{\theta} \quad \text{(for very small } \theta\text{)}, \tag{5.4}$$

where b is the Burgers vector.

It is instructive to calculate the spacing between dislocations in Figure 5.3 and to compare it with the measured value from the electron micrograph. We will express all values in terms of the lattice spacing along [100] directions. Let us call this value a, so that

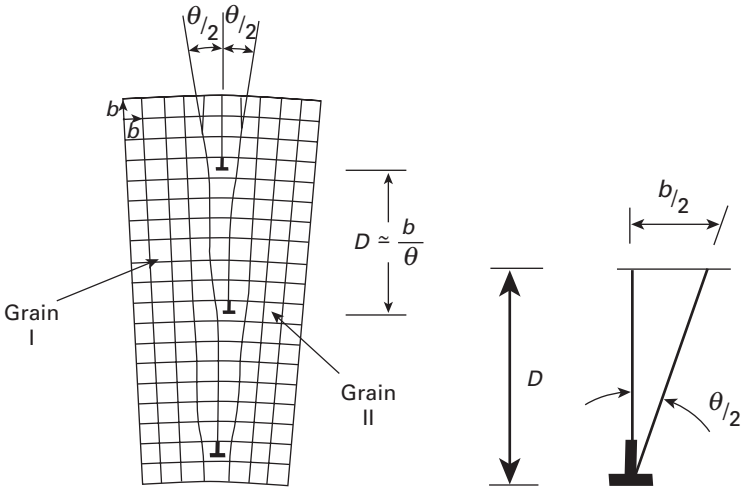

Fig. 5.4 Low-angle tilt boundary.

$$b = 1.3a.$$

The calculated dislocation spacing (from the measured angle $\theta = 10^\circ \approx (1/6 \text{ rad})$ is

$$D = \frac{1.3a}{\theta} \approx 7.8a.$$

The measured dislocation spacing in Figure 5.3 is

$$D = 8a.$$

Thus, the agreement with Equation 5.4 and Figure 5.3 is excellent.

As the misorientation θ increases, the spacing between dislocations is reduced, until, at large angles, the description of the boundary in terms of simple dislocation arrangements does not make sense. Theta becomes so large, that the dislocations are separated by one or two atomic spacings; for such small separations, the dislocation core energy becomes important and the linear elasticity does not hold. In these cases, the grain boundary is a region of severe localized disorder.

Boundaries consisting entirely of edge dislocations are called *tilt boundaries*, because the misorientations, as can be seen in Figure 5.4, can be described in terms of a rotation about an axis normal to the plane of the paper and contained in the plane of dislocations. The example shown in that figure is called a *symmetrical tilt wall*, as the two grains are symmetrically located with respect to the boundary. A boundary consisting entirely of screw dislocations is called a *twist boundary*, because the misorientation can be described by a relative rotation of two grains about an axis. Figure 5.5 shows a twist boundary consisting of two groups of screw dislocations.

It is possible to produce misorientations between grains by combined tilt and twist boundaries. In such a case, the grain boundary structure will consist of a network of edge and screw dislocations.

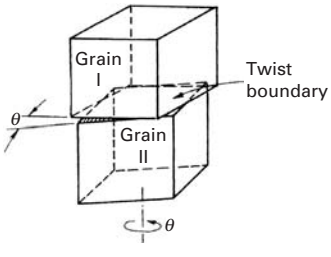

Fig. 5.5 Low-angle twist boundary.

5.2.2 Energy of a Grain Boundary

The dislocation model of a grain boundary can be used to compute the energy of low-angle boundaries ($\theta \leq 10^\circ$). For such boundaries, the distance between dislocations in the boundary is more than a few interatomic spaces. We have

$$\frac{b}{D} \cong \theta \leq 10^\circ \cong \frac{1}{6}\text{rad} \quad \text{or} \quad D \approx 6b,$$

and the energy of the boundary is equal to the total energy of all dislocations per unit length

$$E = E_\perp\left(\frac{1}{D}\right) = E_\perp\left(\frac{\theta}{b}\right) = \frac{\theta}{b}\left[\frac{Gb^2}{4\pi(1-\nu)}\ln\frac{D}{r_0} + E_{\text{core}}\right], \tag{5.5}$$

where $E\perp$ is the strain energy per dislocation in the grain boundary. Thus, the energy of a tilt boundary is given by[2]

$$E = \theta\frac{Gb}{4\pi(1-\nu)}(-\ln\theta + A) = E = E_0\theta(A - \ln\theta), \tag{5.6}$$

where A is a parameter that emerges in the derivation and

$$E_0 = \frac{Gb}{4\pi(1-\nu)}. \tag{5.7}$$

Example 5.3

In a low-angle tilt boundary in an aluminum sample, the misorientation is 5°. Estimate the spacing between dislocations in this boundary, given that $b_{\text{Al}} = 0.29$ nm.

Solution: We have

$$b = 0.29\,\text{nm}, \theta = 5^\circ = 5/57.3 = 0.087\,\text{rad}.$$

The dislocation spacing is

$$D = b/\theta = 0.29\,\text{nm}/0.087 = 3.33\,\text{nm}.$$

Example 5.4

Calculate the energy of a low-angle tilt boundary in nickel as a function of the misorientation θ, for $0 < \theta < 10$. For Ni, $r = 0.125$ nm, $G = 76$ GPa, and $\nu = 0.31$.

Solution: We have

$$E = \frac{Gb}{4\pi(1-\nu)}\theta(A - \ln\theta).$$

[2] M. A. Meyers and K. K. Chawla, *Mechanical Metallurgy* (Englewood Cliffs, Prentice Hall, 1984), pp. 273–275.

We first calculate b; we use $a = 2r\sqrt{2}$, and the magnitude of [100] Burgers vectors is

$$d_{[110]} = \frac{a}{\sqrt{h^2 + k^2 + l^2}} = \frac{a}{\sqrt{2}}.$$

Thus,

$$b = \frac{a}{\sqrt{2}} = 2r = 0.250\,\text{nm}$$

and

$$E = \frac{47 \times 10^9 \times 0.25 \times 10^{-9}}{4\pi(1 - 0.31)}\theta(A - \ln\theta).$$

We can assume that the dislocation energy is equal to the core energy when the separation between them is equal to $10b$. This is twice the core radius used by many scientists. From that value, we obtain the value of the constant of integration, A. The sequence of equations is

$$U = \frac{Gb^2}{10} \quad \text{for} \quad D = 10b = \frac{b}{\theta},$$

$$E = \frac{Gb^2}{10D} = \frac{Gb^2}{100b} = \frac{Gb}{100} \quad (\theta = 0.1),$$

$$\frac{Gb}{100} = \frac{Gb \times 0.1}{4\pi(1 - \nu)}(A - \ln 0.1),$$

$$A = \frac{4\pi(1 - \nu)}{10} + \ln\, 0.1 = 0.866 - 2.30,$$

$$= -1.436.$$

So

$$E = 2.2\theta\,(-1.436 - \ln\theta).$$

Example 5.5

Calculate the dislocation spacing and energy of a low-angle tilt boundary in copper crystal if $\theta = 0.5^\circ$, $G = 48.3$ GPa, $\nu = 0.343$, and $r_{\text{Cu}} = 0.157$ nm.

Solution: The spacing is

$$D = \frac{b}{\theta}.$$

For FCC copper,

$$b = \frac{a}{\sqrt{2}}, \quad 4r_{\text{cu}} = \sqrt{2a},$$

$$b = \frac{(4/\sqrt{2})r_{\text{cu}}}{\sqrt{2}} = 2r_{\text{cu}} = 0.314\,\text{nm},$$

$$\theta = 0.5^\circ = \frac{0.5}{180}\pi = 0.0009\ \text{rad},$$

$$D = \frac{b}{\theta} = \frac{0.314}{0.009} = 34.9\,\text{nm}.$$

We next assume that $D = 10b$, so

$$D = \frac{b}{\theta} = 10b$$
$$\theta = 0.1.$$

We thus have

$$E = E_{\perp}\left(\frac{1}{D}\right) = \frac{Gb^2}{10}\left(\frac{1}{D}\right) = \frac{Gb}{100}, \quad \theta = 0.1.$$

Also,

$$E = \frac{Gb}{4\pi(1-\nu)}\theta(A - \ln\theta).$$

Hence, setting the two equations for E equal to each other, we obtain

$$\frac{Gb}{100} = \frac{Gb}{4\pi(1-\nu)}\theta(A - \ln\theta)$$

and it follows that

$$A = \frac{4\pi(1-\nu)}{100\theta} + \ln\theta$$
$$= \frac{4\pi(1-0.343)}{100 \times 0.1} + \ln 0.1$$
$$= -1.477.$$

Substituting this value of A into the second equation for E yields

$$E = \frac{Gb}{4\pi(1-\nu)}\theta(-1.477 - \ln\theta).$$

Now, given that $G = 48.3$ GPa, $\nu = 0.343$, and $\theta = 0.009$ rad, we obtain

$$E = \frac{48.3 \times 10^9 \times 0.314 \times 10^{-9}}{4\pi(1-0.343)} \times 0.009 \times (-1.477 - \ln 0.009)$$
$$= 0.053 J/m^2.$$

5.2.3 Variation of Grain-Boundary Energy with Misorientation

Consider Equation 5.6. Because of the $(-\ln\theta)$ term, a merger of two low-angle boundaries, forming a high-angle boundary, always results in a net decrease in the total energy of the interface. Thus, low-angle boundaries have a tendency to combine and form boundaries of large misorientation.

A plot of E versus θ gives a curve with a maximum at $\theta_{\max} \approx 0.5$ rad ($\approx 30^\circ$). However, the dislocation model of grain boundaries loses validity at much smaller orientations ($\theta \leq 10^\circ$). Some recent studies, using field-ion microscopy, have shown that the high-angle grain boundaries consist of rather large regions of atomic fit separated by regions of misfit, to which are associated the grain-boundary ledges. The boundary thickness is not more than two to three atomic diameters. Low-angle grain boundaries have a dislocation density that increases proportionally to the misorientation angle (see Equations 5.4 and 5.6), and, consequently, the energy of a low-angle boundary

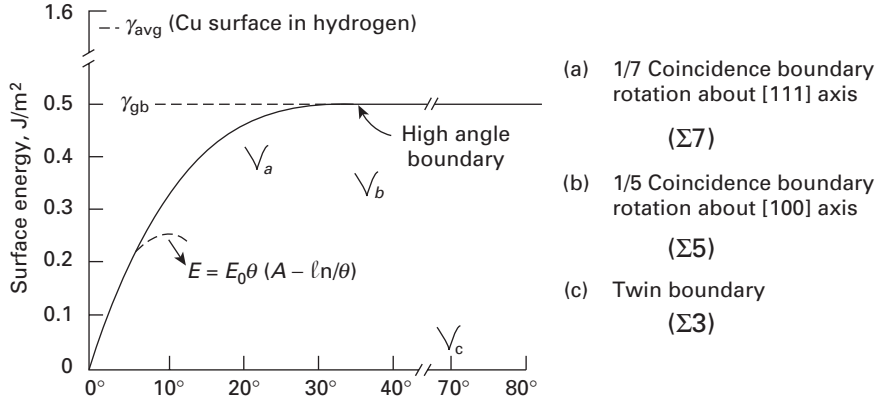

Fig. 5.6 Variation of grain-boundary energy γ_{gb} with misorientation θ. (Adapted with permission from A. G. Guy, *Introduction to Materials Science* (New York: McGraw-Hill, 1972), p. 212.)

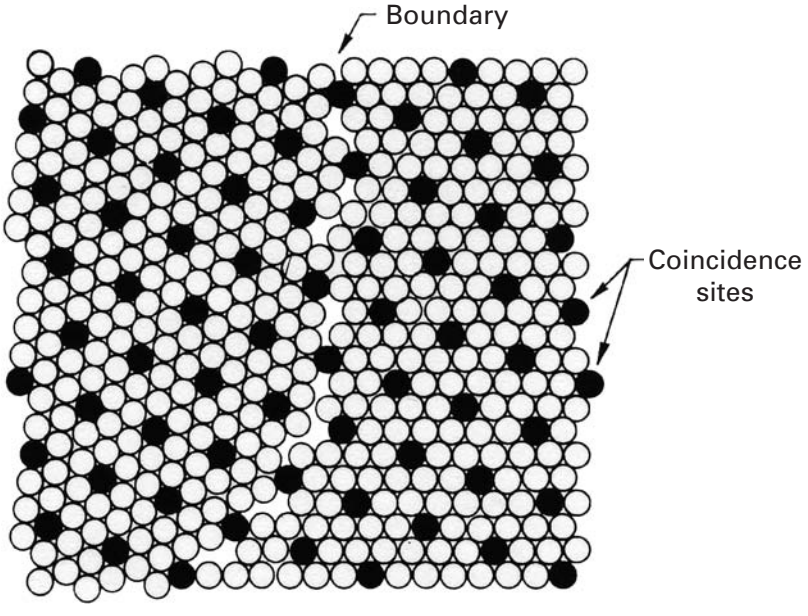

Fig. 5.7 Coincidence lattice made by every seventh atom in the two grains, misoriented 22° by a rotation around the <111> axis. (Adapted from M. L. Kronberg and H. F. Wilson, *Trans. AIME*, 85 (1949), 501.)

increases linearly with θ near 0°. After this, the energy increases slowly as the stress fields of adjacent dislocations interact more strongly. This behavior is shown in Figure 5.6. A surface tension, γ_{gb}, can be associated with an ordinary (high-angle) grain boundary, which consists of a mixture of various types of dislocations. Because the value of γ_{gb} is relatively high, it is instructive to determine the stable forms assumed by the grains of a given material. As it happens, there are certain special boundaries for which a particular high angle between two adjacent crystals produces a low value of γ. These special boundaries can be divided into two categories: coincidence boundaries and coherent twin boundaries. A coincidence boundary (Figure 5.7) is incoherent, as is an ordinary grain boundary; that is, a majority of the atoms of one crystal in the boundary do not correspond to the lattice sites of the other crystal. On an average, however, this noncorrespondence in a coincidence boundary is less as the density of coincidence sites increases. For example, in the figure, one

Table 5.1 Some Coincidence Site Boundaries in FCC Crystals[a]

Rotation Axis	Rotation Angle (deg)	Density of Coincidence Sites
(111)	38	1 in 7
	22	1 in 7
	32	1 in 13
	47	1 in 19
(110)	39	1 in 9
	50.5	1 in 11
	26.5	1 in 19
(100)	37	1 in 15

[a] Reprinted with permission from J. W. Christian, *The Theory of Transformation in Metals and Alloys* (Elmsford, NY: Pergamon Press, 1965), p. 326.

atom in seven in the boundary is in a lattice position for both the crystals. We call this boundary a *one-seventh coincidence boundary*, and the atomic sites (the black atoms in the figure) in question form a coincidence lattice for the two grains. Coincidence lattices occur in all common crystalline structures and have a density of sites varying from $\frac{1}{3}$ to $\frac{1}{9}$ and less.

A twin boundary is frequently a kind of coincidence boundary, but it is convenient to treat it separately. The energy of a twin boundary, γ_{twin}, is generally about 0.1 γ_{gb} (see Figure 5.6), whereas the energy of a coincidence boundary is only slightly less than γ_{gb}. The two most common twin orientations are (1) rotation twins (coincidence), produced by a rotation about a direction [*hkl*] called the twinning axis, and (2) reflection twins, in which the two lattices maintain a mirror symmetry with respect to a plane [*hkl*] called the twinning plane.

Some of the orientations that give the highest density of coincidence lattice sites in crystals are shown in Table 5.1. These boundaries have lower energies than those of random high-angle boundaries. Contrary to the great majority of low-energy boundaries, coincidence site boundaries have greater mobility than that of random boundaries. Twin boundaries, even with low energies, have lower mobility because they are coherent.

The interfaces between different phases (interphase interfaces) are more complex, since the accommodation of the atoms has to be more drastic. Nevertheless, strong interfaces can be formed, even between different ceramic phases. An illustration of this is provided in Figure 5.8, which shows the interface between alumina (hexagonal) and the spinel structure ($NiAl_2O_4$). In ceramics, the requirement of electrical charges puts additional restrictions on the boundaries. Nevertheless, the boundary shown in Figure 5.8(a) and the atomic positions clearly marked in Figure 5.8(b) are of high coherence.

5.2.4 Coincidence Site Lattice (CSL) Boundaries

It is instructive to consider some other important aspects of coincidence site lattice (CSL) boundaries. As described earlier, we get a CSL

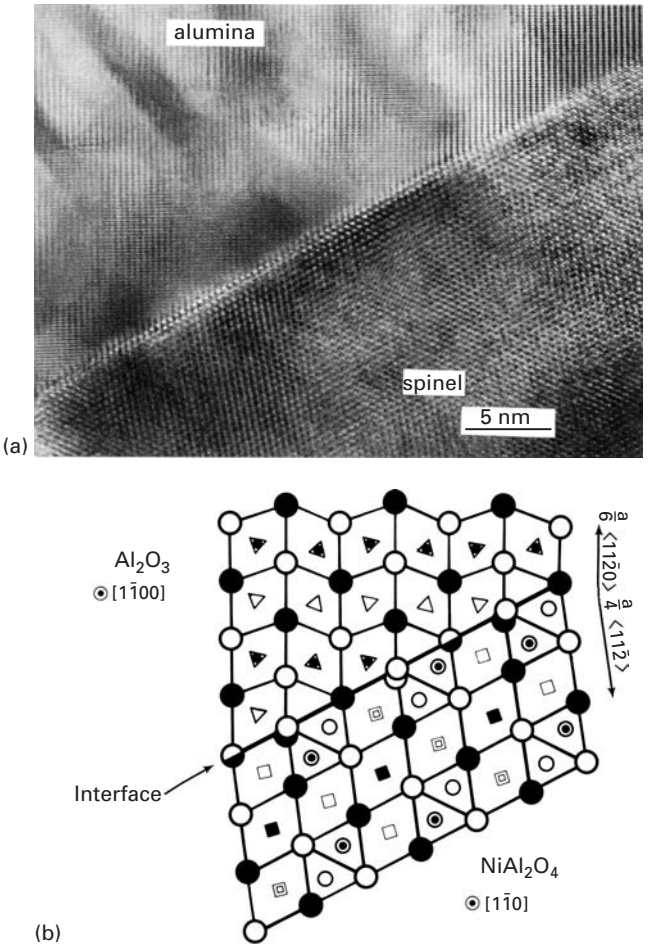

Fig. 5.8 Interface between alumina and $NiAl_2O_4$ (spinel). (a) High-resolution TEM. (b) Representation of individual atomic positions. (Courtesy of C. B. Carter.)

boundary when a certain rotation of one grain relative to another grain results in a three-dimensional atomic pattern in which a certain fraction of lattice points coincide in the two grains. The volume of the CSL primitive cell is a small multiple of the volume of the lattice primitive cell. Such a CSL boundary is characterized by a parameter Σ, the reciprocal of the fraction of lattice sites that coincide (in Table 5.1, $\Sigma = 7, 9, 13, 15, 19$). Equivalently, Σ is the ratio of the volume of the CSL primitive cell to that of the lattice primitive cell. A coherent twin boundary is $\Sigma 3$. It has been observed that CSL grain boundaries with relatively low values of Σ can have a significant influence on the mechanical behavior of a polycrystalline material. CSL boundaries with small values of Σ result in short-period ordered structures in the grain boundary. CSL boundaries with Σ less than 29 show the following advantages over random grain boundaries or boundaries with higher Σ values:

- lower grain boundary energy in pure metals
- lower diffusivity
- lower electrical resistivity
- lower susceptibility to solute segregation

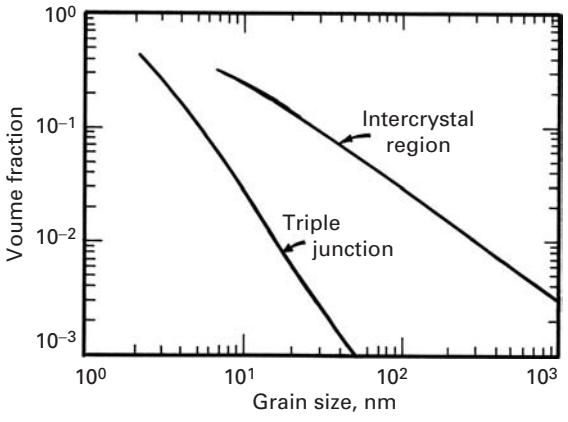

Fig. 5.9 The effect of grain size on calculated volume fractions of intercrystal regions and triple junctions, assuming a grain boundary thickness of 1 nm. (Adapted from B. Palumbo, S. J. Thorpe, and K. T. Aust, *Scripta Met.*, 24 (1990) 1347.)

- greater resistance to grain boundary sliding, fracture, and cavitation
- greater resistance to initiation of localized corrosion
- greater boundary mobility with specific solutes in a specific concentration range.

It would thus appear that control of the character and density of low-Σ boundaries can be a means of producing a superior polycrystalline material.

5.2.5 Grain-Boundary Triple Junctions

Grain-boundary triple junctions are sites where four grains or three grain boundaries meet. Such boundaries are commonly observed in crystalline materials. The number of triple junctions can have a great influence on the mechanical properties of the material. The number of triple junctions in a polycrystalline material will depend on the grain size and crystal geometry of the material. Palumbo *et al.*[3] considered a three-dimensional distribution of tetrakaidecahedral grains and obtained the volume fractions of intercrystalline region (grain-boundary) and triple-boundary junctions. Figure 5.9 shows the effect of grain size on calculated volume fractions of these entities. Note the highly pronounced effect for grain sizes less than 20 nm, i.e., in the nanometer range.

5.2.6 Grain-Boundary Dislocations and Ledges

Various experimental observations of the structure of grain boundaries have demonstrated the existence of grain-boundary dislocations (GBDs) when the orientation relations deviate from the ideal coincidence lattice site orientations. A grain-boundary dislocation belongs to the grain boundary and is not a common lattice dislocation.

Grain-boundary dislocations can acquire the geometry of a grain-boundary ledge by grouping together. This agglomeration, which leads to the formation of a step, is shown in Figure 5.10. Figure 5.10(a)

[3] B. Palumbo, S. J. Thorpe, and K. T. Aust, *Scripta Met.*, 24 (1990) 1347.

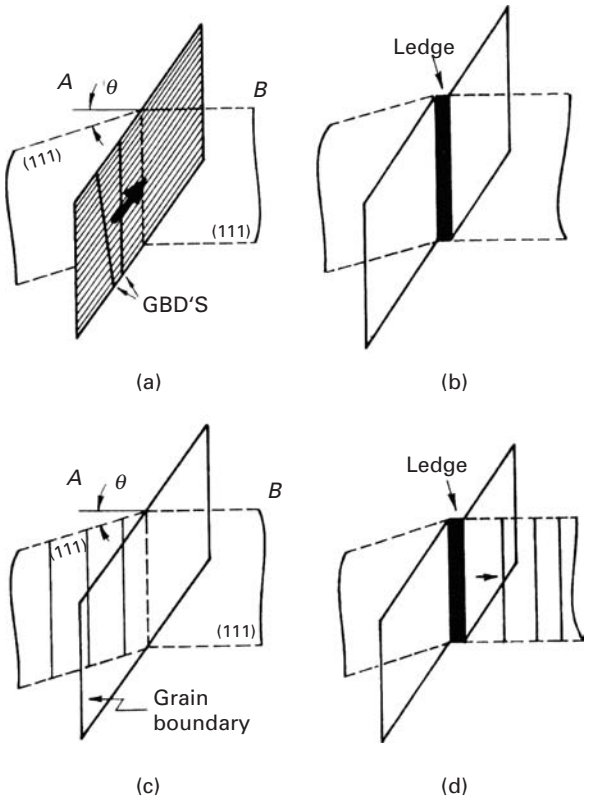

Fig. 5.10 Models of ledge formation in a grain boundary. (Reprinted with permission from L. E. Murr, *Interfacial Phenomena in Metals and Alloys* (Reading, MA: Addison Wesley, 1975), p. 255.)

shows the movement of GBDs along the grain-boundary plane in the direction indicated by the arrow. Figure 5.10(b) shows the coalescence of GBDs to make a grain-boundary ledge. Another way of ledge formation is shown in Figures 5.10(c) and (d). Under the applied tension, lattice dislocations can move from grain *A* through the boundary plane to grain *B* (Figure 5.10(c)). The passage through the boundary results in heterogeneous shear of the boundary, forming a ledge.

The distinction between a ledge and an intrinsic GBD is one of height; the smallest ledge corresponds to a GBD. Detailed analyses showing how slip can transfer from one grain to another via the formation of intrinsic GBDs have been carried out. Figure 5.11 shows a TEM that reveals ledges and GBDs. The larger steps can be considered ledges, whereas the lines could be GBDs.

In the simplified situation shown in Figure 5.10, the (111) planes of the neighboring grains intersect along the boundaries. Ledges in the grain boundaries constitute an important structural characteristic of the high-angle boundaries. It has been observed that the density of ledges increases with an increase in the boundary misorientation. One of the important aspects of this structure of boundaries is that the ledges can function as effective sources of dislocations, a fact that has important implications for the mechanical properties of polycrystals.

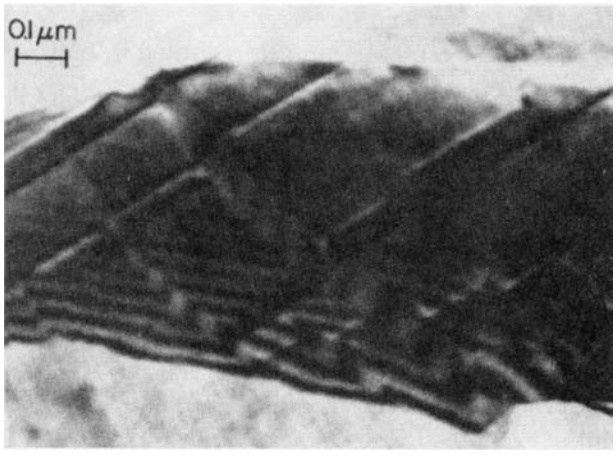

Fig. 5.11 Grain boundary ledges observed by TEM. (Courtesy of L. E. Murr.)

5.2.7 Grain Boundaries as a Packing of Polyhedral Units

The grain-boundary structure can also be described in terms of a packing of polyhedral units. If equal spheres are packed to form a shell such that all spheres touch their neighbors, then the centers of the spheres are at the vertices of a "deltahedron," a polyhedron with equilateral triangles as faces. Ashby *et al.*[4] regard a crystal as a regular packing of polyhedral holes. The FCC structure, for example, consists of a regular packing of tetrahedra and octahedra. The main advantage of such a description of the structure is that it remains valid even when the structure becomes completely disordered (i.e., amorphous). Any grain boundary between metallic crystals can be described in terms of this scheme as a packing of eight basic deltahedra. Ashby *et al.*'s model is able to describe a number of properties associated with grain boundaries — for example, the segregation of certain elements to the boundaries, the characteristically high diffusion rates in the boundaries, and grain-boundary faceting in the presence of impurities. Figure 5.12(a) shows an image-enhanced transmission electron micrograph of a symmetric tilt boundary in gold. The angle θ between the [110] directions in the two grains is approximately 32°. The boundary can be represented (as shown in Figure 5.12(b)) as an array of polyhedra. The figure represents the atomic positions along two planes ("+" and "•") of the TEM of Figure 5.12(a).

5.3 Twinning and Twin Boundaries

There are two types of twin boundaries: deformation twins and annealing twins. A brief description of deformation twins follows.

[4] M. F. Ashby, F. Spaepen, and S. Williams, *Acta Met.*, 26 (1978) 1053.

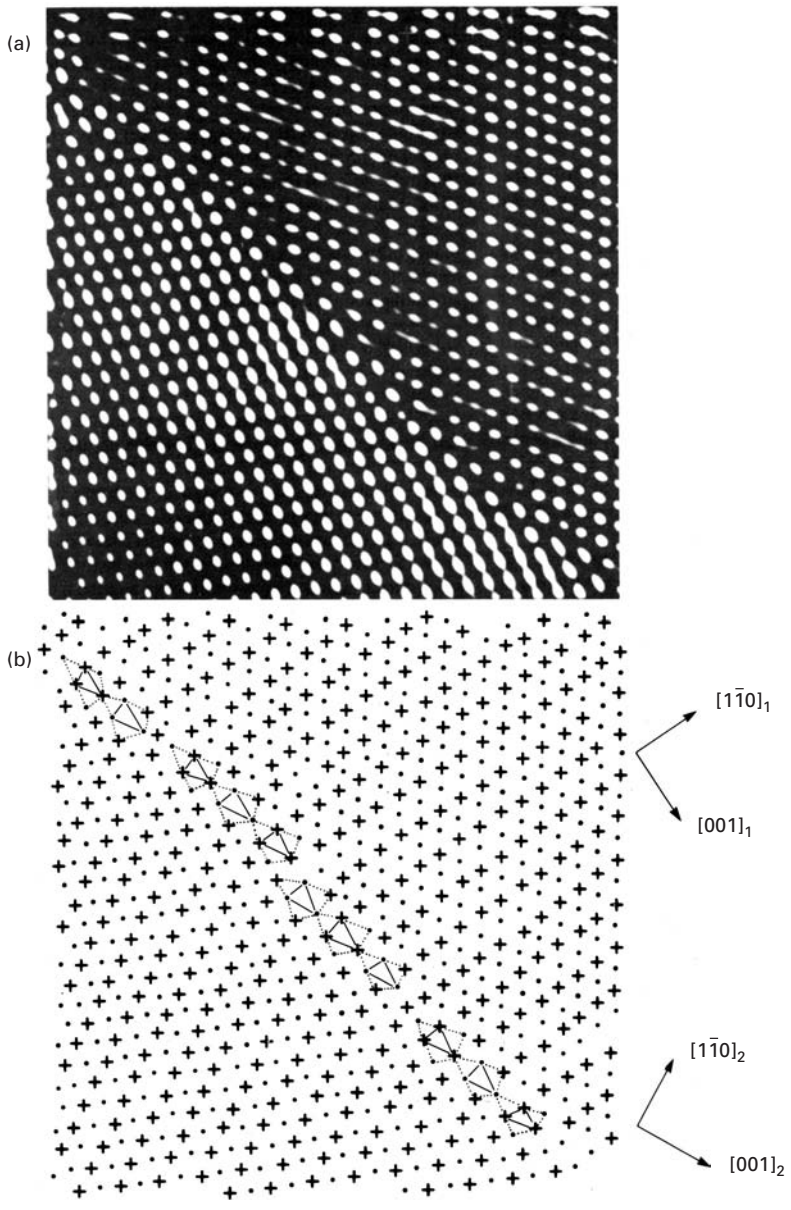

Fig. 5.12 Image and atomic position model of an approximately 32° [110] tilt boundary in gold; note the arrangement of polygons, which represents the boundary. (From W. Krakow and D. A. Smith, *J. Mater. Res.* 22 (1986) 54.)

5.3.1 Crystallography and Morphology

Deformation or mechanical twinning is the second most important mechanism of plastic deformation after slip, although it is not nearly as common as slip. The crystallographic nature of deformation twins is shown in Figure 5.13. When a crystal deforms plastically by twinning, atomic displacements occur, as shown in the figure, which give rise to crystal bands within the grain that are twin oriented. Hexagonal metals, such as Zn and Mg, behave in this way when they are deformed at ambient temperatures, while BCC metals, such as

Table 5.2 Twinning Planes, Directions, and Shears

Structure	Twin Plane and Direction		Shear Strain, γ
FCC	$(111)[11\bar{2}]$		0.707
BCC	$(11\bar{2})[111]$		0.707
HCP	$(10\bar{1}2)\ [10\bar{1}\bar{1}]$	Cd:	0.171
		Zn:	0.139
		Mg:	0.129
		Ti:	0.139
		Be:	0.199

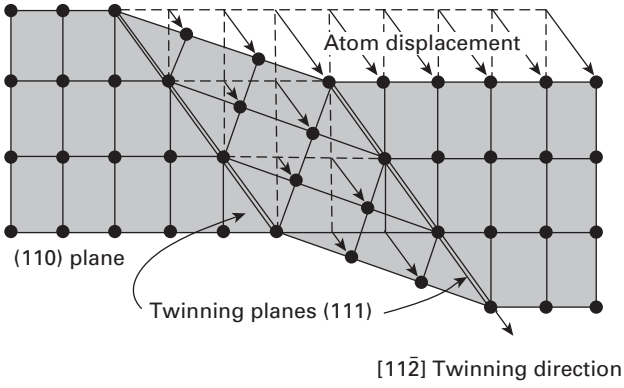

Fig. 5.13 Schematic of twinning in FCC metals.

iron, show this behavior when they are deformed at subambient temperatures. This mechanism is not of great importance in the deformation of FCC metals. The twin planes, twin vectors, and the shear produced by them are given in Table 5.2 for FCC, BCC, and HCP crystals.

Figures 5.14(a) and (b) show deformation twins in Fe–Si and tungsten, respectively. It is clear that twins are crystallographically oriented along specific planes. Figure 5.14(b) shows several grains, as well as the twins that extend, at most, from grain boundary to grain boundary. A few of them are marked by arrows and number 2. They cannot propagate through grain boundaries because of the crystallographic requirements. The sagacious reader will note that there is a mixture of microcracks and deformation twins in the figure, but this issue will not be discussed.

Figure 5.15 illustrates the formation of deformation twins in ceramics. A grain of silicon nitride subjected to compressive loading is imaged in Figure 5.15(a). The diffraction pattern (the spots in Figure 5.15(c)) reveals more than one crystallographic orientation. It is possible, by focusing on only one family of reflections, to image one family of twins. This is shown in Figure 5.15(b). All the bright twins in this dark-field image have the same orientation.

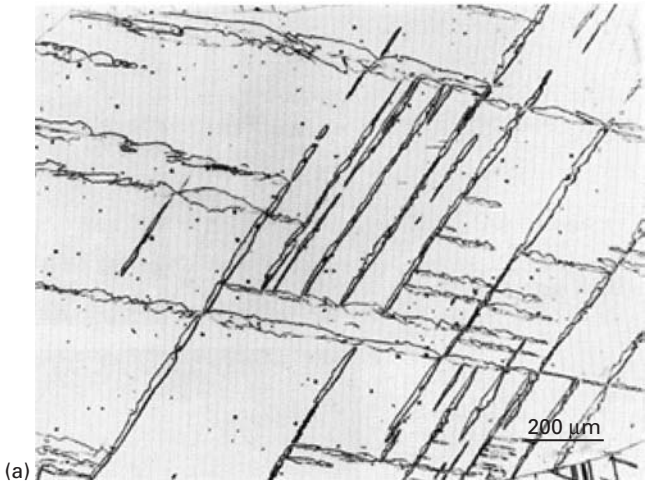

(a)

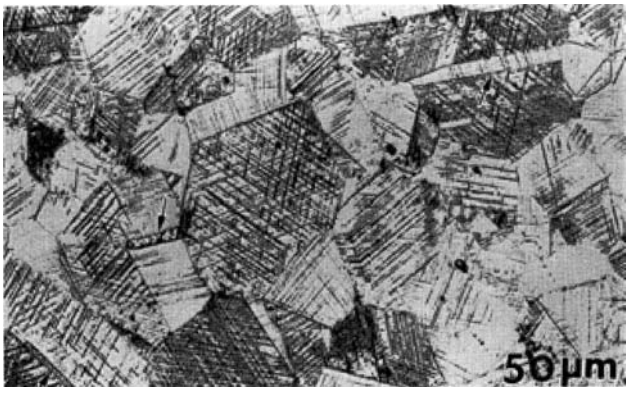

(b)

Fig. 5.14 Deformation twins in (a) iron–silicon (courtesy of O. Vöhringer) and (b) tungsten.

The mechanism of plastic deformation by twinning is very different from that of slip. First, the twinned region of a grain is a mirror image of the original lattice, while the slipped region has the same orientation as that of the original, unslipped grain. Second, slip consists of a shear displacement of an entire block of crystal, while twinning consists of uniform shear strain. Third, the slip direction can be positive or negative (i.e., in tension or compression), while the twinning direction is always polar. Twinning results in a change of shape of a definite type and magnitude, as determined by the crystallographic nature of the twinning elements.

The stress necessary to form twins is, generally, greater, but less sensitive to temperature, than that necessary for slip. This stress required to initiate twinning is much larger than the stress necessary for its propagation. Deformation twinning occurs when the

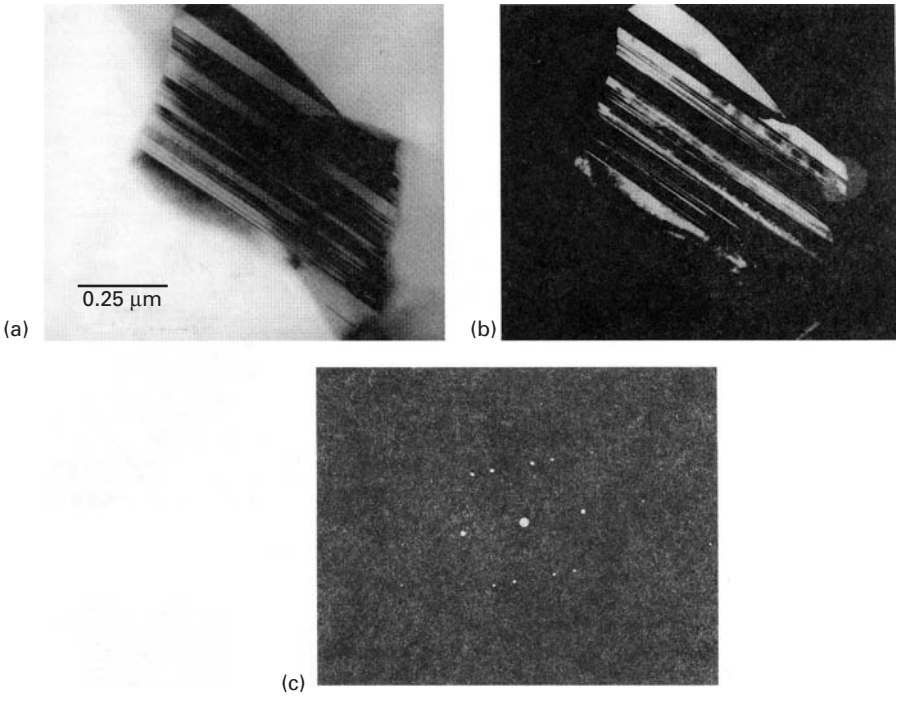

Fig. 5.15 Deformation twins in silicon nitride observed by TEM. (a) Bright field. (b) Dark field. (c) Electron diffraction pattern showing spots from two twin variants, *A* and *B*. (Courtesy of K. S. Vecchio.)

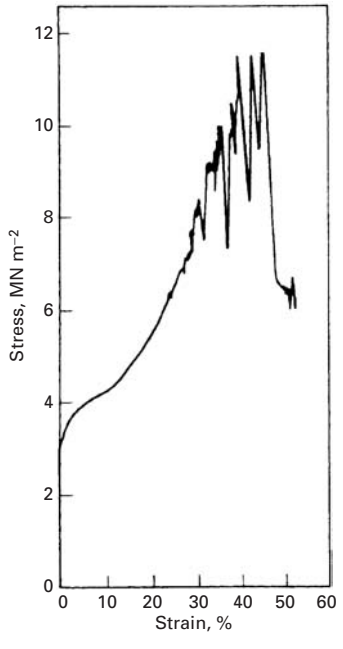

Fig. 5.16 Serrated stress–strain curve due to twinning in a Cd single crystal. (Adapted with permission from W. Boas and E. Schmid, *Z. Phys.*, 54 (1929) 16.)

applied stress is high due to work-hardening, low temperatures, or, in the case of HCP metals, when the resolved shear stress on the basal plane is low. Copper and other FCC metals can be made to deform by twinning at very low temperatures or at very high strain rates. Deformation twins, however, play an important role in the straining of HCP metals. The "cry" heard when a polycrystalline sample of tin is bent plastically is caused by the sudden formation of deformation twins. The bursting of twins during straining can lead to a serrated form of stress–strain curve (Figure 5.16). In many HCP metals, the slip is restricted to basal planes. Thus, twinning can contribute to plastic deformation by the shear that it produces, but this is generally small. (See Table 5.2.) More importantly, the twinning process serves to reorient the crystal lattice to favor further basal slip. In HCP metals, the common twinning elements are the $(10\bar{1}2)$ plane and $[10\bar{1}\bar{1}]$ direction (see Figure 5.17). Twinning results in a compression or elongation along the *c*-axis, depending on the ratio c/a. For $c/a > \sqrt{3}$ (the case of Zn and Cd), twinning occurs on $(10\bar{1}\bar{2})$ $[10\bar{1}\bar{1}]$ when the metal is compressed along the *c*-axis. When $c/a > \sqrt{3}$, the twinning shear is zero. For $c/a < \sqrt{3}$ (the case of Mg and Be), twinning occurs under tension along the *c*-axis. Figure 5.17 shows this dependence on the ratio c/a.

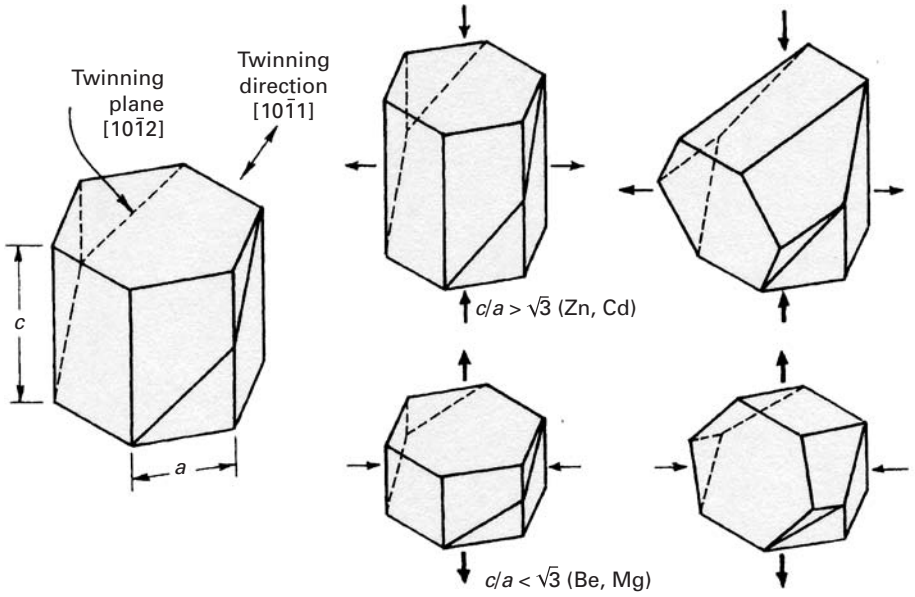

Fig. 5.17 Twinning in HCP metals with c/a ratio more or less than $\sqrt{3}$.

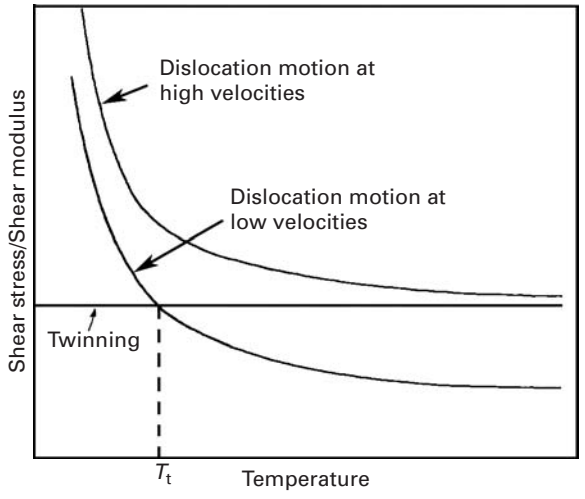

Fig. 5.18 Effect of temperature on the stress required for twinning and slip (at low and high strain rates). (Courtesy of G. Thomas.)

5.3.2 Mechanical Effects

One may regard slip and twinning as competing mechanisms; experimentally, it has been found that either an increase in strain rate or a decrease in temperature tends to favor twinning over slip. In this context, the graphical scheme proposed by G. Thomas and presented in Figure 5.18 is helpful. The low temperature dependence of the stress required to initiate twinning is a strong indication that it is not a thermally activated mechanism. Hence, τ/G for twinning is not temperature dependent. On the other hand, the thermally activated dislocation motion becomes very difficult at low temperatures; T_t is

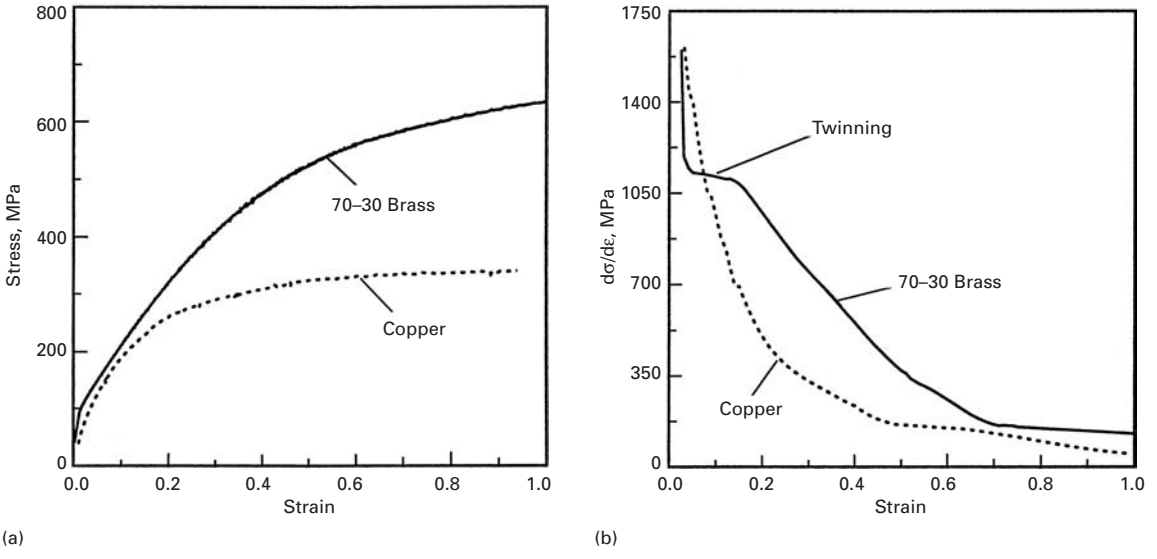

Fig. 5.19 (a) Stress–strain curves for copper (which deforms by slip) and 70% Cu–30% Zn brass (which deforms by slip and twinning). (b) Work-hardening slope $d\sigma/d\varepsilon$ as a function of plastic strain; a plateau occurs for brass at the onset of twinning. (After S. Asgari, E. El-Danaf, S. R. Kalidindi, and R. D. Doherty, *Met. and Mater. Trans.*, 28A (1997) 1781.)

the temperature below which the material will yield by twinning in conventional deformation. However, at high strain rates, dislocation generation and dynamics are such that the whole curve is translated upward, while the twinning curve is stationary, for reasons that will be given later. As a consequence, the intersection of the two curves takes place at a higher temperature.

As the stacking-fault energy of an alloy is decreased, the propensity for twinning increases. The addition of zinc to copper decreases the stacking-fault energy dramatically, from 78 mJ/m^2 (for pure Cu) to 7 mJ/m^2 (for 75–25 brass). This leads to a much greater planarity of slip, which eventually results in twinning. Twinning generates internal barriers to slip and breaks down a material's microstructure into progressively smaller domains. The result is an increase in work-hardening; that is, the movement of dislocations is hampered. Figure 5.19(a) illustrates this effect. The work-hardening rate of copper decreases with plastic strain, in the expected fashion, while brass, in which twinning is prevalent, shows an almost constant work-hardening, over a significant plastic strain range. The onset of twinning is clearly seen in the plateau of the work-hardening rate, in Fig 5.19(b).

As shown in Figure 5.18, the twinning stress seems to be quite insensitive to the temperature. Figure 5.20 shows the twinning stress for a number of metals. The stress required for slip, on the other hand, is quite sensitive to temperature; see Figure 5.18.

Mechanical twinning is, in FCC metals, quite sensitive to the stacking-fault energy. The stress required for twinning increases as the stacking-fault energy is increased. Figure 5.21 shows the twinning stress for a number of copper alloys. The following relationship is obeyed between the twinning stress, σ_T, and the staking-fault energy, γ_{SF}:

$$\sigma_T = K\left(\frac{\gamma_{SF}}{Gb}\right)^{1/2},$$

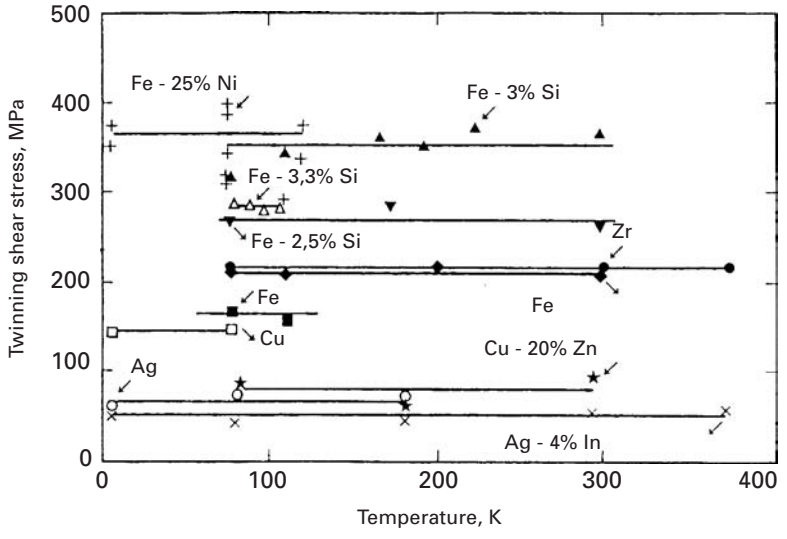

Fig. 5.20 Effect of temperature on twinning stress for a number of metals. (From M. A. Meyers, O. Voehringer, and V. A. Lubarda, *Acta Mater.*, 49 (2001) 4025.)

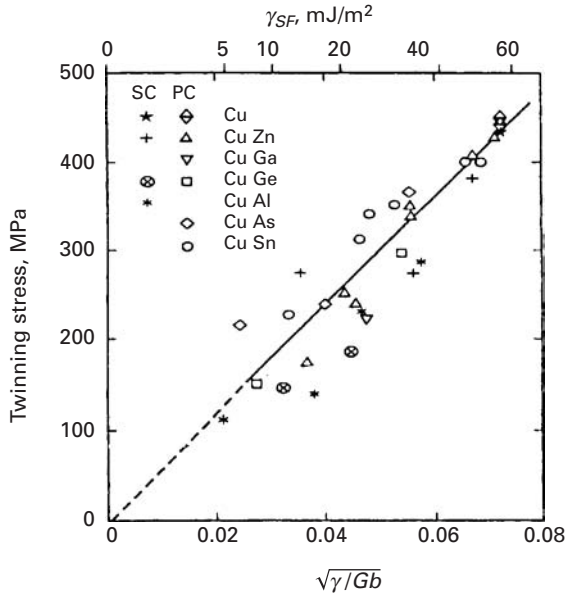

Fig. 5.21 Effect of stacking-fault energy on the twinning stress for several copper alloys. (From M. A. Meyers, O. Voehringer, and V. A. Lubarda, *Acta Mater.*, 49 (2001) 4025.)

where G is the shear modulus, b is the Burgers vector, and K is a constant.

By setting the twinning stress equal to the slip stress, one can obtain the domains in which twinning and slip are prevalent as a function of grain size, stacking-fault energy, etc. For the strain rate, temperature, and grain size dependence of the slip stress, we use constitutive equations such as the Johnson–Cook equation (Section 3.2). One sets the slip stress, σ_S, equal to the twinning stress:

$$\sigma_T = \sigma_S.$$

The application of this equation for titanium with different grain sizes provides the plot shown in Figure 5.22(a). The lines in the

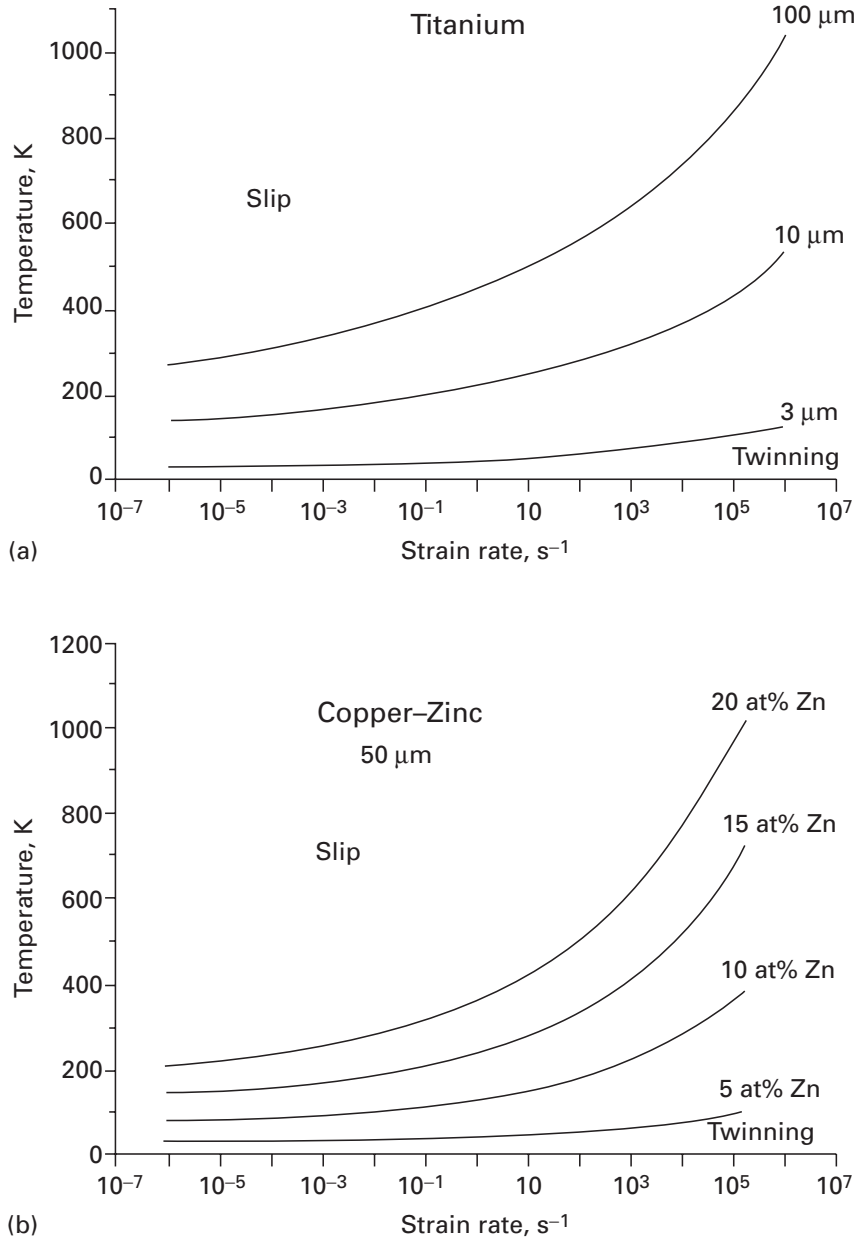

Fig. 5.22 Temperature–strain rate plots with slip and twinning domains; (a) effect of grain size in titanium; (b) effect of stacking-fault energy in copper–zinc alloys. (From M. A. Meyers, O. Voehringer, and V. A. Lubarda, *Acta Mater.*, 49 (2001) 4025.)

plot separate the twinning and slip domains. As the strain rate is increased, the maximum temperature for twinning is increased. The same plot shows the effect of grain size (different lines). As the grain size is decreased, the twinning domain decreases. Figure 5.22(b) shows the effect of stacking-fault energy on the domains. This is done for a monocrystalline copper–zinc alloy. The stacking-fault energy decreases with increasing zinc content. Whereas the Cu–20 at% Zn alloy twins at ambient temperature and low strain rate, it is necessary to apply a very high strain rate at a low temperature to trigger twinning in a Cu–5 at% Zn alloy.

5.4 Grain Boundaries in Plastic Deformation (Grain-Size Strengthening)

Grain boundaries have a very important role in the plastic deformation of polycrystalline materials. The following are among the more important aspects of this role.

1. At low temperatures ($T <$, $0.5T_m$, where T_m is the melting point in K), the grain boundaries act as strong obstacles to dislocation motion. Mobile dislocations can pile up against the boundaries and thus give rise to stress concentrations that can be relaxed by initiating locally multiple slip.
2. There exists a condition of compatibility among the neighboring grains during the deformation of polycrystals that is, if the development of voids or cracks is not permitted, the deformation in each grain must be accommodated by its neighbors.[5] This accommodation is realized by multiple slip in the vicinity of the boundaries, which leads to a high strain-hardening rate. It can be shown, following von Mises, that for each grain to stay in contiguity with others during deformation, at least five independent slip systems must be operating. (See Section 6.2.5.) This condition of strain compatibility leads a polycrystalline sample to have multiple slip in the vicinity of grain boundaries. The smaller the grain size, the larger will be the total boundary surface area per unit volume. In other words, for a given deformation in the beginning of the stress–strain curve, the total volume occupied by the work-hardened material increases with decreasing grain size. This implies a greater hardening due to dislocation interactions induced by multiple slip.
3. At high temperatures, the grain boundaries function as sites of weakness. Grain boundary sliding may occur, leading to plastic flow or opening up voids along the boundaries. (See Chapter 13.)
4. Grain boundaries can act as sources and sinks for vacancies at high temperatures, leading to diffusion currents, as, for example, in the Nabarro–Herring creep mechanism. (See Chapter 13.)
5. In polycrystalline materials, the individual grains usually have a random orientation with respect to one another. Frequently, however, the grains of a material may be preferentially oriented. For example, an Fe–3% Si solid–solution alloy, used for electrical transformer sheets because of its excellent magnetic properties, has grains with their {110} planes nearly parallel and their <100> direction along the rolling direction of the sheet. This material is said to have a *texture* or *preferred orientation*. A preferred orientation of grains is also frequently observed in drawn wires.

[5] J. P. Hirth, *Met. Trans.* 3 (1972) 3047.

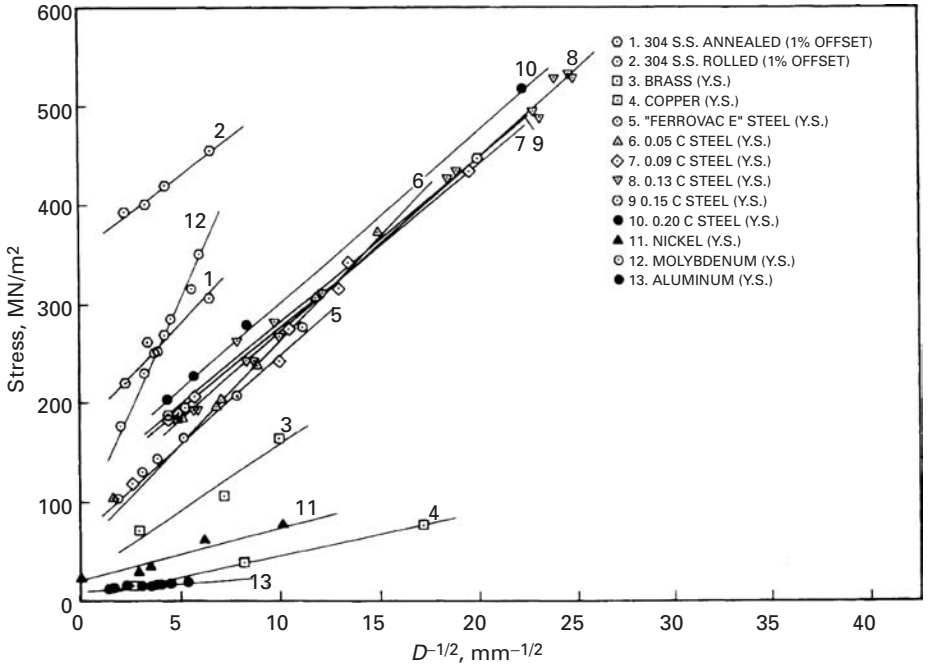

Fig. 5.23 Hall–Petch plot for a number of metals and alloys. Y. S. indicates yield strength.

Ever since Hall and Petch[6] introduced their well-known relationship between the lower yield point of low-carbon steels and grain size, a great deal of effort has been devoted to explaining that relationship from a fundamental point of view and applying it to the yield and flow stress of different metals and alloy systems. The Hall–Petch (H–P) equation has the form

$$\sigma_y = \sigma_0 + kD^{-1/2}, \tag{5.8}$$

where σ_y is the yield stress, σ_0 is a frictional stress required to move dislocations, k is the H–P slope, and D is the grain size. This equation has been applied to many systems, with varying degrees of success. It seems to be a satisfactory description of the dependence of yield stress on grain size when a somewhat limited range of grain sizes is being investigated. Figure 5.23 illustrates the Hall–Petch equation for several metals. BCC and FCC metals exhibiting smooth elastic–plastic transitions and yield points are represented. Table 5.3 presents the parameters for a number of metals.

Figure 5.24 shows the yield strength of iron over a much wider range than that presented in Figure 5.23. The plot is of the Hall–Petch line (full line) and the upper bound (theoretical strength, assumed to be $E/30$), as well as the lower bound (single crystal). Substantial deviations from a single Hall–Petch curve that has approximately the slope for ferrovac E steel and 0.05C steel are observed. The very broad range of grain sizes is the reason for the deviation. Thus, the Hall–Petch

[6] E. O. Hall, *Proc. Roy. Soc.* (*London*) B64 (1951) 474; N. J. Petch, *J. Iron Steel Inst.* 174 (1953) 25.

Table 5.3 Tabulation of σ_0 and k Values for BCC, FCC, and HCP Structures[a]

Material Specification[b]	σ_0 (MPa)	k ($MN/m^{3/2}$)
Body-Centered Cubic		
Mild steel, y.p.	70.60	0.74
Mild steel, $\varepsilon = 0.10$	294.18	0.39
Swedish iron, y.p.	47.07	0.71
Swedish iron, no y.p.	36.28	0.20
Fe–3% Si, y.p., –196 °C	505.99	1.54
Fe–3% Si, twinning, –196 °C	284.37	3.32
Fe–18% Ni, $\varepsilon = 0.002$	650.14	0.22
Fe–18% Ni, twinning, –196 °C	843.32	1.30
FeCo, ordered, $\varepsilon = 0.004$	50.01	0.90
FeCo, disordered, $\varepsilon = 0.004$	319.68	0.33
Chromium, y.p.	178.47	0.90
Chromium, twinning, –196 °C	592.52	4.37
Molybdenum, y.p.	107.87	1.77
Molybdenum, $\varepsilon = 0.10$	392.24	0.53
Tungsten, y.p.	640.33	0.79
Vanadium, y.p.	318.70	0.30
Niobium, y.p.	68.64	0.04
Tantalum, with O_2, y.p. 0 °C	186.31	0.64
Face-Centered Cubic		
Copper, $\varepsilon = 0.005$	25.50	0.11
Cu–3.2% Sn, y.p.	111.79	0.19
Cu–30% Zn, y.p.	45.11	0.31
Aluminum, $\varepsilon = 0.005$	15.69	0.07
Aluminum, fracture, 4K	539.33	1.67
Al–3.5% Mg, y.p.	49.03	0.26
Silver, $\varepsilon = 0.005$	37.26	0.07
Silver, $\varepsilon = 0.002$	23.53	0.17
Silver, $\varepsilon = 0.20$	150.03	0.16
Hexagonal Close- Packed		
Cadmium, $\varepsilon = 0.001$, –196 °C	17.65	0.35
Zinc, $\varepsilon = 0.005$, 0 °C	32.36	0.22
Zinc, $\varepsilon = 0.175$, 0 °C	71.58	0.36
Magnesium, $\varepsilon = 0.002$	6.86	0.28
Magnesium, $\varepsilon = 0.002$, –196 °C	14.71	0.47
Titanium, y.p.	78.45	0.40
Zirconium, $\varepsilon = 0.002$	29.42	0.25
Beryllium, y.p.	21.57	0.41

[a] Adapted with permission from R. W. Armstrong, in *Advances in Materials Research*, Vol. 5, R. F. Bunshah, ed. (New York: Wiley-Interscience, 1971), p. 101.

[b] y.p. = yield point.

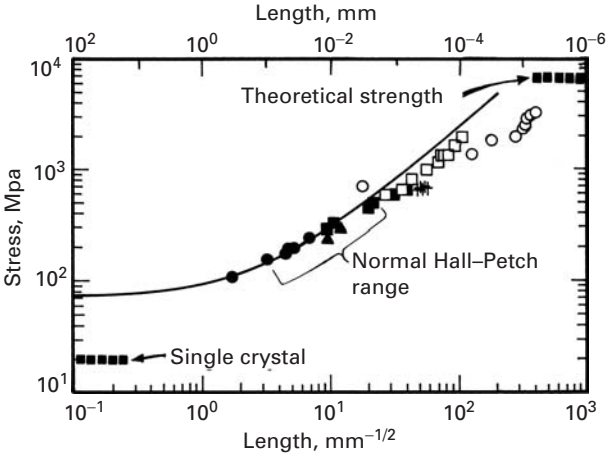

Fig. 5.24 Hall–Petch plot for iron and low-carbon steel extending from monocrystal to nanocrystal; notice the change in slope. (After T. R. Smith, R. W. Armstrong, P. M. Hazzledine, R. A. Masumura, and C. S. Pande, *Matls. Res. Soc. Symp. Proc.*, 362 (1995) 31.)

behavior should be considered not a universal law, but an approximation over a limited range of grain sizes. Since most engineering alloys have grain sizes in the range 10–100 μm, the Hall–Petch equation is indeed very useful.

The principal theories advanced to explain the Hall–Petch relationship are presented next. The first two theories have lost a lot of their credibility, because dislocation pileups are not thought to be as important as they used to be, especially in high-stacking-fault energy materials.

5.4.1 Hall–Petch Theory

The basic idea behind the separate propositions of Hall and Petch is that a dislocation pileup can "burst" through a grain boundary due to stress concentration at the head of the pileup. If τ_a is the resolved shear stress applied on the slip plane, then the stress acting at the head of a pileup containing n dislocations is $n\tau_a$ (Equation 4.26). The number of dislocations in a pileup depends on the length of the pileup, which, in turn, is proportional to the grain diameter D. According to Eshelby *et al.*[7] (see Equation 4.26(a)):

$$L = \frac{\alpha n G b}{\pi \tau_a}. \tag{5.9}$$

In this equation we have added a geometrical constant α which is equal to unity for screw dislocations and equal to $1\ (1 - \nu)$ for edge dislocations. If the source of the dislocation pileup is located at the centre of the grain, then $L = D/2$.

If τ_c is the critical stress required to overcome the grain-boundary obstacles, then the dislocations of the pileup will be able to traverse the grain boundary if

$$n\tau_a \geq \tau_c. \tag{5.10}$$

[7] J. D. Eshelby, F. C. Frank, and F. R. N. Nabarro, *Phil. Mag.* 42 (1951) 351.

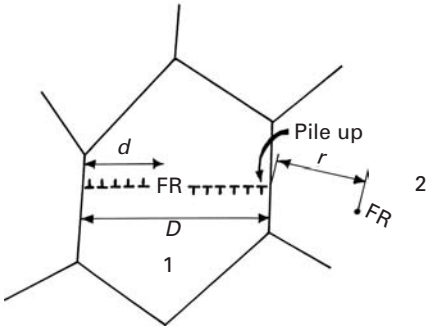

Fig. 5.25 Frank–Read source operating in center of grain 1 and producing two pileups at grain boundaries; the Frank–Read source in grain 2 is activated by stress concentration.

From Equation 5.9

$$\frac{\alpha D \tau_a}{2G b/\pi}\tau_a \geq \tau_c, \qquad \text{or} \qquad \frac{\alpha \pi D \tau_a^2}{2G b} \geq \tau_c.$$

In order to take into account the friction stress τ_0 needed to move the dislocations in the absence of any obstacle, we have to add the term τ_0. Thus,

$$\tau_a \geq \tau_0 + kD^{-1/2}. \tag{5.11}$$

Equation 5.11 is essentially identical to Equation 5.8, once the shear stresses are converted into normal stresses. Note that Eshelby's equation is valid only for a large number of dislocations; hence, the equation is not applicable to grain sizes below a few micrometers.

5.4.2 Cottrell's Theory

Cottrell[8] used a somewhat similar approach to that of Hall and Petch; however, he recognized that it is virtually impossible for dislocations to "burst" through boundaries. Instead, he assumed that the stress concentration produced by a pileup in one grain activated dislocation sources in the adjacent grain. Figure 5.25 shows how a Frank–Read source at a distance r from the boundary is activated by the pileup produced by a Frank–Read source in the adjacent grain. The slip band blocked in the boundary was treated by Cottrell as a shear crack. The maximum shear stress at a distance r ahead of a shear crack is given by

$$\tau = (\tau_a - \tau_0)\left(\frac{D}{4r}\right)^{1/2},$$

where τ_0 is the frictional stress required to move dislocations and $r < D/2$. The stress required to activate the Frank–Read source in the neighboring grain is given by

$$\tau_c = (\tau_a - \tau_0)\left(\frac{D}{4r}\right)^{1/2},$$

or

$$\tau_a = \tau_0 + 2\tau_c r^{1/2} D^{-1/2}.$$

This equation is of a Hall–Petch form.

[8] A. H. Cottrell, *Trans. TMS-AIME*, 212 (1958) 192.

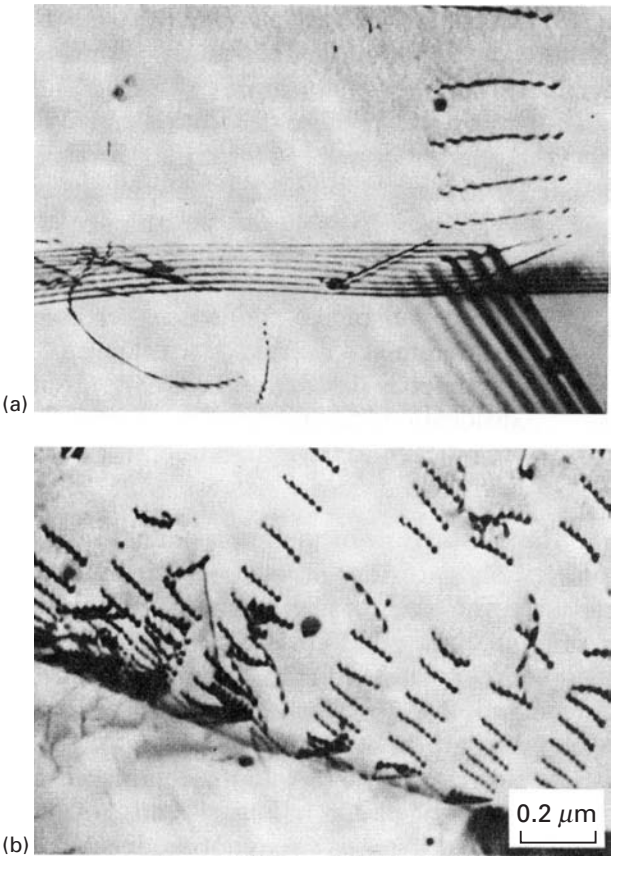

Fig. 5.26 Dislocation activity at grain boundaries in AISI 304 stainless steel ($\dot{\varepsilon} = 10^{-3}\ s^{-1}$). (a) Typical dislocation profiles after a strain of 0.15%. (b) Same after a strain of 1.5%. (Courtesy of L. E. Murr.)

5.4.3 Li's Theory

Li[9] used a different approach to obtain a relationship between the yield stress and grain size. Instead of using pileups, he considered the grain boundary to be a source of dislocations. The concept of grain-boundary dislocation sources is discussed in Section 4.4.8, and it is thought that the onset of yielding in polycrystals is associated with the activation of these sources. Li suggested that the grain-boundary ledges generated dislocations, "pumping" them into the grain. Figure 5.26 shows dislocation activity in stainless steel in the grain-boundary regions. These patterns can be interpreted as being due to dislocation pileups or dislocation emission from grain-boundary ledges. Such dislocations act as Taylor (Section 4.4.10) "forests" in regions close to the boundary. The yield stress is, according to Li, the stress required to move dislocations through these "forests." For many metals, the flow stress is related, under most conditions, to the dislocation density by the relationship (Section 6.3)

$$\tau = \tau_0 + \alpha G b \sqrt{\rho}, \tag{5.12}$$

[9] J. C. M. Li, *Trans. TMS-AIME*, 227 (1963) 239.

where τ_0 is the friction stress, α is a numerical constant, and ρ is the dislocation density. At this point, use was made of the experimental observation: ρ was taken to be inversely proportional to the grain diameter D. Li rationalized this as follows: The ledges "pump" dislocations into the grains. The number of dislocations generated per unit deformation is proportional to the number of ledges, or to the grain-boundary surface per unit volume, assuming the same ledge density per unit area for different grain sizes. That is,

$$\rho \propto S_v. \tag{5.13}$$

Equation 5.3 shows that the grain boundary surface per unit volume, S_v, is inversely proportional to D. Thus:

$$\rho \propto \frac{1}{D}. \tag{5.14}$$

Substituting Equation 5.14 into Equation 5.12, we obtain

$$\tau = \tau_0 + G b D^{-1/2}.$$

Again, this is a Hall–Petch equation.

5.4.4 Meyers–Ashworth Theory

There have been other proposals, including one by Meyers and Ashworth,[10] who analyzed elastic and plastic incompatibility stress between neighboring grains. Stress concentrations occur at grain boundaries during elastic loading because the strains have to be compatible. For metals having anisotropy ratios different from unity (see Chapter 2, Equation 2.17), the Young's moduli in different directions are different. For example, for nickel,

$$E[100] = 137\,\text{GPa},$$
$$E[110] = 233\,\text{GPa},$$
$$E[111] = 303\,\text{GPa}.$$

The incompatibility stresses were calculated by Meyers and Ashworth by finite element analysis and found to be

$$\tau_\text{I} = 1.37\sigma_\text{AP},$$

where σ_{AP} is the normal stress applied to the specimen. Hence, the interfacial shear stress due to the incompatibility is almost three times higher than the resolved shear stress homogeneously applied on the grain ($\tau_H = \sigma_{AP}/2$). This means that dislocation activity at the grain boundary starts before dislocation activity at the center of the grains.

When the stress reaches the critical level required for emission, localized plastic deformation will start (Figure 5.27(b)). These dislocations do not propagate throughout the grain, for two reasons:

[10] M. A. Meyers and E. Ashworth, *Phil. Mag.*, 46 (1982) 737.

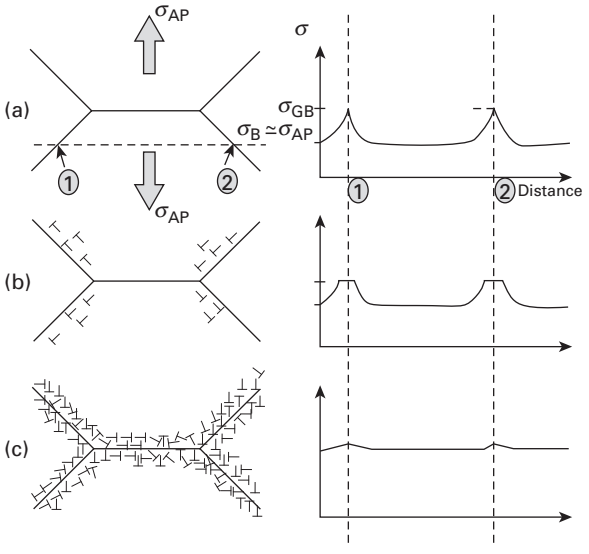

Fig. 5.27 Sequence of stages in (a) polycrystalline deformation, starting with (b) localized plastic flow in the grain-boundary regions (microyielding), forming (c) a work-hardened grain-boundary layer that effectively reinforces the microstructure.

1. The stress decreases rapidly with distance from the grain boundary.
2. The center of the grains is under homogeneous shear stress control, which is maximum at 45° to the tensile axis. On the other hand, the interfacial and homogeneous shear stresses have different orientations. Figure 5.27 shows how the dislocations emitted from the grain boundaries will undergo cross-slip. Extensive cross-slip and the generation of dislocation locks will result in a localized layer with high dislocation density.

The plastic flow of the grain-boundary region attenuates the stress concentration; geometrically necessary dislocations accommodate these stresses (Figures 5.27(b) and (c)). This marks the onset of microyielding. The dislocations do not propagate throughout the whole grain, because of cross-slip induced by the difference in orientation between the maximum shear stress (due to the applied load) and the stress concentration due to elastic incompatibility. The work-hardened grain-boundary layer has a flow stress σ_{GB}, while the bulk has a flow stress $\sigma_B(\sigma_{GB} > \sigma_B)$. The material behaves, at increasing applied loads, as a composite made out of a continuous network of grain-boundary film with flow stress σ_{GB} and of discontinuous "islands" of bulk material with flow stress σ_B. The increasing applied stress σ_{AP} does not produce plastic flow in the bulk in spite of the fact that $\sigma_{AP} > \sigma_B$, because the continuous grain-boundary network provides rigidity to the structure. The total strain in the continuous grain-boundary network does not exceed 0.005, since it is elastic; hence, plastic deformation in the bulk is inhibited. This situation can be termed "plastic incompatibility."

When the applied load is such that the stress in the grain-boundary region becomes equal to σ_{GB}, plastic deformation re-establishes itself in this region. The plastic deformation of the continuous matrix results in increases in stress in the bulk with plastic

flow (Figure 5.27(c)). This marks the onset of *macroyielding*. After a certain amount of plastic flow, dislocation densities in the bulk and grain-boundary regions become the same; then, since both regions have the same flow stress, plastic incompatibility disappears, and we have $\sigma_{AP} = \sigma_{GB} = \sigma_B$.

One arrives at a relationship

$$\sigma_y = \sigma_B + 8k(\sigma_{GB} - \sigma_B)D^{-1/2} - 16k^2(\sigma_{GB} - \sigma_B)D^{-1}. \tag{5.15}$$

The last term becomes important at small grain sizes and decreases the slope.

Example 5.6

If you could produce AISI 1020 steel with a grain size of 50 nm, what would be the expected yield stress, assuming a Hall–Petch response? (Use data from Figure 5.23.)

Solution: The Hall–Petch equation for this problem is $\sigma_y = \sigma_0 + kD^{-1/2}$. From Figure 5.23

$$\sigma_0 = 120\,\text{MPa},$$
$$k = 18\,\text{MPa/mm1/2} = 0.56\,\text{MN/m}^{3/2}.$$

Therefore,

$$\sigma = (120 \times 10^6) + (0.56 \times 10^6) \times (50 \times 10^{-9})^{-1/2}$$
$$= 2.65 \times 10^9\,\text{Pa}$$
$$= 2.65\,\text{GPa}.$$

5.5 Other Internal Obstacles

There are other internal obstacles to the motion of dislocations that may have an effect analogous to grain boundaries. Examples are cell walls and deformation twins. These barriers were studied by several investigators, and their effect on flow stress may be represented by the general equation

$$\sigma_f = \sigma_0 + K\,\Delta^{-m}, \tag{5.16a}$$

where the coefficient m has been found to vary between $\frac{1}{2}$ and 1. If we want to include the effects of both grain size and substructure refinement due to the internal barriers, we can use the following overall equation, which describes the response of the material reasonably well:

$$\sigma_f = \sigma_0 + K_1 D^{-1/2} + K_2 \Delta^{-m}. \tag{5.16b}$$

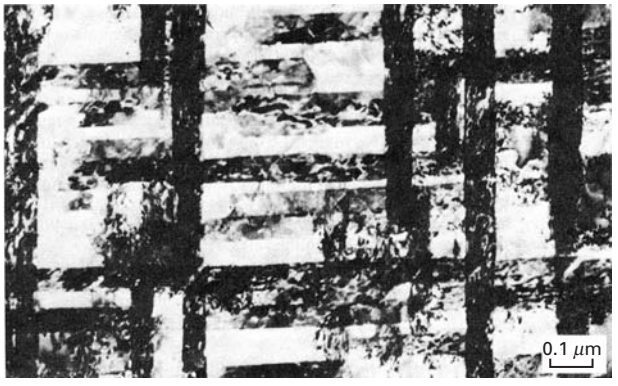

Fig. 5.28 Deformation twins in shock-loaded nickel (45 GPa peak pressure; 2 μs pulse duration). Plane of foil (100); twinning planes (111) making 90°. (Courtesy of L. E. Murr.)

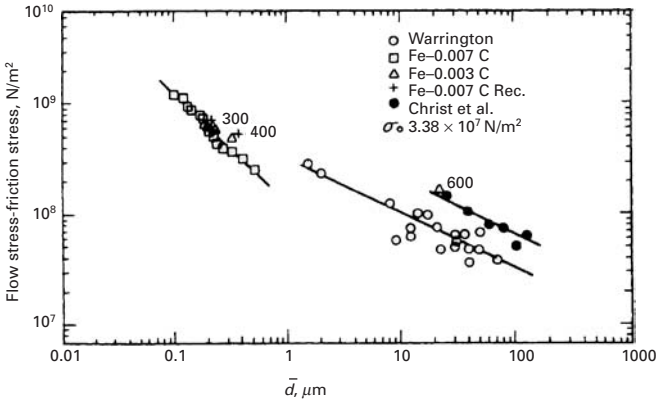

Fig. 5.29 Strength of wire-drawn and recovered Fe–0.003% C as a function of transverse lineal-intercept cell size. Recovery temperatures (in °C) as indicated. (Adapted with permission from H. J. Rack and M. Cohen, in *Frontiers in Materials Science: Distinguished Lectures*, L. E. Murr, ed. (New York: M. Dekker, 1976), p. 365.)

Figure 5.28 shows an example of substructural refinement in nickel. The twins were induced by shock loading at 45 GPa and 2 μs. It is easy to understand why these obstacles strengthen the metal. Dislocation movement occurring in subsequent deformation by, say, tensile testing is severely hampered by all such planar obstacles. Internal cells are also very effective barriers.

The effect of the dislocation cell size on the flow stress of highly cold-worked low-carbon steel wire is shown in Figure 5.29. The straining to high levels was accomplished by wire drawing, and the material was recovered and showed thin cell walls and virtually dislocation-free cell interiors. The slope in the log–log plot is −1, and we have, consequently,

$$\log(\sigma_f - \sigma_0) - \log(\sigma_1 - \sigma_0) = -1(\log \bar{d} - \log \bar{d}_1), \tag{5.17}$$

where this equation expresses the straight line passing through $(\sigma_f - \sigma_0, \bar{d})$ and $(\sigma_1 - \sigma_0, \bar{d}_1)$. Notice that the ordinate in Figure 5.26 is $\sigma - \sigma_0$. Manipulation of Equation 5.17 will yield

$$\log \frac{(\sigma_f - \sigma_0)}{(\sigma_f - \sigma_0)} = \log \left(\frac{\bar{d}}{\bar{d}_1} \right)^{-1}.$$

Hence,

$$\sigma_f - \sigma_0 = \frac{\sigma_1 - \sigma_0}{\bar{d}_1^{-1}} \bar{d}^{-1} = K \bar{d}^{-1}.$$
$$\sigma_f = \sigma_0 + K \bar{d}^{-1}.$$

On the other hand, when the annealings were done at 600 °C and above, recrystallization took place, and the group of points on the right side of the plot were found. The slope was decreased to $-\frac{1}{2}$, leading to a regular Hall–Petch relationship.

In low-carbon steels, the yield stress is strongly dependent on grain size; a steel with a grain size of 0.5 mm and σ_y of 104 MN/m^2 has its yield stress increased to approximately 402 MN/m^2 when the grain size is reduced to 0.005 mm. As the carbon content is increased and the steel tends more and more toward eutectoid, other effects, such as the ferrite–pearlite ratio, the spacing of cementite layers in the pearlite, and the size of the pearlite colonies, become important parameters. Gladman, McIvor, and Pickering[11] developed an expression for pearlite–ferrite mixtures, namely,

$$\sigma_y(\text{ksi}) = f_\alpha^{1/3}[2.3 + 3.81(\%\ \text{Mn}) + 1.13D^{-1/2}] + (1 - f_\alpha^{1/3})[11.6 + 0.25S_0^{-1/2}] + 4.1(\%\ \text{Si}) + 27.6(\sqrt{\%\text{N}}),$$

where f_α is the ferrite fraction, D is the ferrite grain size (in mm), S is the interlamellar spacing in pearlite (in mm), and % Mn, Si, and N are the weight percentages of manganese, silicon, and nitrogen, respectively.

Hyzak and Bernstein[12] proposed the following equation for fully pearlitic steels:

$$\sigma_y(\text{MPa}) = 2.18\ S^{-1/2} - 0.40\ P^{-1/2} - 2.88\ D^{-1/2} + 52.30.$$

Here, S is the pearlite interlamellar spacing, P is the pearlite colony size, and D is the austenite grain size. (The units of S, P, and D are not given by Hyzak and Bernstein, but should be cm.)

5.6 Nanocrystalline Materials

Since 1985, a great deal of research has been devoted to materials containing grain sizes in the nanometer range. These materials possess mechanical, magnetic, and electronic properties that are quite different from those of conventional crystalline materials (10 μm $\leq d \leq$ 300 μm). It is clear that high strength levels can be achieved through reductions in grain size. Another beneficial effect is an enhanced deformability of ceramics, due to the large grain-boundary interface. A strength level of 4,000 MPa was obtained in a drawn steel that had a grain size of 10 nm (0.01 μm).

[11] T. Gladman, I. D. McIvor, and R. E. Pickering, *J. Iron Steel Inst.*, 210 (1972) 916.
[12] J. M. Hyzak and I. M. Bernstein, *Met. Trans.*, 7A (1976) 1217.

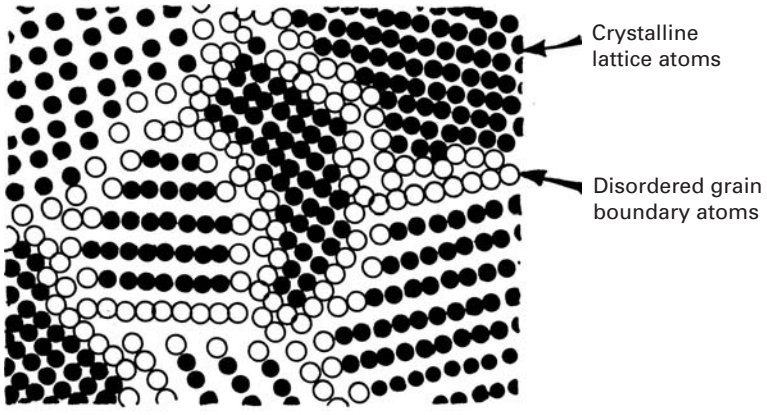

Fig. 5.30 Gleiter representation of atomic structure of a nanocrystalline material; white circles indicate grain-boundary regions. (Courtesy of H. Gleiter.)

Figure 5.30 shows the schematic atomic structure of a nanocrystalline material. The atoms in the centers of the crystals (black circles) have a crystalline periodic arrangement. The configuration was developed by Gleiter, based on a Morse potential fitted to gold. At the boundaries, the spacings are altered. Thus, nanocrystalline materials can be considered a new class of disordered materials created by having a sizeable fraction of the atoms at disordered sites. The boundary region is characterized by a lower atomic density, and this is indeed a characteristic of nanocrystalline materials (between 75 and 90% of the crystalline density). The densities of nanocrystalline materials vary from 83–96% for Pd and 72–97% for Cu. In conjunction with the lower density, the Young's modulus of nanocrystalline materials is also lowered. For Cu and Pd (with theoretical values of Young's modulus E of 120–130 GPa), the reported E value in the nanocrystalline state is 21–66 GPa.

Two principal methods are used to produce these nanocrystalline materials:

1. Evaporation of metal from melt and condensation on to a "cold finger;" this nanosized powder is subsequently densified by pressing.
2. Extreme mechanical deformation of powders in, for instance, a ball-milling machine. Hard spheres impinge upon powders numerous times until a saturation of defects occurs, causing recrystallization.

There are also other techniques: molecular beam epitaxy, rapid solidification from melt, reactive sputtering, sol-gel, electrochemical deposition, and spark erosion.

The mechanical properties of nanocrystalline materials are quite distinct from those of conventional polycrystalline materials. A simple extrapolation using the Hall–Petch equation would predict extraordinarily high values of the yield stress. For example, copper with a grain size of 25 nm should have a yield stress of 720 MPa (data extrapolated from Table 5.3). Indeed, experimental results, shown in Figure 5.31, show a very high yield stress ($\sim$185 MPa). However, a

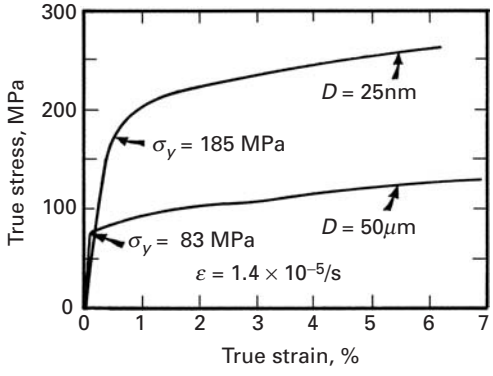

Fig. 5.31 Stress–strain curves for conventional ($D = 50$ μm) and nanocrystalline ($D = 25$ μm) copper. (Adapted from G. W. Nieman, J. R. Weertman, and R. W. Siegel, *Nanostructured Materials*, 1 (1992) 185.)

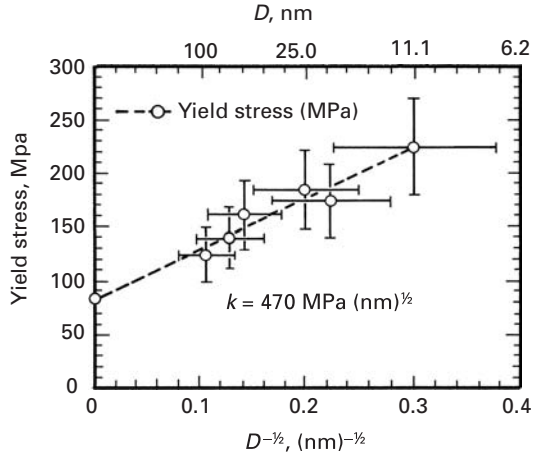

Fig. 5.32 Hall–Petch relationship for nanocrystalline copper. (After G. W. Nieman, J. R. Weertman, and R. W. Siegel, *Nanostructured Matls.*, 1 (1992) 185.)

simple extrapolation using the Hall–Petch equation does not predict quantitatively correct results. The Hall–Petch slope decreases as the grain size is decreased. Figure 5.32 shows the Hall–Petch relationship obtained in the nanocrystalline regimen (grain sizes between 10 and 100 nm). The slope k is equal to 470 MPa $\sqrt{\text{nm}}$. This can be converted into 0.014 MN/m$^{3/2}$. There has been considerable discussion as to the nature of the strength of nanocrystals. Some of the ideas[13,14,15] that have been bandied about are briefly presented in the following list.

1. *Dislocation pileups*. There is a minimum number of dislocations below which the equation for the stress concentration is no longer operative.
2. *Dislocation network models*. Models such as Li's or Meyers and Ashworth's use dislocation networks within the grain-boundary regions as the parameters determining the effects of grain size. Chang and Koch[13] and Scattergood and Koch[14] addressed these

[13] J. S. C. Chang and C. C. Koch, *Scripta Met. Mat.*, 24 (1990) 1599.
[14] R. O. Scattergood and C. C. Koch, *Scripta Met. Mat.*, 27 (1992) 1195.
[15] M. A. Meyers, A. Mishra, and D. J. Benson, *Prog. Mater. Sci.*, 51 (2006) 427.

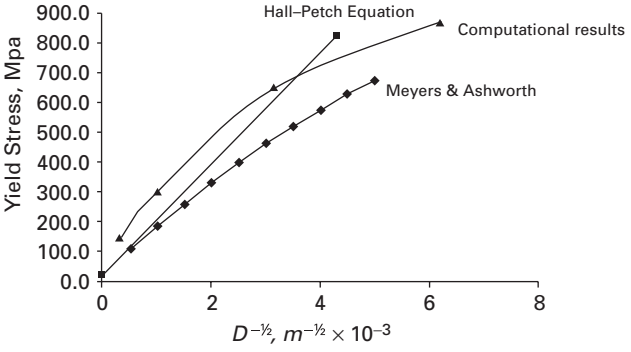

Fig. 5.33 Classical Hall–Petch slope compared with Meyers and Ashworth equation and computations assuming a grain-boundary region and grain interior with different work-hardening curves. As grain size is decreased, grain-boundary region gradually dominates the deformation process. (From H.-H. Fu, D. J. Benson, and M. A. Meyers, *Acta Mater.*, 49 (2001) 2567.)

phenomena and proposed that, below a critical grain size D_c, a dislocation-network mechanism controlled the flow stress. Meyers and Ashworth's formulation predicted a decrease in the Hall–Petch slope for smaller grain sizes, in line with experimental observations. Their theory is based on the formation of a hardened region along the grain boundaries (Section 5.4.4).

3. *Grain-boundary sliding.* In the nanocrystalline domain, sliding along grain boundaries becomes a significant component of plastic deformation for $D < 10$ nm.

The incorporation of the D^{-1} term into the Hall–Petch equation that was carried by Meyers and Ashworth, and is described in Section 5.4.4, leads to results that are shown in Figure 5.33. The The D^{-1} term in Equation 5.15 is negative and produces a gradual decrease in the slope of the Hall–Petch curve. This is evident from the plot in Figure 5.33, made by the application of Equation 5.15.

The same curvature was obtained by means of computational modeling carried out by Fu *et al.*[16] These calculations were made for grains as small as 26 nm. Figure 5.33 also shows the classical Hall–Petch slope for the micrometer-sized grains. It is a straight line. The slopes predicted from Equation 5.15 and from the computational prediction decrease with decreasing grain size and the yield stress approaches a saturation value as the grain size is reduced.

When the grain size is smaller than 10 nm, other processes start operating; grain-boundary sliding becomes important, as pointed out above, and some researchers have even reported a negative Hall–Petch slope.

5.7 Volumetric or Tridimensional Defects

Voids and inclusions are among the principal tridimensional defects in materials. Inclusions are often produced in metals by the accidental incorporation of slag or pieces of refractory bricks into the melt or

[16] H.-H. Fu, D. J. Benson, and M. A. Meyers, *Acta Mater.*, 49 (2001) 2567.

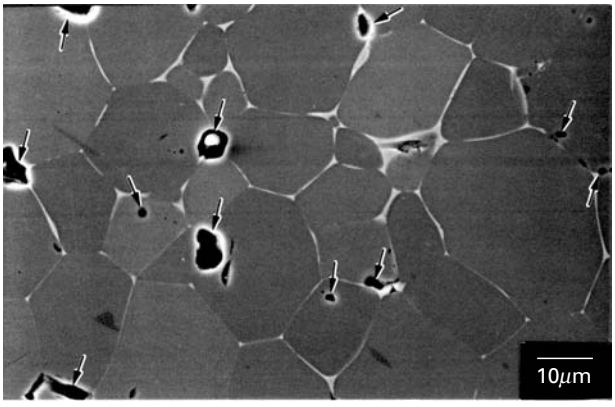

Fig. 5.34 Voids (dark spots marked by arrows) in titanium carbide. The intergranular phase (light) is nickel, which was added to increase the toughness of the TiC.

in powder metallurgy processes, from extraneous matter. Inclusions are also often the result of impurities, such as sulfur and phosphorous in steel. Vacuum arc remelting and other refining processes lead to alloys in which the inclusion content is minimized. Ceramics and brittle metals and intermetallics are especially sensitive to inclusions and voids. As will be seen in Chapter 8, these are easy sites for the initiation of fracture. Spherical and elongated flaws are the principal failure initiation sites in brittle materials. Such flaws are activated both in tension and compression, and are responsible for the great differences between compressive and tensile strength (a factor of 5–10).

Ceramics are often produced by sintering or hot pressing of powders. This often leaves a residual porosity, which is a major source of concern. Figure 5.34 shows the microstructure of titanium carbide produced by hot pressing of powders. Residual porosity can be seen, and the voids are indicated by arrows. These voids have diameters of 1–4 μm. It is difficult to completely eliminate porosity in ceramics. Small, intragranular pores that are only visible by TEM, such as the ones in Al_2O_3 in Figure 5.35(a), are very difficult to remove, because bulk diffusion is orders of magnitude slower than grain-boundary diffusion. If the voids were at the confluence of grain boundaries, it would be easier to eliminate them by high-temperature sintering. The voids seen in Figure 5.27(a) are faceted because this shape minimizes the overall surface energy; the surface energy is anisotropic, and the surfaces with the least number of broken bonds per unit area have the least energy. This is evident from the hexagonal voids shown in Figure 5.35(a), which all have parallel faces. The TEM of Figure 5.35(b) also shows dislocations, which are produced during hot pressing of titanium carbide. The difficulty of hot pressing or sintering pure, high-temperature ceramics without voids is often bypassed by using sintering aids, or materials with a lower melting point. These materials — usually glasses — become viscous at high temperatures and fill the existing voids. They also act as a high-temperature lubricant between the ceramic particles and help to densify the ceramic, by capillary action. An illustration of the use of sintering aids to help

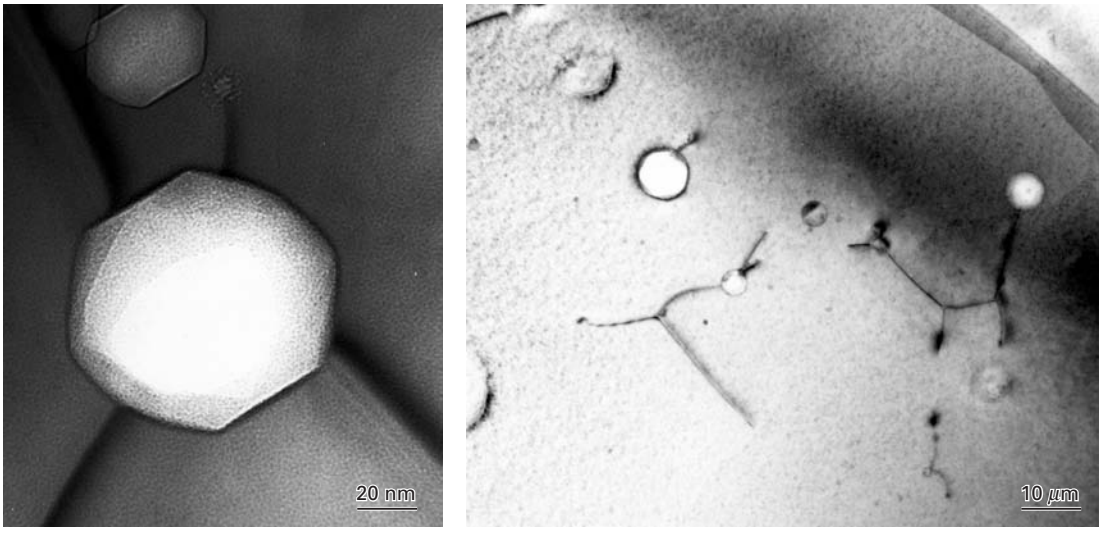

(a) (b)

Fig. 5.35 (a) Transmission electron micrograph illustrating faceted grain-interior voids within alumina and (b) voids in titanium carbide; dislocations are pinned by voids.

Fig. 5.36 Glassy phase at triple point in silicon nitride; notice the individual crystallographic planes in Si_3N_4. (Courtesy of K. S. Vecchio.)

the consolidation is given in Figure 5.36. Three silicon nitride grains are imaged by the TEM; the interplanar spacing, 0.65 nm, is shown. The three grains surround a glassy material, marked G. If no sintering aid were used, a central void would be formed. Nevertheless, the glassy phase is a volumetric defect and results in a weaker material than a fully dense, pure Si_3N_4.

Example 5.7

(a) Calculate the volume fraction of voids in the micrograph in Figure 5.34.
(b) If Young's modulus for fully dense TiC is 440 GPa, what is Young's modulus for the porous TiC?

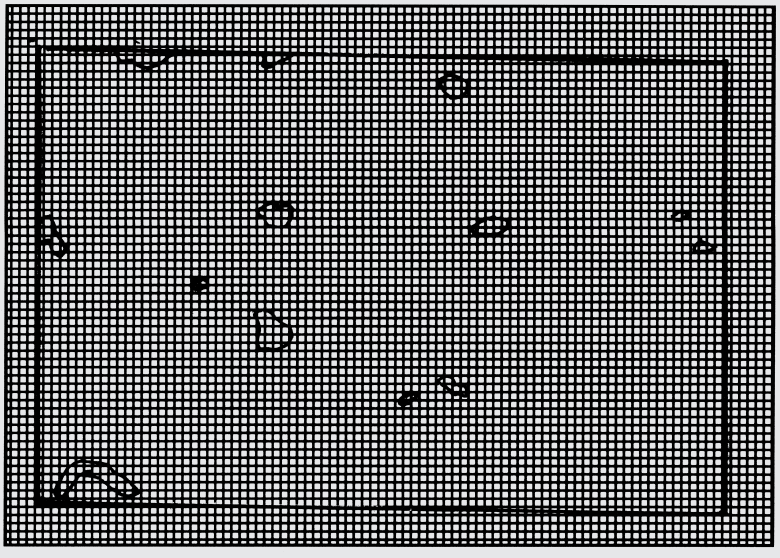

Fig. E5.7

Solution:

(a) We overlay a grid on the micrograph and count the intersections of lines falling within the voids. (See Figure E5.7.)

$$\text{Total numbers of intersections in grid} = 72 \times 47 = 3{,}384;$$

$$\text{Total numbers of intersections inside voids} \approx 66.$$

Therefore, the porosity is approximately 66/3,384 = 2%.
(b) From Chapter 2, we obtain the equation for Young's modulus (Equation 2.25):

$$\begin{aligned} E &= E_0(1 - 1.9p) \\ &= 440 \times (1 - 1.9 \times 0.02) \\ &= 423 \text{ GPa}. \end{aligned}$$

5.8 Imperfections in Polymers

Let us consider again the basic "cooked spaghetti" structure of a polymer. In an amorphous polymer, there is no apparent order among

the molecules, and the polymeric chains are arranged randomly. As we pointed out in Chapter 1, macromolecules can be made to crystallize. However, unlike metals or ceramics, long-chain polymers or macromolecules (synthetic or natural) do *not* form exact, periodic structures having long-range order in three dimensions. This is because such a highly ordered structure in a polymer, in general, will not be in equilibrium. It is, however, possible to obtain a variety of metastable chain conformations, depending on the route taken to reach a particular state. In any of these metastable states, order may be locally present; that is, we can have crystalline regions interspersed with amorphous regions. Polymers can thus be amorphous or partially crystalline, a 100% crystalline polymer being difficult to obtain in practice. In a partially crystalline or semicrystalline polymer, depending on its type, molecular weight, and crystallization temperature, the amount of crystallinity can vary from 30 to 90%. The inability to attain a fully crystalline structure is due mainly to the long chain structure of polymers: Some twisted and entangled segments of chains that get trapped between crystalline regions never undergo the conformational reorganization necessary to achieve a fully crystalline state. Molecular architecture also has an important bearing on the polymer crystallization behavior: Linear molecules with small or no side groups crystallize easily; branched chain molecules with bulky side groups do not. For example, linear, high-density polyethylene can be crystallized to more than 90%, whereas branched polyethylene can be crystallized only to about 65%.

Amorphous polymers can be considered to be fairly homogeneous on a supramolecular scale. Semicrystalline polymers, consisting of tiny crystalline regions randomly distributed in an amorphous material, are heterogeneous, multiphasic, or even *composite* in nature. Lamellar crystals can form when a crystallizable polymer such as a linear polymer is cooled very slowly from its melting point. Small, platelike lamellar single crystals can also be obtained by the precipitation of a polymer from a dilute solution. The long molecular chains in the lamellae are folded in a regular manner. In a lamellar-polymer single crystal, the thickness of a lamella is typically about 10 nm, while the length of the chain is about 100 to 1,000 nm. The extremely long chain is conformed into a narrow lamella by the process of chain folding during crystallization. Figure 1.26c shows this phenomenon of chain folding. Many such lamellar crystallites group together and form spherulites. (See Chapter 1.)

Crystalline defects such as those described for metals and ceramics are not at all ubiquitous in polymers. One may define defects in polymers in simple chemical and physical terms. Chemical defects include defects such as a linear polymer branching off into two branches that grow at different rates to give branches of different lengths. One can also have syndiotactic defects, which are stereochemical in nature. For example, an isotactic polymer chain can have syndiotactic defects embedded in it. Physical aspects of defects involve conformational defects in chain coiling. It is easy to see that kinetic and energetic

factors will be very important in these type of defects, because such defects involve chain movement. Variables such as temperature, pressure, concentration, molecular weight, chain polarity, etc., are important, and statistical mechanics needs to be used. Thus, point defects in polymers are chain-conformational kinks, jogs, and inclusions. Point defects also include an interstitial or substitutional molecule. For example, if a macromolecular chain consisting of species *A* has a monomer *B* trapped inside the polymer crystal, that would be an interstitial point defect. If there is a break in the length of the molecular chain we will have a chain end and a vacancy or a row of vacancies.

As we have seen, in metals dislocations are very important because they are mobile, while in ceramics they are immobile under most conditions. Although dislocations can exist in polymeric crystals also, they do not play such a major role in the deformation of polymers. Direct observations of dislocations have been made in some semicrystalline polymers by transmission electron microscopy, which has been instrumental in elucidating the structural imperfections in metals and ceramics. One of the great limitations to the use of electron microscopy in the study of polymers is the radiation damage produced in the polymers by the electron beam. Images produced by electron diffraction contrast, as well as electron diffraction patterns, depend on the crystallinity of the specimen. A large dose of electrons will tend to destroy the long-range crystalline order, more so in polymers than in metals or ceramics, because nonpolymeric crystalline materials such as metals and ceramics are more resistant to electron irradiation. Thus, only a limited number of scattered electrons can be used to obtain crystallographic information from the sample under study before the diffraction pattern changes from crystalline reflections to broad, amorphous haloes. Radiation damage can establish cross-links and cause strain in the lattice at first. Continued exposure to an electron beam can make the diffraction contrast weaker and eventually disappear. It is therefore necessary to take special precautions before examining the structure of polymers in an electron microscope. Perhaps the most widely studied polymer in this regard is polyethylene, although it is difficult to take high-resolution images of polyethylene at room temperature by TEM because of the sensitivity of the polymer to radiation. By comparison, thermoplastics such as PPS, PEEK, and PEK are fairly resistant to electron irradiation. Experimentally, giant screw dislocations showing growth spirals have been observed in these thermoplastics. Terminating moiré fringes have been used to show the existence of dislocations in a polyethylene crystal. A lattice-imaging technique has been used on poly (para phenylene terephthalamide) PPTA and poly (paraphenylene benzobis thiazole) PBT fibers. In these fibrous materials, one has, relative to polyethylene, rather high radiation stability for electron microscopic observations because of the electronic conjugation of the backbone chain.

In crystalline metals and ceramics, two-dimensional defects such as grain boundaries are thin regions where two grains meet. In polymeric crystals, grain boundaries can be very complex, again because

of the chain connectivity. Besides, the electron beam sensitivity of polymers makes TEM observations and their interpretation quite difficult. Planar defects such as stacking faults and twins have been observed in samples of poly (diacetylene) crystals.

Suggested Reading

Interfacial Defects

H. Gleiter. "On the Structure of Grain Boundaries in Metals." *Mater. Sci. Eng.*, 52 (1982) 91.

H. Gleiter and B. Chalmers. "High-Angle Grain Boundaries," *Progress in Materials Science*, vol. 16, B. Chalmers, J. W. Christian, and T. B. Massalski, eds. Elmsford, NY: Pergamon Press, 1972.

L. E. Murr. *Interfacial Phenomena in Metals and Alloys*. Reading, MA: Addison-Wesley, 1975.

A. P. Sutton and R. W. Baluffi. *Interfaces in Crystalline Materials*. New York, NY: Oxford University Press, 1994.

Twinning

R. E. Reed-Hill, J. P. Hirth, and H. C. Rogers, eds., *Deformation Twinning*. TMS-AIME Conf. Proc. New York, NY: Gordon and Breach, 1965.

J. W. Christian and S. Mahajan. *Deformation Twinning*. New York, NY: Oxford University Press, 1995.

Grain-Size Effects

R. W. Armstrong. "The Influence of Polycrystal Grain Size on Mechanical Properties" in *Advances in Materials Research*, vol. 4, H. Herman, ed. New York, NY: Wiley Interscience, 1971, p. 101.

R. W. Armstrong, in *Yield, Flow, and Fracture of Polycrystals*, T. N. Baker, ed. London: Appl. Sci. Publ., 1983, p. 1.

H. Gleiter, "Nanocrystalline Materials," *Progress in Materials Science*, 33 (1989) 223.

Exercises

5.1 Calculate the dislocation spacing in a symmetrical tilt boundary ($\theta = 0.5^\circ$) in a copper crystal.

5.2 Starting from the equation $E = E_0\theta(A - \ln \theta)$ for a low-angle boundary, show how one can obtain graphically the values of E_0 and A.

5.3 Taking $A = 0.3$, compute the value of $\theta_{\max}$.

5.4 Show that, for a low-angle boundary, we have

$$\frac{E}{E_{\max}} = \frac{\theta}{\theta_{\max}}\left(1 - \ln \frac{\theta}{\theta_{\max}}\right),$$

where $E_{\max}$ and $\theta_{\max}$ correspond to the maximum in the E-versus-θ curve.

5.5 Consider two parallel tilt boundaries with misorientations θ_1 and θ_2. Show that, thermodynamically, we would expect the two boundaries to join and form one boundary with misorientation $\theta_1 + \theta_2$.

5.6 Can you suggest a quick technique to check whether lines observed in an optical microscope on the surface of a polished sample after deformation are slip lines or twin markings?

5.7 A twin boundary separates two crystals of different orientations; however, we do not necessarily need dislocations to form a twin. Why?

5.8 Let m be the total length of dislocations per unit area of a grain boundary. Assume that at yield, all the dislocations in the grain interiors (ρ) are the ones emitted by the boundaries. Assume also that the grains are spherical (with diameter D). Derive the Hall–Petch relation ($\sigma = \sigma_0 + kD^{-1/2}$) for this case, and give the expression for k.

5.9 Consider a piano wire that has a 100% pearlitic structure. When this wire undergoes a reduction in diameter from D_0 to $D\varepsilon$, the pearlite interlamellar spacing normal to the wire axis is reduced from d_0 to $d\varepsilon$, that is,

$$\frac{d_0}{d_\varepsilon} = \frac{D_0}{D_\varepsilon},$$

where the subscript o refers to the original dimensions, while the subscript ε refers to the dimensions after a true plastic strain of ε. If the wire obeys a Hall–Petch type of relationship between the flow stress and the pearlite interlamellar spacing, show that the flow stress of the piano wire can be expressed as

$$\sigma = \sigma_i + \frac{k'}{\sqrt{d_0}} \exp\left(\frac{\varepsilon}{4}\right).$$

5.10

(a) Determine the mean lineal intercept, the surface area per unit volume, and the estimated grain diameter for the specimen shown in Figure Ex5.10.

(b) Estimate the yield stress of the specimen (AISI 304 stainless steel).

(c) Estimate the parameters of part (a), excluding the annealing twins. By what percentage is the yield stress going to differ?

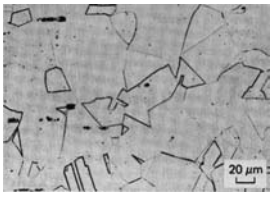

Fig. Ex5.10

5.11 Professor M. I. Dum conducted a study on the effect of grain size on the yield stress of a number of metals using thin foil specimens (thickness 0.1 mm and width 6.25 mm). He investigated grain sizes of 5, 25, 45, and 100 μm. Which specimens can be considered truly polycrystalline?

5.12 Thompson[17] obtained the following results for the yield stress of nickel:

Grain Size (μm)	Yield Stress (MN/m^2)
0.96	251
2	185
10	86
20	95
95	33
130	25

[17] A. W. Thompson, *Acta Met.*, 25 (1977) 83.

(**a**) Find the parameters in the Hall–Petch equation. Plot the yield stress versus D^{-1}, $D^{-1/2}$, and $D^{-1/3}$. Which plot shows the best linearity?
(**b**) Show how you can determine the correct exponent by another plot (not by trial and error).

5.13 If the grain size of a metal is doubled by an appropriate annealing, by what percentage is the surface area per unit volume of the metal changed?

5.14 Nilles and Owen[18] found a strong grain-size dependence of the stress required for twinning when deforming an Fe–25 at.% Ni alloy at 4 K. From what you learned in the text, is this behavior expected? Compare the ratio of the Hall–Petch slopes of the twinning and yield stresses for Fe–25% Ni with the ratio found for chromium and Fe–Si.

5.15 Most polycrystalline materials, when etched, form grooves at grain boundaries. When annealed, ceramics form thermal grooves at grain boundaries. A schematic of such a groove is shown in Figure Ex5.15. If the surface energy per unit area of the material is γ_s, derive an expression for the energy per unit area of the grain boundary between grains 1 and 2.

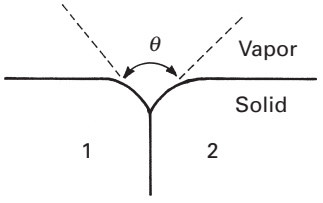

Fig. Ex5.15

5.16 Estimate the average grain diameter and the grain-boundary area per unit volume for a material that has isotropic grains (the same dimension in all directions) and ASTM grain size 6.

5.17 How many grains in an area of 5 × 5 cm would be counted, in a photomicrograph taken at a magnification of 500×, for a metal with ASTM grain size 3?

5.18 A graduate student (undergraduates are much brighter!) measured the grain size of a metallic specimen and found that it was equal to ASTM #2. However, he had the wrong magnification in his picture (400× instead of 100×). (a) What is the correct ASTM grain size? (b) What is the approximate grain diameter?

5.19 Nanophase materials show many different characteristics vis-à-vis conventional materials. Discuss the sintering behavior of a nanophase powder in relation to that of a conventional powder.

5.20 Calculate the volume fraction of voids in the TiC specimen shown in Figure 5.35(b).

5.21 Examine Figure Ex5.21.
(**a**) Using the lineal intercept method, determine the mean lineal intercept and the grain size if the material is TiC.
(**b**) Determine the grain size using the ASTM method.

5.22
(**a**) Using the mean lineal intercept, calculate the grain diameter for tantalum, given the micrograph in Figure 5.29(a).
(**b**) Calculate the ASTM grain size.
(**c**) Estimate the yield stress for this specimen of tantalum, using values from Table 5.3.

[18] J. L. Nilles and W. S. Owen, *Met. Trans*., 3 (1972) 1877.

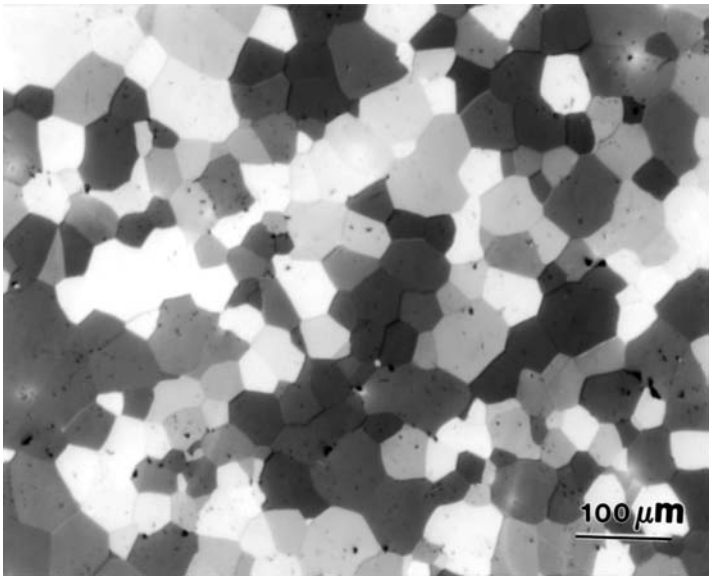

Fig. Ex5.21

5.23 A polycrystalline sample has 16 grains per square inch in a photomicrograph taken at magnification 100×. What is the ASTM grain size number?

5.24 A 20-cm line gave seven intersections in a 100× micrograph. Using the lineal intercept method, determine the mean lineal intercept and the grain size.

5.25 How many grains in an area of 5 × 5 cm would be counted in a photomicrograph taken at a magnification of 500× for a metal with an ASTM grain size 3.

5.26 The yield stress of AISI 1020 steel with a grain size of 200 μm is 200 MPa. Estimate the yield stress for a grain size of 10 μm if the Hall–Petch constant $k = 0.8$ MN/m$^{3/2}$.

5.27 A small-angle tilt boundary has a misorientation of 0.1°. What is the spacing between the dislocations in this boundary if the Burgers vector of the dislocation is 0.33 nm?

5.28 Calculate the dislocation spacing of a low-angle tilt boundary in aluminum for $\theta = 0.5°$. Take $G = 26.1$ GPa, $v = 0.345$, and $r_{Al} = 0.143$ nm.

5.29

(a) Determine the grain size for the microstructure of zirconium shown in Figure Ex5.29, using the lineal intercept method. Use the scale given at the bottom.

(b) Use the Hall–Petch equation to determine the yield stress of this material, given $\sigma_0 = 29$ MPa, $k = 0.25$ MPa m$^{1/2}$.

5.30 From Figure 5.2 (a, b) find the grain diameter of samples using the lineal intercept ASTM method, $N = 2^{n-1}$.

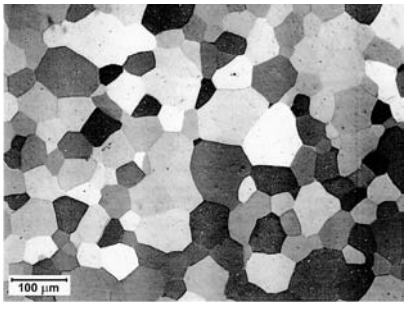

Fig. Ex5.29 Microstructure of zirconium. (Courtesy of S. Barrabes and M. E. Kassner.)

5.31 Calculate the dislocation spacing and energy of a low-angle tilt boundary in Ni if $\theta = 0.5^\circ$, $G = 76$ GPa, $r = 0.125$ nm, $\nu = 0.31$.

5.32 If a sample of copper had a grain size of 75 mm, what would be the expected yield stress, assuming a Hall–Petch response? (Use the data from Figure 5.23.)

5.33 Describe the difference between deformation twins and annealing twins. Describe the differences in twinning in HCP, BCC, and FCC crystals.

Chapter 6

Geometry of Deformation and Work-Hardening

6.1 Introduction

The relaxation times for the molecular processes in gases and in a majority of liquids are so short, that molecules/atoms are almost always in a well-defined state of complete equilibrium. Consequently, the structure of a gas or liquid does not depend on its past history. In contrast, the relaxation times for some of the significant atomic processes in crystals are so long, that a state of equilibrium is rarely, if ever, achieved. It is for this reason that metals in general (and ceramics and polymers, under special conditions) show the usually desirable characteristic of work-hardening with straining, or strain-hardening. In other words, plastic deformation distorts the atoms from their equilibrium positions, and this manifests itself subsequently in hardening.

In fact, hardening by plastic deformation (rolling, drawing, etc.) is one of the most important methods of strengthening metals, in general. Figure 6.1 shows a few deformation-processing techniques in which metals are work-hardened. These industrial processes are used in the fabrication of parts and enable the shape of metals to be changed. The figure is self-explanatory. Rolling is used to produce flat products such as plates, sheets, and also more complicated shapes (with special rolling cylinders). In forging, the top hammer comes down, and the part is pushed into a die (closed-die forging) or is simply compressed. Extrusion uses a principle similar to that in the use of a tube of toothpaste. The material is squeezed through a die, and its diameter is reduced. In stamping, first the ends of a blank are held, and then the upper die comes down, punching the blank into the lower die.

If deformation is carried out at low and moderate temperatures, the metal workhardens. However, if the temperature is sufficiently high, the dislocations generated in work-hardening are annealed out, and the final metal is in the annealed condition. *Hot working* designates all work done on a metal or alloy above its recrystallization temperature, while *cold working* indicates work done below the

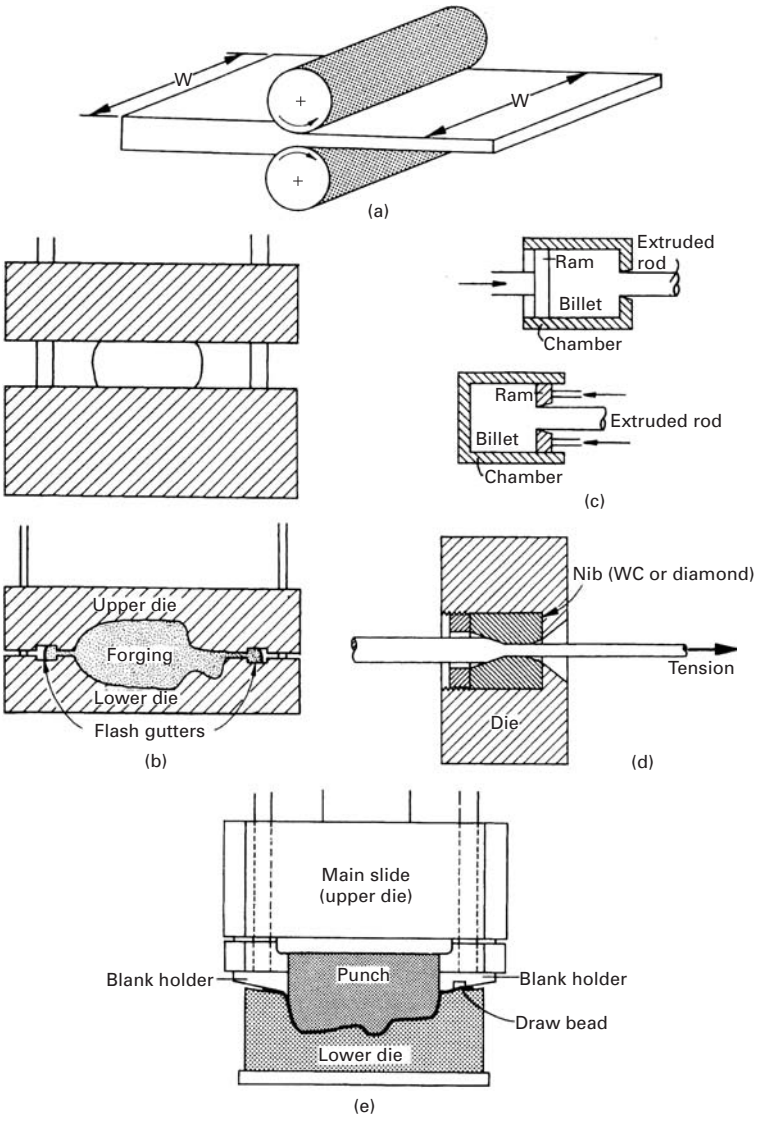

Fig. 6.1 Common metalworking methods. (a) Rolling. (b) Forging (open and closed die). (c) Extrusion (direct and indirect). (d) Wire drawing. (e) Stamping.

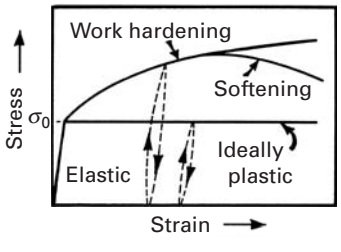

Fig. 6.2 Stress–strain curves (schematic) for an elastic, ideally plastic; a work-hardening; and a work-softening material.

recrystallization temperature of the metal or alloy. Certain metals, in particular (e.g., copper), do not have many precipitation hardening systems, but are ductile and can be appreciably hardened by cold working. If the relaxation times were short, the structure would return almost immediately to its state of equilibrium, and a constant stress for plastic deformation would result, independent of the extent of deformation. This is shown in Figure 6.2 as the elastic, ideally plastic solid. However, when a real crystalline solid is deformed plastically, it turns more resistant to deformation, and a greater stress is required for additional deformation. The phenomenon is called *work-hardening*. If the stress is interrupted, and the material is unloaded after a certain plastic strain, the unloading slope is equal to the Young's modulus. Upon loading, the stress returns to its original

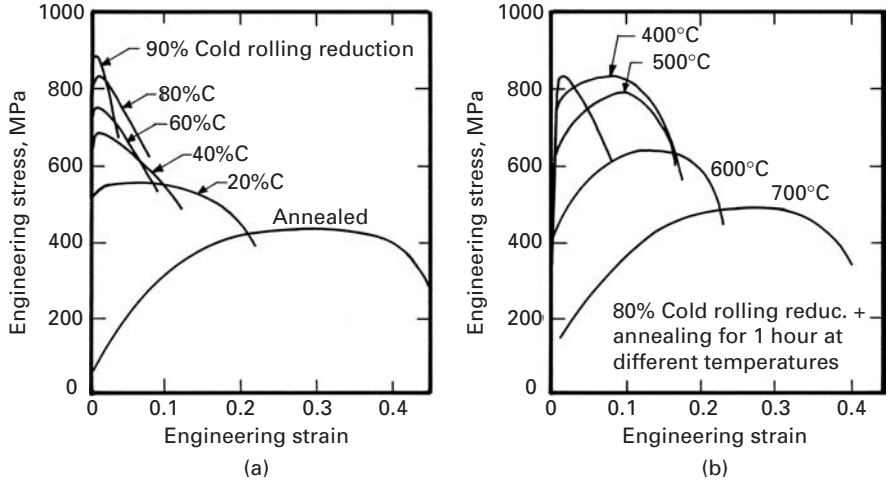

Fig. 6.3 Engineering-stress–engineering-strain curves for nickel. (a) Nickel subjected to 0, 20, 40, 60, 80, and 90% cold-rolling reduction. (b) Nickel cold rolled to 80%, followed by annealing at different temperatures. (From D. Jaramillo, V. S. Kuriyama, and M. A. Meyers, *Acta Met.* 34 (1986) 313.)

value. Thus, for a work-hardening material, the flow stress is increased above σ_0, whereas for an ideally plastic material, the flow stress is constant at σ_0. Under certain conditions, the material can also soften. This is also shown in Figure 6.2 and is discussed in greater detail in Section 6.4.

In Chapter 4, we discussed the various kinds of defects in materials. Of these defects, the primary carriers of plastic deformation in metals and ceramics are dislocations and twins. From the simple motion of dislocations along specific planes, we derived the Orowan Equation 4.29, which relates the global plastic strain to the individual dislocation motion and density. Basically, the hardening in a crystalline structure occurs because these materials deform plastically by the movement of dislocations, which interact directly among themselves and with other imperfections, or indirectly with the internal stress field (short range or long range) of various imperfections and obstacles. All these interactions lead to a reduction in the mean mobility of dislocations, which then require a greater stress for accomplishing further movement (i.e., with continuing plastic deformation, we need to apply an ever greater stress for further plastic deformation); hence the phenomenon of work-hardening.

Figure 6.3 illustrates how a metal (in this case, nickel) work-hardens by cold rolling. As the nickel plate is reduced in thickness (and increased in length), its stress–strain response changes. In the figure, we plot engineering stress versus engineering strain, and all the curves show a softening after hardening. This softening is due not to an inherent structural "softening," but to a localized reduction in cross section, called *necking*. (See Chapter 3.) The yield stress increases from less than 100 MPa (in the annealed condition) to approximately 850 MPa (after 90% reduction in thickness by cold rolling). Concomitantly, the ductility decreases. The sample that received 80% reduction was subjected to one-hour annealings at various temperatures; the resulting mechanical response is shown in Figure 6.3(b). After a 700 °C annealing, the curve is almost coincident with the original

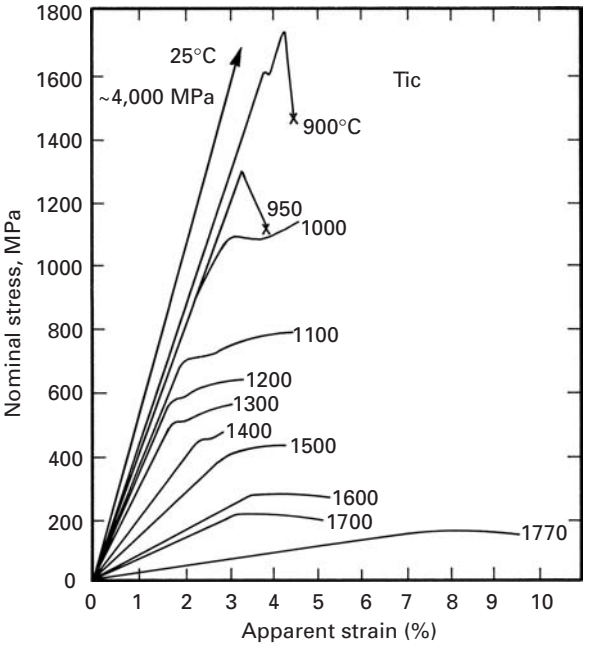

Fig. 6.4 Stress–strain curves for annealed polycrystalline TiC deformed in compression at the temperatures indicated ($\dot{\varepsilon} = 1.7 \times 10^{-4}\ s^{-1}$). (Adapted from G. Das, K. S. Mazdiyasni, and H. A. Lipsitt, *J. Am. Cer. Soc.*, 65 (1982) 104.)

annealed curve, showing that the effects of cold rolling have been eliminated. This occurs because the dislocations produced by plastic deformation have been eliminated by the annealing. The nickel specimens were polycrystalline, with a grain size of 40 μm.

In Chapter 4, we dealt exclusively with monocrystals; we will see, in this chapter, how the plastic deformation in one single crystallographic direction is related to the overall deformation of a crystal and how different crystals in a polycrystal deform in a "cooperative" manner.

In ceramics, plastic deformation is not so common. At room temperatures many ceramics are brittle, and it was seen in Chapter 4 that the Peierls–Nabarro stress opposing dislocations is much higher and that the mobility of dislocations is much more restricted than for metals. This is illustrated in Figure 6.4 which shows results of compression tests on TiC specimens carried out at different temperatures. Note that the elastic portion of the curves shows a slope that is considerably lower than the prediction from the Young's modulus, because no extensometer was used to measure strain. Thus, the abscissa records both the strain in the specimen and the deflection in the machine; for this reason, the term "apparent strain" is used. The ambient-temperature compressive strength of TiC is approximately 4,000 MPa. As the temperature is increased beyond 950 °C, plastic deformation gradually sets in. This is called the *ductile–brittle transition*. As the temperature is increased, the flow stress decreases. In this temperature regimen, the material exhibits plasticity. In monocrystalline Al_2O_3 deformed at high temperatures, significant plastic deformation is also observed. Figure 6.5 shows the

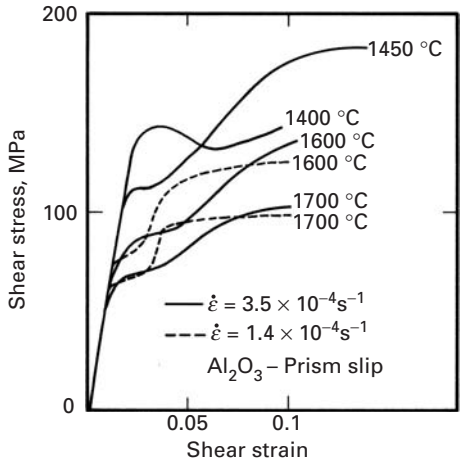

Fig. 6.5 Shear stress τ vs. shear strain γ for prism plane slip in Al_2O_3 at various temperatures; $\dot{\varepsilon} = 3.5 \times 10^{-4}\ s^{-1}$ for the solid curves, $\dot{\varepsilon} = 1.4 \times 10^{-4}\ s^{-1}$ for the dashed curves. (Courtesy of T. E. Mitchell.)

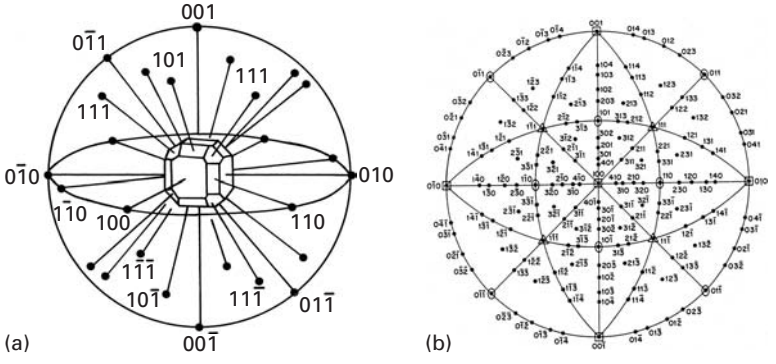

Fig. 6.6 (a) Representation of crystallographic directions and poles (normals to planes) for cubic structure. (b) Standard [100] stereographic projection. (Reprinted with permission from C. S. Barrett and T. B. Massalski, *The Structure of Metals*, 3d ed. (New York: McGraw-Hill, 1966), p. 39.)

shear-stress–shear-strain response for Al_2O_3 oriented for prismatic slip. (See Section 4.4.7.)

6.2 Geometry of Deformation

6.2.1 Stereographic Projections

The mechanical properties of crystals are anisotropic, and slip occurs only on certain planes, along certain directions. For this reason, it is important to define the *orientation* of a crystal. The most common technique for doing so is the stereographic projection, which will be presented here in an abbreviated way; greater details are given in Barrett and Massalski. (See suggested reading.) The stereographic projection is a geometric representation of the directions and planes of a crystal. From stereographic projections, one can determine the angles between planes, planes and directions, and directions. The stereographic projection is the projection of a sphere on a plane. We imagine a unit cell of a certain crystalline structure at the center of the sphere. (See Figure 6.6(a).) The directions and plane poles (normals to the planes passing through the origins) intercept a sphere at points; these points are projected onto a plane. Figure 6.6(b) shows a standard

cubic projection. This projection is known as a [100] standard projection because the <001> direction corresponds to the center. There are other standard projections: [110], [111], [112], and so on. Theoretically, the angles between directions and/or plane poles are measured on the sphere; in practice, however, these angles are measured on the standard projection, making use of a special chart called the Wulff net. This chart is the projection of a plane of a sphere in which all the meridians and parallels are marked at regular degree intervals. The sphere has the same diameter as the standard projection. By inserting a tack at the center and rotating the standard projection around it, we can easily find all desired angles.

An analogy can be made with maps. Imagine that we look at the earth from the "top;" that is, we view the northern hemisphere with the north pole at the center. If we now draw a map on a circle, we have a situation analogous to a stereographic projection. The meridians of the map correspond to great circles on the stereographic projection – that is, circles whose center is coincident with the center of the sphere. The four great circles that are perpendicular to the plane of the paper are projected as straight lines.

In a stereographic projection, the crystalline symmetry can be clearly seen. For instance, the <100> directions form a cross in Figure 6.6, with the crystalline symmetry indicated in Figure 6.6(b); two-, three-, four-, and six-field symmetry axes are shown. (The symmetries have been introduced in Section 2.8, and the reader is referred to Table 2.1.) For the <111>, <110>, and <100> directions, the symmetry is four-, two-, and threefold, respectively, in the cubic system. Two-, three-, and fourfold symmetries are indicated by lens, triangle, and square, respectively. As a consequence, the standard projection can be divided, by means of great circles, into 24 spherical triangles that are crystallographically equivalent. The vertices of these triangles are <100>, <110>, and <111>, as can be seen in Figure 6.7. Comparing this figure with Figure 6.6(b), we can see that the directions on the sides and within the spherical triangles are also equivalent. Consequently, one single triangle is sufficient to specify any crystallographic orientation in the cubic system; the [100], [110], [111] triangle is used most commonly. The reader is warned, however, that this simplification is not applicable to the other crystal systems.

6.2.2 Stress Required for Slip

The flow stresses of crystals are highly anisotropic. For instance, the yield stress of zinc under uniaxial tension can vary by as much as a factor of 6, depending on the orientation. Consequently, it is very important to specify the orientation of the load with respect to that of the crystal. In shear or torsion tests, the shear plane and directions are precisely known. Because dislocations can glide only under the effect of shear stresses, these shear stresses have to be determined. In uniaxial tensile and compressive tests (the most common tests), one has to determine mathematically the shear component of the applied stress acting on the plane in which slip is taking place.